UNIVERSITY OF CALIFORNIA
SANTA CRUZ

THE GEOLOGIC CONTEXT OF LUNAR MAGNETIC ANOMALIES

A dissertation submitted in partial satisfaction of the
requirements for the degree of

DOCTOR OF PHILOSOPHY

in

EARTH SCIENCE

by

Megan R. K. Seritan

December 2022

The Dissertation of Megan R. K. Seritan
is approved:

Professor Ian Garrick-Bethell, Chair

Professor Francis Nimmo

Professor Emeritus Robert Coe

Assistant Professor Sonia Tikoo-Schantz

Peter Biehl
Vice Provost and Dean of Graduate Studies

Table of Contents

List of Figures

List of Tables

Abstract

The geologic context of lunar magnetic anomalies

by

Megan R. K. Seritan

The goal of this thesis is to investigate the geologic origins of two different lunar magnetic anomalies: Reiner Gamma on the lunar nearside, and the Gerasimovich-area anomalies on the farside. Chapters 2 and 3 are concerned with Reiner Gamma, while Chapter 4 is concerned with the Gerasimovich-area anomalies. Understanding the geologic origins of these lunar magnetic anomalies is key to progressing our understanding of the Moon's magnetic history, and this work carries out these investigations using data from lunar orbiters.

In Chapter 2, I present evidence that the magnetic anomaly Reiner Gamma overlies a relative-negative Bouguer gravity anomaly. This gravity anomaly is likely a buried impact crater, and I determined its age, and thus the age of the Reiner Gamma magnetic source bodies, to be between ∼3.3 Ga and ∼3.9 Ga, which are the approximate temporal bounds of mare volcanism. This range of ages coincides with the putative high-field era of the lunar dynamo (∼3.56–3.9 Ga), thus, the high magnetization of Reiner Gamma could be due to deposition during a time of a high-magnitude ambient field.

In Chapter 3, I present observations that a portion of Reiner Gamma appears to have been demagnetized by the emplacement of a dome in the nearby Marius Hills

volcanic complex. I created three different models to determine if the observed magnetic anomaly was diminished by thermal demagnetization. First, I created a flexure model, which approximated the dome as a buried laccolith and determined the burial depth of the laccolith based on its surface expression. Second, I created a thermal model, which determined the time-temperature history of areas around the laccolith. Third, I created a dipole model that simulated thermal demagnetization via decreasing the moments of some of the source dipoles. These three models, taken together, suggest that thermal demagnetization did occur at Reiner Gamma, and we use this result to estimate source body burial depths of $<\sim$2 km, age of $\sim$3.5-3.9 Ga, and a magnetization of $\sim$3.6 A/m.

In Chapter 4, I present the observation that in the region of the Gerasimovich magnetic anomalies, areas of high magnetic field tend to overlie areas of low surface slope. Because the Gerasimovich region is antipodal to the Crisium basin, other work has suggested that the magnetic anomalies could be due to highly magnetic antipodal ejecta (Hood and Artemieva, 2008; Lin et al., 1988; Wakita et al., 2021). My work validates this antipodal ejecta hypothesis and estimates a magnetized layer thickness between $\sim$0.8-1.2 km and $\sim$2.4 km and a source body magnetization of $\sim$3-5 A/m.

To Stefan,

my coauthor in life

Acknowledgments

One of classes that you take during your first quarter as a UCSC EPS student is called Foundations, and in it each professor in the department gives a lecture about their particular subfield and what research they're working on. Ian was the very first lecture in Foundations in Fall quarter 2016, and, just like that, I decided that I wanted to switch from seismology to planetary science. I am incredibly grateful to have had Ian as an advisor; he graciously accepted me as a "surprise" student who had no experience in planetary science prior to grad school. They say that your advisor makes or breaks your grad school experience; Ian certainly made mine.

In the same vein, I want to thank the Planetary group who welcomed me with open arms. Many thanks to to Francis, who advised me on my second project for my qualifying exam, and to Xi, the first professor that I TA'd for. And to the new and current EPS students & alums: Rachel, Szilard, Coby, Brynna, Huazhi, Sarah, Adrienne, Xinting, Pranvera, Nathan, Linfeng, Nick, Jack, Carver, Doug, and more. You all inspire me to work hard and play hard.

Any acknowledgements section by an EPS student would be incomplete without thanking the EPS staff who make everyone's lives an order of magnitude easier. Thank you to Jennifer for your administrative support and kind chats, and thank you to Amy, whose patience with my questions is boundless.

Thank you to my closest friends for laughing with me, crying with me, and supporting me through every season of grad school. To Anna: I'm so grateful to call you

my friend; our elementary school selves would be proud of us. To Adrienne: thank you for your garden advice, your game instructions, and your kindness. I'll always treasure our Highway 17 commute chats. To Claire: I am eternally grateful to have spent grad school near you. Your presence is a gift and I'll always hold our weekly MHA nights in my heart.

An especially a huge thank you to my parents, Craig and Lori Kelley. You've encouraged my journey through science every step of the way and I'm so lucky for your constant support. Thank you to my in-laws, Marius (the Marius Hills are named after you in my mind) and Andreea Seritan for your kindness and support. Thank you to my extended family for supporting me from New Mexico: Lene Bryson, Fred and Virginia Kelley, and everyone in the generations below the grandparents.

And finally, a most profound thank you to my husband, Stefan. You've been there with me through every one of the 2,267 days of grad school and through 1,014 days of undergrad before that. You've celebrated each of my successes, dried my tears, and have been a joy to share life with. I wouldn't be who I am today without you.

Chapter 1

Introduction

Magnetic fields are one of the fundamental phenomena in the universe and are of critical importance to planetary science. The presence of magnetic fields, either in the form of a dynamo-generated global field or a localized crustal anomaly, can reveal information about a body's history and composition. This work focuses on magnetic fields as they relate to Earth's closest neighbor, the Moon. Since the Apollo era, we have known from orbital magnetometer measurements that the Moon possesses numerous crustal magnetic anomalies (Hood et al., 1979; Dyal et al., 1972). Previous work has investigated these magnetic anomalies and discovered surface markings, called lunar swirls, associated with some of them (Hood and Schubert, 1980), and noted that some magnetic anomalies are antipodal to large basins (Lin et al., 1988). In spite of this initial progress, the geologic origins of these anomalies are still not broadly understood, which hampers our ability to understand the Moon's magnetic history more fully. The Moon may have once had a global magnetic field driven by a dynamo, but there is contention

as to its mechanism (Dwyer et al., 2011; Evans et al., 2018), duration and strength (Evans and Tikoo, 2022; Suavet et al., 2013; Tikoo et al., 2014), and if it existed at all (Tarduno et al., 2021). Understanding the geologic origins of lunar magnetic anomalies offers a path forward to better understanding lunar magnetic history. Hypotheses for their formation include impact ejecta (Hood et al., 2001; Wieczorek et al., 2012) and volcanic materials (Hemingway and Tikoo, 2018; Purucker et al., 2012).

Recent lunar missions have provided orbital datasets that are a great improvement upon the datasets of the Apollo era in both resolution and coverage. The focus of this work is using these orbital datasets, among them topography, reflectance, gravity, and magnetic fields, to carry out careful investigations of the geologic settings of two different magnetic anomalies: Reiner Gamma, located on the nearside in Oceanus Procellarum, and the Gerasimovich magnetic anomalies, located on the farside to the west of the Orientale basin. The first project uses gravity data to infer that part of the Reiner Gamma magnetic anomaly overlies a buried crater. Constraining the formation time of the buried crater then constrains the formation time of the magnetic anomaly itself. The second project pursues the observation that part of the Reiner Gamma magnetic anomaly appears to have been thermally demagnetized by the emplacement of a nearby volcanic dome. By modeling the dome emplacement and demagnetization processes, we place constraints on the depth, age, and magnetization of the magnetic source bodies. The third project, rather than focusing on the Reiner Gamma magnetic anomaly, focuses on the Gerasimovich magnetic anomalies, which are antipodal to the Crisium basin. We present the discovery that the areas of high magnetic field are collocated

with the areas of low slope. This suggests that the magnetic source bodies underwent downslope movement after deposition, supporting the antipodal ejecta hypothesis for these anomalies. These three projects, taken together, represent a new level of detail in investigating the geologic contexts of individual lunar magnetic anomalies, which forwards our goal of understanding the Moon's magnetic and geologic histories.

Chapter 2

Gravity constraints on the age and formation of the Moon's Reiner Gamma magnetic anomaly

This chapter is a slightly modified reprint of work previously published as M. R. Kelley and I. Garrick-Bethell, I. (2020), Gravity constraints on the age and formation of the Moon's Reiner Gamma magnetic anomaly, *Icarus 338*, 113465.

Abstract

The Moon once possessed a dynamo that produced numerous magnetic anomalies in the lunar lithosphere. Determining the ages and magnetization strengths of these anomalies would constrain the timing and strength of the dynamo. Unfortunately, most anomalies are not associated with dated geologic features. Here we report that the north-

eastern portion of the Reiner Gamma magnetic anomaly overlies a relative-negative Bouguer gravity anomaly that we interpret to be a buried impact crater (consistent with Evans et al. (2016)). Reiner Gamma is associated with sinuous optical markings known as swirls, which are likely correlated with the underlying magnetization. These markings provide a higher resolution map of the magnetization than possible with existing field data. We present two arguments that suggest the crater overprinted by the Reiner Gamma swirl formed in a pre-existing flood basalt layer. Hence, we constrain the Reiner Gamma source body's age to be bounded by the approximate duration of mare volcanism, ∼3.3 Ga to ∼3.9 Ga. This range includes the putative high-field epoch of the Moon's dynamo (∼3.56–3.9 Ga), which could explain Reiner Gamma's high magnetization. Finally, we calculate the potential range of positions of the rim of the buried crater, and find that the main body of Reiner Gamma is likely outside the buried rim. This finding may be useful for constraining the origin of the Reiner Gamma magnetic source bodies.

2.1 Introduction

The Moon, although currently lacking a global magnetic field, features many localized magnetic anomalies that likely formed in the presence of an extinct dynamo (Arkani-Hamed and Boutin, 2014; Baek et al., 2019; Hood, 2011; Hood et al., 2001; Nayak et al., 2017). Determining the ages of anomaly source bodies would constrain when and how the Moon was able to sustain a dynamo with possibly Earth-strength

magnetic fields (Weiss and Tikoo, 2014). However, determining these ages is complicated by the fact that the geologic origins of lunar magnetic anomalies are unknown. Source body formation theories include either impact ejecta (Hood et al., 2001; Wieczorek et al., 2012) or volcanic materials (Hemingway and Tikoo, 2018; Purucker et al., 2012) that acquired a thermoremanent magnetization (TRM) in the Moon's ancient dynamo field. It is also possible that some anomalies are materials that acquired a TRM or shock-remanent magnetization (SRM) in a field amplified or produced by large impacts (Hood and Artemieva, 2008). Determining the ages of the anomalies could also help assess this latter hypothesis, as the ages of the Moon's largest basins are >3.7 Ga (Stöffler et al., 2006). Smaller impacts may also produce transient magnetic fields, but the short-lived nature of these fields would require any magnetization to be a SRM. For the strongest anomalies, SRM is not expected to be the dominant source of the magnetization, since SRM is a relatively inefficient magnetization process (Tikoo et al., 2015a).

Even if the geologic origins of the Moon's magnetic anomalies are unknown, constraints on their ages can be obtained by relating them to local geologic features with known ages. Lunar swirls, a class of lunar magnetic anomalies that show sinuous variations in albedo (Blewett et al., 2011), are particularly useful for this task. Because the swirls' variations in albedo are likely caused by a "mini-magnetosphere" that shields the surface from the darkening effects of the solar wind (Bamford et al., 2012; Deca et al., 2018; Hemingway and Garrick-Bethell, 2012; Hood et al., 1979; Hood and Schubert, 1980), swirl surface patterns are likely related to the shape of the near-surface magnetic

field. These near-surface magnetic fields are not readily observable at orbital altitudes. Thus, lunar swirls provide a higher-resolution correlation between magnetic field (and thereby source body geometry) and local geology than presently available from orbit.

One particular swirl, Reiner Gamma (Figs. 2.1 and 2.2), is near a diverse set of geologic features that could constrain the swirl's age, and thereby the age of the magnetizing field. Reiner Gamma can be divided into two parts, the elliptical southwestern region, which we refer to as the "main body", and the narrow and sinuous northeastern region, which we refer to as the "tail" (Fig. 2.2b, yellow labels). Southwest of the main body there is a cluster, approximately ∼100 km in extent, of smaller swirls. Lee et al. (2019) showed that one of the southernmost smaller swirls in this region is magnetized in the same direction as the main body, suggesting that their source bodies may have formed at the same time. A useful geologic feature near the Reiner Gamma tail is the Marius Hills, a large volcanic province (Figs. 2.1 and 2.2b). Recent work has found that portions of the Reiner Gamma tail were demagnetized by small volcanoes in the Marius Hills (Kelley et al., 2018), and that the relative-positive Bouguer anomalies observed at the Marius Hills are consistent with intruded dike swarms (Deutsch et al., 2019). Here we report the discovery of another geologic feature near Reiner Gamma that can be used to constrain the swirl's age: a circular relative-negative Bouguer gravity anomaly that underlies the Reiner Gamma tail (Figs. 2.1b, d and 2.2c), herein referred to as the Reiner Gamma quasi-circular mass anomaly (RG-QCMA). One interpretation of this low in Bouguer gravity is an impact crater completely buried by basalt. Previously, Evans et al. (2016) identified RG-QCMA as a possible buried impact crater, but they

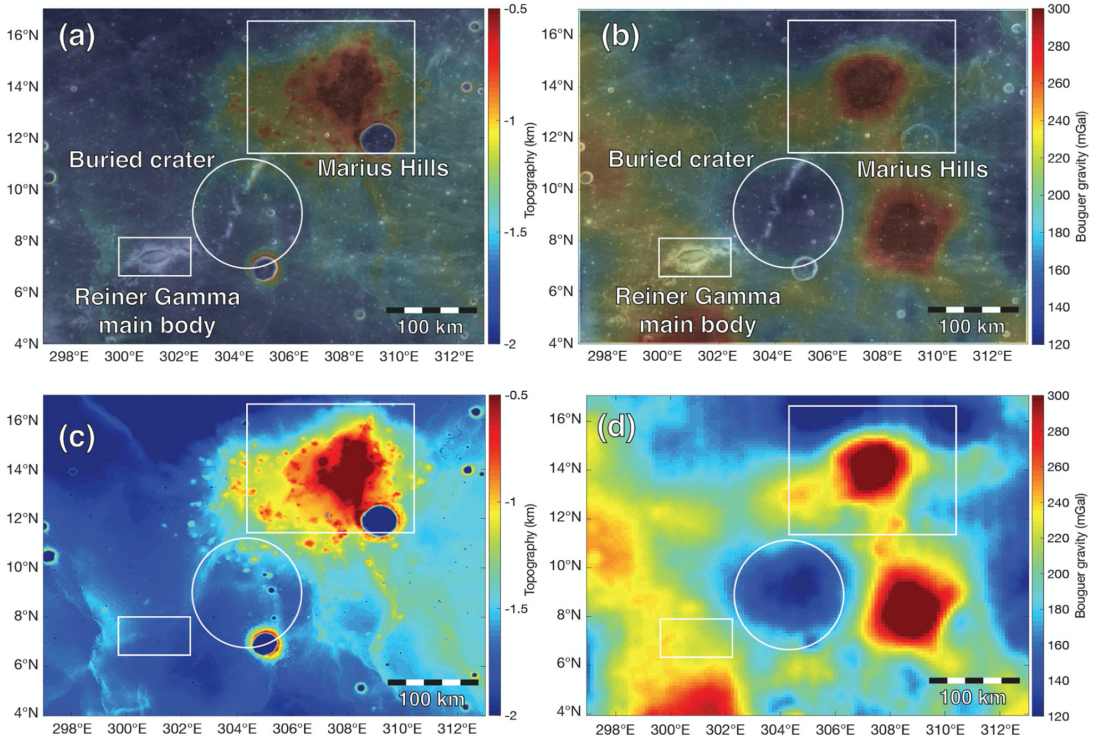

Figure 2.1: Reiner Gamma swirl, RG-QCMA, and the Marius Hills. (a) 750 nm Clementine reflectance overlain with LRO LOLA topography. (b) 750 nm Clementine relfectance overlain with GRAIL Bouguer gravity. (c) LRO LOLA topography. (d) GRAIL Bouguer gravity. RG-QCMA, interpreted to be a buried impact crater, is indicated by the white circle.

did not consider its importance in the formation of Reiner Gamma swirl.

In the next sections we discuss the data supporting the hypothesis that RG-QCMA is a buried impact crater – which is a critical assumption for all of our conclusions. We then show that the Reiner Gamma magnetic source bodies must postdate this crater, which implies that the source bodies must be located within the flood basalts that have buried the crater, i.e., that the source bodies likely formed during mare volcanism. The potential range of formation ages of the source bodies includes the putative high field (>50 μT) epoch between ~3.56–3.9 Ga (Weiss and Tikoo (2014)). Additionally, we find

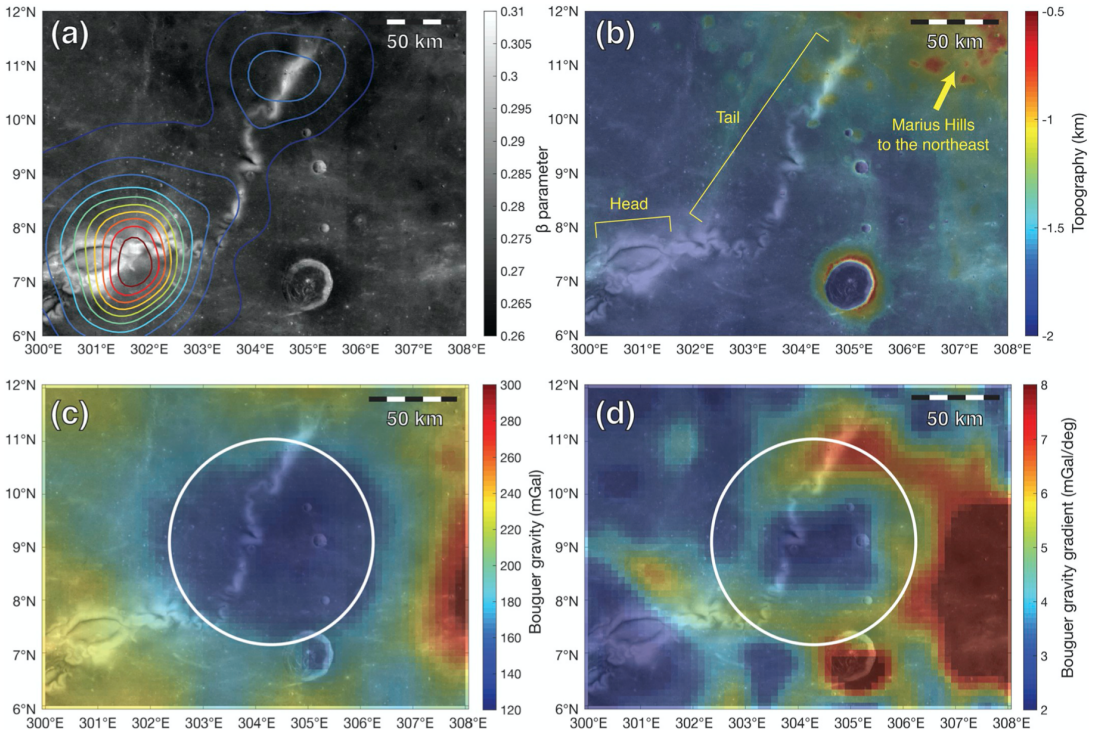

Figure 2.2: Reiner Gamma swirl. (a) Spectral parameter β, a combination of 750 nm and 950 nm reflectance that highlights lunar swirls. The contour lines show the total magnetic field. The minimum contour is 3.4 nT, the maximum contour is 34.2 nT, the contour interval is 3.4 nT, and the altitude is 20 km. (b) β parameter overlain by LRO LOLA topography. The edge of the Marius Hills volcanic complex is seen in the northeast corner. (c) β parameter overlain by GRAIL Bouguer gravity. (d) β parameter overlain by the 2D gradient of GRAIL Bouguer gravity. The white circle in panels (c) and (d) indicates the relative-low anomaly, interpreted to be a buried impact crater.

that the main body of Reiner Gamma is located outside of the buried crater's rim.

2.2 Data & analysis

2.2.1 Data

We use GRAIL Bouguer gravity data (Zuber et al., 2013) from a degree and order 900 spherical harmonic model, which was truncated to degree and order 600. This gridded Bouguer gravity map was produced with a resolution of 8 pixels per degree (ppd, Figs. 2.1b, 2.1d, 2.2c, 2.5c, 2.6c, 2.7b, and 2.7d, PDS product gggrx_0900c_boug_l600). We use Lunar Reconnaissance Orbiter (LRO) Lunar Orbiter Laser Altimeter (LOLA) topography data (Smith et al. (2010)) at a resolution of 64 ppd (Figs. 2.1a, 2.1c, 2.2b, 2.5b, 2.6b, 2.7a, and 2.7c), Lunar Reconnaissance Orbiter Camera (LROC) wide-angle camera (WAC) images (Robinson et al., 2010) at a resolution of 152 ppd (Figs. 2.5a and 2.6a), and a spherical harmonic model based on magnetic field data from Kaguya and Lunar Prospector datasets (Tsunakawa et al., 2015), expanded to degree and order 450 (Fig. 2.2a). We also use the spectral parameter β, which is a combination of 750 nm and 950 nm Clementine reflectance values (Hemingway et al., 2015) with a resolution of 151.5 ppd. The parameter β is meant to highlight lunar swirls (Figs. 2.2 and 2.7) and suppress bright, fresh craters.

2.2.2 Crater evidence and formation mechanisms

For our analysis, we assume that RG-QCMA (Figs. 2.1b, 2.1d, and 2.2c) is a buried impact crater, since the vast majority of circular features seen in gravity data are impact features (Evans et al., 2016). Since a false positive interpretation of a QCMA as an impact crater is possible, we sought additional evidence supporting this assumption. Firstly, we looked for the presence of concentric wrinkle ridges at RG-QCMA, which are found at partially buried impact craters of similar size (e.g. Flamsteed P at 3.2°S, 315.9°E, 112 km diameter). We found no concentric wrinkle ridges at RG-QCMA, but we also found that the nearby partially buried craters Eddington and Russell (which are similar in size to our putative buried crater, Fig. 2.3) lack wrinkle ridges. Hence, wrinkle ridges are not a defining feature of all buried craters. Secondly, we compared the putative buried crater's estimated rim height with basalt thicknesses in the region. The height of the crater's rim is less than the basalt thicknesses in the region (Section 2.2.3). Together, these two lines of evidence show a buried impact crater at RG-QCMA is plausible.

There are two models that can be used to explain how an impact crater creates a relative-positive or a relative-negative Bouguer anomaly. The first model applies to buried craters and depends on the pre-existing stratigraphy. This model was described by Evans et al. (2016) and proposes that a relative-negative Bouguer anomaly arises from a pre-existing basalt layer overlying a lower-density anorthositic crust, which was then impacted and covered with additional basalt (Fig. 2.4). To understand this,

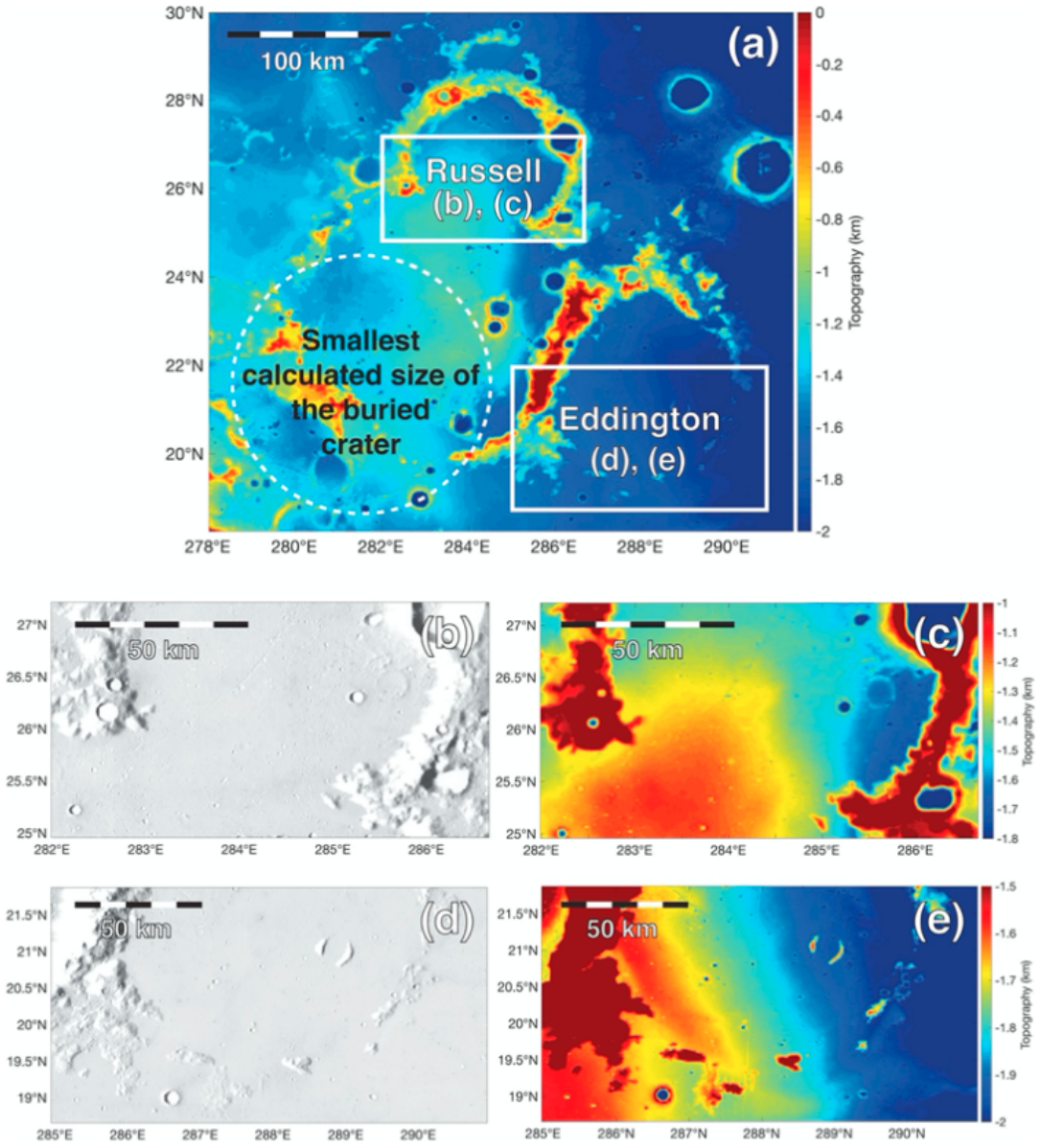

Figure 2.3: Partially buried craters Russell and Eddington. Note the lack of concentric wrinkle ridges in the buried sections of these craters. (a) Context map showing Russell to the north and Eddington to the south, as compared to the size of the smallest diameter calculated for the Reiner Gamma buried crater (white dashed circle). (b) Negative-color LRO WAC image showing the southern region of Russell. (c) LRO LOLA topography map of the southern region of Russell. (d) Negative-color LRO WAC image showing the southern region of Eddington. (e) LRO LOLA topography map of the southern region of Eddington.

consider an impactor encountering only lower-density crustal material. If the resulting crater was then filled with higher-density basalt, the excess of higher-density material inside the crater relative to the background would cause a relative-positive Bouguer anomaly. However, if the impact was into pre-existing basalt overlying crustal material, the background boundary between lower- and higher-density materials (Fig. 2.4, white dashed line) would be deeper than the crater floor. When the crater is subsequently buried by additional basalt, the uplifted floor and central peak of the crater, made of lower-density material, causes a relative-negative Bouguer anomaly. In Fig. 2.4, the orange (lower-density) material located above the white dashed line is what causes the relative-negative Bouguer anomaly.

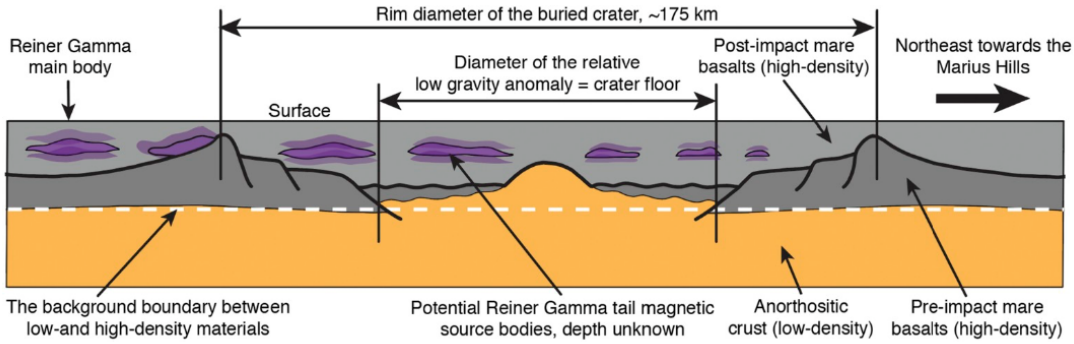

Figure 2.4: Cross-section showing the buried crater, based on Fig. 3b in Evans et al. (2016). Orange indicates lower-density anorthositic material, and shades of gray indicate higher-density mare basalts. The darker shade of gray indicates the mare basalts that were deposited prior to the impact. The impact caused an uplift of the anorthositic material in the center of the crater. The crater was then buried by additional higher-density mare basalts, indicated by the lighter shade of gray. The uplift of less-dense anorthositic material in the center of the crater above the background boundary between low- and high-density material (white dotted line) causes a relative low in Bouguer gravity. The purple objects indicate the possible location of magnetized materials comprising the Reiner Gamma magnetic anomaly. Figure not to scale.

The second model to explain how a crater produces a relative-negative or a relative-positive Bouguer anomaly invokes the pre-existing porosity of the target layer. As explained in Milbury et al. (2015), relatively low pre-existing crustal porosities (less than ∼7%) may produce relative-negative Bouguer anomalies because after the transient crater's collapse, dilatant expansion increases pore space (and thus produces a lower density relative to surroundings) in the displaced material. In contrast, relatively high pre-existing porosities (greater than ∼7%) may produce relative-positive Bouguer anomalies because the impact's shock wave crushes out pore space (and thus creates a higher density relative to surroundings) at the center of the crater. This model suggests that the pre-existing porosity in the area of RG-QCMA may have been low, which would have produced the observed relative-negative Bouguer anomaly. This low porosity may have been due to extensive basaltic eruptions that intruded the early crust and accumulated on its surface. This interpretation is supported by the high surface density in this region (greater than ∼2600 kg m^{-3}) (Besserer et al., 2014), and the substantial thickness of the basalts near the Marius Hills (3–4 km) (Gong et al., 2016). The relative-negative Bouguer anomaly would still be observed even after the impact crater was buried with basalt.

The key implication of both RG-QCMA formation models is that the putative impact crater near Reiner Gamma likely formed on a pre-existing mare surface. The stratigraphic and temporal implications of this finding for the Reiner Gamma source bodies are discussed in Section 2.3.1.

2.2.3 RG-QCMA/buried crater rim diameter

Estimating the topographic rim diameter of the buried crater may also affect our interpretation of the spatial distribution of the Reiner Gamma magnetic source bodies. For example, the source of the elliptical main body of Reiner Gamma may be a magnetized melt sheet from an oblique impact (Garrick-Bethell and Kelley, 2019). A crater rim that directly intersects the main body might be inconsistent with this hypothesis, since such topography might have altered the elliptical crater's formation, possibly breaking the high degree of symmetry in the melt sheet inferred by Garrick-Bethell and Kelley (2019). Since this elliptical crater's diameter is only ∼25% of the putative buried crater that is the source of RG-QCMA, and formed by an oblique impact that yielded a shallow impact crater, it is unlikely that any relative-negative Bouguer anomaly from this crater would be resolvable in GRAIL data. Alternatively, Reiner Gamma may be magnetized volcanic material, such as a lava tube or dike (Hemingway and Tikoo, 2018). The buried RG-QCMA crater rim could have affected the formation of such volcanic structures; for example, a surface lava flow may have been unable to flow over the crater rim. The implications of the relationship between the buried rim and the swirl pattern will be discussed further in Section 2.3.2, while the rest of this section will be dedicated to estimating the location and diameter of the buried crater rim.

We use two different methods to determine the buried crater's rim diameter. Method 1 assumes that the relative-negative gravity anomaly arises predominantly from

the crater floor uplift scenario described in Evans et al. (2016) (see Section 2.2.2). In this case, we first take the two-dimensional gradient of the Bouguer map and measure the diameter of the maxima seen in the gradient map (Fig. 2.2d). This diameter is assumed to represent the edge of the causative source body (Blakely, 1996), which we assume herein to be equivalent to the floor diameter. Known crater scaling relationships are then used to calculate the rim diameter given the floor diameter.

In Method 2, we assume that RG-QCMA arises from the putative relative increase in porosity that followed the impact (Section 2.2.2). In this case, we derive relationships between the topography and gravity anomalies of exposed craters of a similar size, and then apply them to RG-QCMA. In contrast to the relative-negative anomaly at RG-QCMA, these exposed craters possess relative-positive Bouguer anomalies. However, we argue that they are valid to compare to RG-QCMA because the competing processes that determine whether a crater shows a relative-negative or relative-positive Bouguer signal (compaction vs. dilatant bulking) occur over similar spatial scales within the crater.

For Method 1, we begin by producing a map of the magnitude of the gradient at each point of the scalar field of Bouguer gravity values in the area of RG-QCMA. In this map (Fig. 2.2d), a quasi-circular ridge of maxima can be seen encircling the location of the depression in Bouguer gravity. Once we determined the locations of all local maxima along this ridge, the ridge's diameter was obtained with a least-squares circle-fitting algorithm (Pratt, 1987). The fit, as with all other fits in this work, was performed in an orthographic projection, preventing map distortion from affecting the fit

results. Values obtained by this method will be referred to as "gravity-gradient" values. For RG-QCMA, we obtained a gravity-gradient floor diameter of 122 km centered at 8.96°N, 305.01°E (Fig. 2.2c and 2.2d, white circles). For comparison, when RG-QCMA was first identified in Evans et al. (2016), they inferred its diameter to be 118 km.

We then use our gravity-gradient crater floor diameter in the following crater scaling relationship, where floor diameter is D_{floor} and rim diameter is D_{rim}:

$$D_{\text{floor}} = D_{\text{rim}} - 1.84 \times D_{\text{rim}}^{\frac{2}{3}} \tag{2.1}$$

This equation, derived by Evans et al. (2016), combines assumptions made in separate studies of crater scaling relationships. Firstly, it is assumed that the total rim diameter of the crater is the sum of the floor diameter and two terrace widths. This assumption likely holds for the buried crater because its diameter is within the transition between the complex crater regime and the peak-ring basin regime. The transition between the complex crater regime and the peak-ring basin regime occurs at a crater rim diameter of approximately 200 km (Baker et al., 2011). Secondly, a known scaling relationship between the terrace widths and the rim diameter, valid for rim diameters up to 350 km (Melosh, 1989; Pike, 1977), can be used to write the floor diameter in terms of the rim diameter (Evans et al., 2016). Using the equation above with $D_{\text{floor}} = 122$ km, we obtain $D_{\text{rim}} = 181$ km. The same scaling calculation can be applied to the floor diameter of 118 km obtained by Evans et al. (2016) yielding a rim diameter of 176 km. These rim diameters are summarized in the top half of Table 2.1.

For Method 2, we surveyed unburied lunar craters with topographic rim diameters

Method 1: Eqn. 2.1

	Result of crater scaling relationship
D_{floor} = gravity gradient buried floor crater, 122 km	D_{rim} = 181 km
D_{floor} = Evans et al. (2016) buried crater floor, 118 km	D_{rim} = 176 km

Method 2: Eqn. 2.2

	$D_{\text{rim, ref}}/D_{\text{floor, ref}}$ = Joliot rim/floor, 164 km/100 km	$D_{\text{rim, ref}}/D_{\text{floor, ref}}$ = Compton rim/floor, 162 km/121 km
D_{floor} = gravity gradient buried floor crater, 122 km	D_{rim} = 200 km†	D_{rim} = 163 km
D_{floor} = Evans et al. (2016) buried crater floor, 118 km	D_{rim} = 194 km	D_{rim} = 158 km†

Table 2.1: Calculated rim diameters for the putative buried crater located at RG-QCMA. The upper portion of the table shows the buried crater rim diameters calculated using a crater scaling relationship (Eqn. 2.1). The lower portion of the table shows the buried crater rim diameters calculated by scaling the gravity-gradient floor diameters of Joliot and Compton to the buried crater (Eqn. 2.2). The values with a dagger indicate the largest and smallest values in the table, which define the edges of the annulus plotted in Fig. 2.7.

between 150 km and 250 km, a range which includes the approximate diameter of the buried crater. We selected two craters, Joliot and Compton, for comparison with RG-QCMA because they display a quasi-circular Bouguer gravity signal clearly associated with the crater. Joliot has a rim diameter of 164 km (Fig. 2.5), and Compton has a rim diameter of 162 km (Fig. 2.6). Both of these craters have relative-positive Bouguer anomalies, presumably due to relative changes in porosity (section above). No other craters in this size range displayed clear relative-negative Bouguer anomalies without truncating the lower limit of the range of the included spherical harmonic degrees.

We performed a simple check to determine if the gravity gradient method described above is successful in inferring topographic properties of these craters. We measured the topographic floor diameters of these craters with LRO LOLA topography data, obtaining 123 km and 131 km for Joliot and Compton, respectively. Next, we calculated the diameter of each crater's ring of maxima in the two-dimensional Bouguer gravity gradient (as for the buried crater, above). The resulting gravity-gradient floor diameter values for Joliot and Compton are 100 km and 121 km, respectively (Figs. 2.5 and 2.6, overlain circles). We find the ratio between the gravity-gradient diameter and the true topographic floor diameter for both Joliot and Compton are similar: Joliot's gravity-gradient diameter is 81% of its topographic floor diameter, and Compton's gravity-gradient diameter is 92% of its topographic floor diameter. This supports our assumption of these gravity anomalies arising from a self- consistent process, i.e. changes in the subsurface porosity structure.

Finally, we use the topographic rim and gravity gradient floor diameter of Jo-

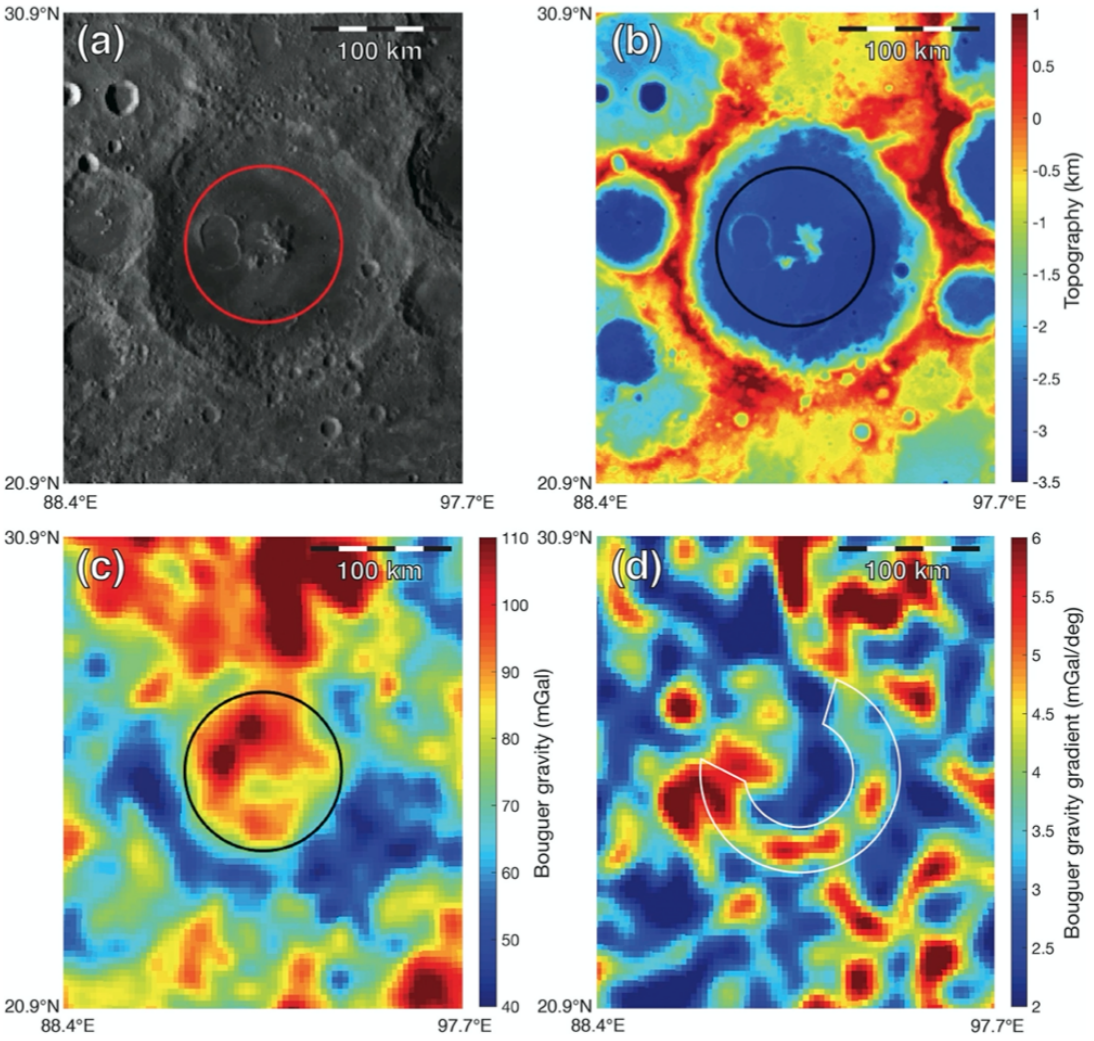

Figure 2.5: Joliot crater, located at 25.8°N, 93.1°E. The overlaid circle in (a), (b), and (c) indicates the diameter of the ring of maxima in the 2D Bouguer gradient (referred to as the gravity-gradient diameter in the text), which we interpret to represent the edge of the crater floor. (a) WAC image of Joliot. (b) LRO LOLA topography map of Joliot. (c) GRAIL Bouguer gravity map of Joliot. (d) GRAIL Bouguer gravity 2D gradient map of Joliot. The white semicircular arc shows the ridge of maxima that were fit.

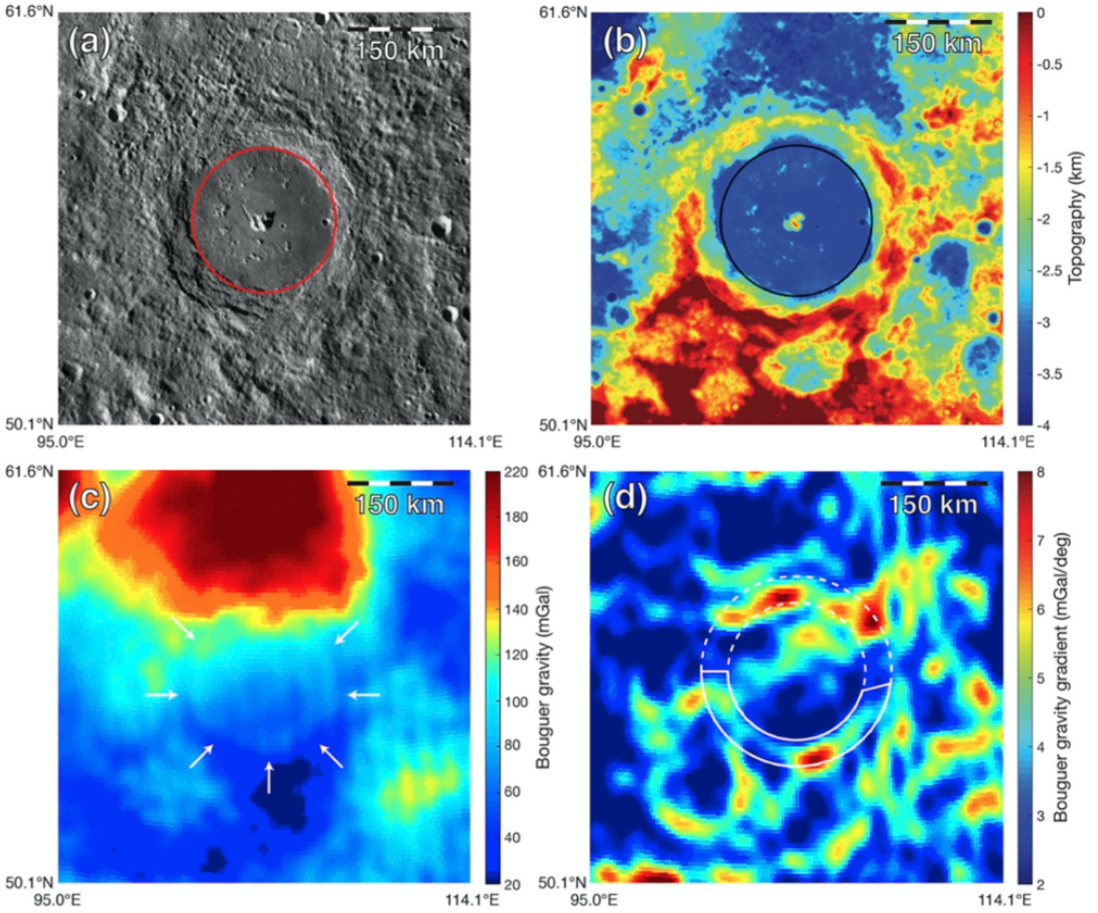

Figure 2.6: Compton crater, located at 55.3°N, 103.8°E. The overlaid circle in (a) and (b) indicates the diameter of the ring of maxima in the 2D Bouguer gradient (referred to as the gravity-gradient diameter in the text), which we interpret to represent the edge of the crater floor. (a) WAC image of Compton. (b) LRO LOLA topography map of Compton. (c) GRAIL Bouguer gravity map of Joliot, with white arrows showing the approximate extent of the relative-positive Bouguer anomaly. (d) GRAIL Bouguer gravity 2D gradient map of Joliot. The solid white semicircular arc shows the ridge of maxima that were fit, while the dashed white lines indicate the extension of the fit area into a circle.

liot and Compton to estimate the buried crater rim diameter via the following scaling relationship:

$$D_{\text{rim}} = D_{\text{floor}} \cdot \frac{D_{\text{rim, reference}}}{D_{\text{floor, reference}}} \tag{2.2}$$

The first term on the right-hand side of Eq. 2.2, D_{floor}, the buried crater floor diameter, can be two different values: 122 km for this study's gravity-gradient value, or 118 km, as inferred from the gravity gradients performed by Evans et al. (2016). The numerator on the right-hand side of Eq. 2.2, $D_{\text{rim, reference}}$, can be the rim diameter of either Joliot or Compton: 164 km or 162 km, respectively. The denominator on the right-hand side of Eq. 2.2, $D_{\text{floor, reference}}$, can be the gravity-gradient floor diameter of either Joliot or Compton: 100 km or 121 km, respectively (both the numerator and the denominator refer to the same reference crater when calculating D_{rim}). In total, we calculated four buried crater rim diameters using Eq. 2.2, (1) this study's gravity-gradient D_{floor} with the topographic rim and gravity-gradient floor for Joliot, (2) this study's gravity-gradient D_{floor} with the topographic rim and gravity-gradient floor for Compton, (3) the Evans et al. (2016) D_{floor} with the topographic rim and gravity-gradient floor for Joliot, and (4) the Evans et al. (2016) D_{floor} with the topographic rim and gravity-gradient floor values for Compton. The resulting four buried crater rim values, summarized in the lower portion of Table 2.1, are in addition to the rim diameters calculated using the gravity-gradient D_{floor} values in the canonical crater scaling relationship (upper portion of Table 2.1). With six different potential buried crater rim diameters, it is enlightening to plot only the smallest and the largest values to see the range over which the buried rim could be located (Fig. 2.7).

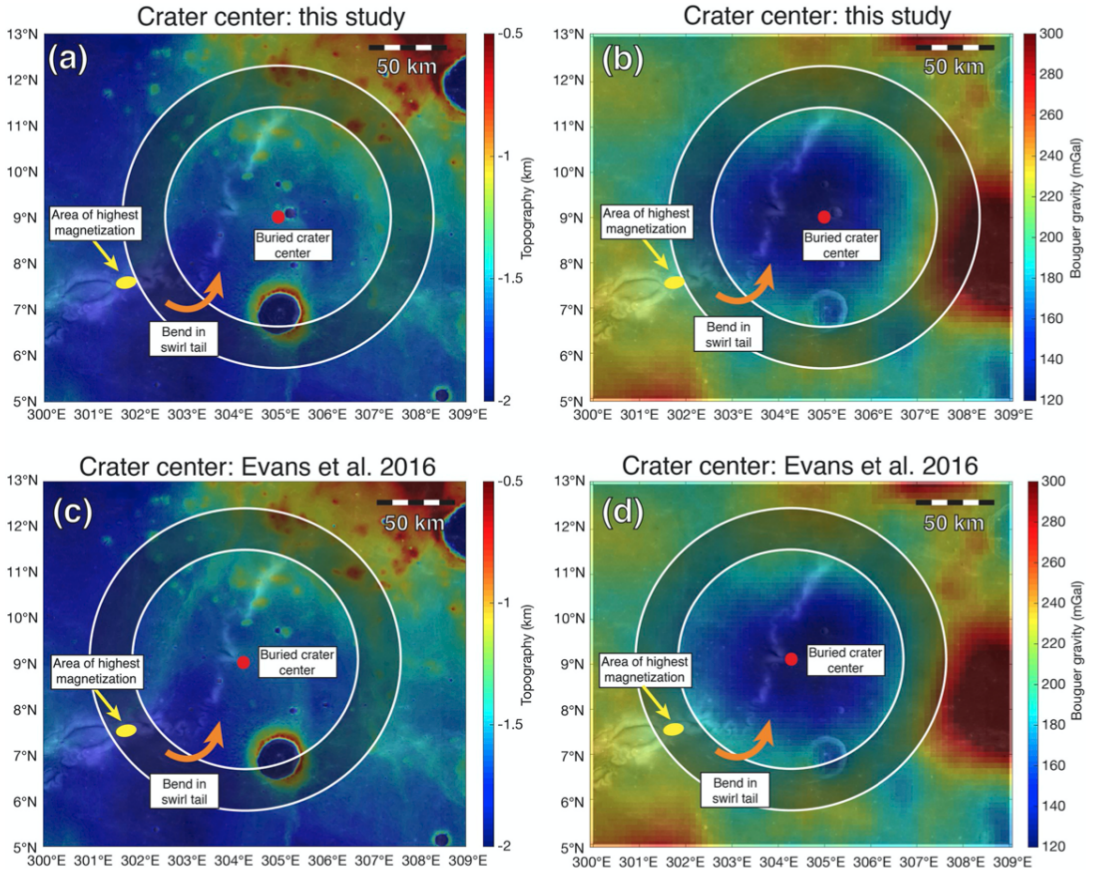

Figure 2.7: Maps showing the range of potential locations for the rim of the buried crater (white circles) in relation to Reiner Gamma swirl (see Table 2.1). (a) β parameter overlain by LRO LOLA topography with potential crater rims centered on the crater fit latitude/longitude as found in this study: 8.96°N, 305.01°E. (b) Same as panel (a) but for a map of GRAIL Bouguer gravity. (c) β parameter overlain by LRO LOLA topography with potential crater rims centered on the crater latitude/longitude as found in Evans et al. (2016): 9.1°N, 304.3°E. (d) Same as panel (c) but for a map of GRAIL Bouguer gravity.

The calculated buried crater rim diameters can be centered either on the coordinates of this study's best-fit gravity-gradient maximum diameter, 8.96°N, 305.01°E, or on the coordinates of the relative-negative Bouguer anomaly as reported by Evans et al. (2016), 9.1°N, 304.3°E. The crater center from this study is located farther to the south and east by 4 km and 22 km, respectively (Fig. 2.7, central red dots). While the difference in latitude between the two potential centers does not have a large effect on the buried crater's rim position relative to the main body of Reiner Gamma swirl, the difference in longitude changes where the maximum and minimum possible rim diameter values intersect the swirl (discussed further in Section 2.3.2). The difference in longitude also changes the locations where the potential rim diameters overlap with a relative-positive Bouguer anomaly located to the east (Fig. 2.7b). As discussed previously, this anomaly may be due to intruded dike swarms associated with Marius Hills volcanism (Deutsch et al., 2019). However, the volcanism that created this positive anomaly need not have affected the RG-QCMA, as the RG-QCMA signal is determined by the buried crater floor diameter, not its rim diameter.

Now that a family of potential buried crater rim diameter values has been calculated, we can briefly return to our assumption that RG-QCMA is in fact indicative of a buried impact crater (see Section 2.2.2). One test of this assumption is that the rim height of the putative buried crater is less than the mare basalt thickness in this region of Oceanus Procellarum. The largest possible buried crater rim diameter calculated above is 200 km. This rim diameter value can be used to calculate the crater rim height

above the surrounding terrain via another crater scaling relationship (Pike, 1977):

$$h_r = 0.236 \cdot D_r^{0.399} \tag{2.3}$$

For $D_r = 200$ km, the resulting rim height is $h_r = 2$ km. The basalts of Oceanus Procellarum around the Marius Hills, which are immediately northeast of RG-QCMA, are approximately 3–4 km thick (Gong et al., 2016). Thus, our impact crater assumption passes the rim burial test.

2.3 Discussion

2.3.1 Temporal implications

Our interpretation of the geologic sequence of events at RG-QCMA is as follows: (1) The formation of the underlying anorthositic crust. (2) The onset of mare volcanism and the deposition of pre-crater basalt. (3) The impact that formed the crater. (4) The deposition of post-crater basalt, burying the crater.

The putative buried crater must predate the magnetic source bodies because the depth of the transient cavity of the buried crater is greater than the maximum depth of the source bodies. We first estimate the diameter of the transient cavity from the buried crater's rim diameter (assumed here to be 158 km, see Section 2.2.3), using equation 6.2 from Melosh (2011), yielding 105 km. Using the approximation that the transient cavity depth is 3/10 times its diameter, we obtain a depth of 31 km (via equation 5.5.4 of Melosh (1989)). Any magnetic source bodies shallower than ∼31 km at the time of impact would be either destroyed or brecciated and no longer produce a coherent

magnetic signature. The maximum depth of the top of the magnetic source bodies can be estimated by measuring the bright-to-dark transition length scale of the swirl (Hemingway and Tikoo, 2018). For the Reiner Gamma tail, this length scale is at a maximum ∼5 km; thus, the source bodies must have been deposited after the impact.

Since the buried crater must predate the deposition of the Reiner Gamma magnetic source bodies, the source bodies must lie somewhere within the post-impact basalts that bury the crater. Note that in general, mare basalts themselves are not strongly magnetic (Shea et al., 2012; Suavet et al., 2013; Tikoo et al., 2012; Weiss and Tikoo, 2014), and are not expected to be source bodies except in cases of exotic processes (Hemingway and Tikoo, 2018). While we do not know the age of the lowest layers of basalt, a reasonable upper bound on the age of RG-QCMA, and thereby the Reiner Gamma source body, is the age of the oldest lunar basalts. The oldest known lunar basalts are small clasts with ages up to 4.35 Ga (Terada et al., 2007; Taylor et al., 1983; Dasch et al., 1987), and cryptomare with surface ages up to 4.0 Ga (Whitten and Head, 2015). However, a more reasonable upper bound on the age of Reiner Gamma is ∼3.9 Ga, which marks the onset of most volcanism (Hiesinger et al., 2011; Whitten et al., 2011; Whitten and Head, 2015). Previous work has suggested that features like Reiner Gamma could potentially be ejecta from the South Pole–Aitken basin (Wieczorek et al., 2012). If the South Pole–Aitken basin is older than 3.9 Ga (Garrick-Bethell and Kelley, 2019), then the Reiner Gamma source body cannot be ejecta from the South Pole–Aitken basin. Our age range does permit Reiner Gamma source material to be ejecta from the Imbrium basin, as proposed by Hood et al. (2001).

The minimum age of RG-QCMA can be constrained by the age of the surface basalts overlying Reiner Gamma. This age can be constrained by the crater density statistics overlying the Reiner Gamma source body, implying 3.3 Ga (Hiesinger et al., 2011). If the Reiner Gamma source body is volcanic material intruded beneath the surface at some unknown time, it could make this minimum age inapplicable. Most of the volcanism related to the Marius Hills complex occurred between 3.2 and 3.8 Ga (Kiefer, 2013; Wilhelms et al., 1987). If the Reiner Gamma source body is volcanic, it is likely related to the volcanism in the nearby Marius Hills. In this case, the age of Marius Hills volcanism does not substantially widen the potential age of the Reiner Gamma source body: 3.2 Ga rather than 3.3 Ga (note that if the source bodies are volcanic this age constraint holds regardless of whether RG-QCMA is in fact a buried impact crater). The total inferred range of ages for the Reiner Gamma source body covers both the high-field epoch of the Moon's global magnetic field (∼3.56 Ga to 3.9 Ga) as well as times when the intensity of the field was much lower (∼3.3 Ga to 3.5 Ga). The high inferred magnetization of the Reiner Gamma source body (Garrick-Bethell and Kelley, 2019) can be more easily explained if the source body was deposited and magnetized during the high-field epoch.

2.3.2 Spatial implications

The elliptical main body of Reiner Gamma does not directly overprint any of the potential buried crater rims found in this study (Fig. 2.7). The smallest potential buried crater rim diameter, when centered on the best-fit circle from this study, intersects the

swirl near where the west-to-east path of the tail abruptly turns ∼60° towards the northeast (Fig. 2.7, orange curved arrow). For potential buried crater rims centered on the coordinates given in Evans et al. (2016), the largest potential buried crater rim diameter intersects the swirl near the region of highest magnetization (Fig. 2.7, small yellow ellipse), but does not directly cross through the elliptical main body. This finding does not contradict the proposal that the main body of the swirl could be an elliptical melt sheet from an oblique impact (Garrick-Bethell and Kelley, 2019). That is, the putative elliptical crater formed from such a highly oblique impact might not have assumed the highly symmetric form it is inferred to presently possess, if the impactor had impacted the RG-QCMA crater rim.

2.4 Conclusions

The northeastern portion of Reiner Gamma lunar swirl is superposed on a circular Bouguer anomaly, referred to as RG-QCMA, which may be a buried impact crater. The relative-negative value of RG-QCMA implies that the impact occurred onto a pre-existing basalt layer. We constrain the source body's age to be between and ∼3.3 Ga (the age of the surface basalts in this region) and ∼3.9 Ga (the age of the onset of most volcanism). The range overlaps with the lunar dynamo's putative high-field epoch between ∼3.56 and 3.9 Ga. This could explain the previously inferred high values of magnetization at Reiner Gamma (Garrick-Bethell and Kelley, 2019). This age range likely excludes ejecta from the Moon's oldest basin, South Pole-Aitken, as the source of

the magnetic source bodies. Finally, the main portion of Reiner Gamma falls outside the rim of the buried crater, which may constrain its formation mechanism.

Chapter 3

Modeling thermal demagnetization at the lunar swirl Reiner Gamma

This chapter is a slightly modified reprint of work submitted as M. R. K. Seritan and I. Garrick-Bethell, I. (2022), Volcanic thermal demagnetization of the Reiner Gamma magnetic anomaly, *Icarus (in review)*.

Abstract

The age and formation mechanism of the Moon's lithospheric magnetic anomalies can give insight into the timing and age and strength of the Moon's past global magnetic field. Here we focus on the magnetic anomaly Reiner Gamma, which is associated with a bright sinuous pattern on the surface known as a lunar swirl. We propose that portions of Reiner Gamma's magnetic source bodies were demagnetized by the heat from volcanic domes in the Marius Hills. We model one of the domes as an

intrusive magma body and calculate its subsurface thermal evolution to constrain the volume and burial depth of the original magnetized source bodies. We infer that their burial depths of the remaining magnetized source bodies do not exceed ∼2 km, which is consistent with basalt thicknesses in this region and suggests that the source bodies were emplaced during mare basalt volcanism, which likely began at ∼3.9 Ga. We also estimate the swirl source bodies to have magnetizations of at least ∼3.6 A/m. The source depths and magnetization magnitudes are consistent with the Reiner Gamma magnetic source bodies becoming strongly magnetized during the Moon's major episode of mare volcanism, offering further support of a strong dynamo on the Moon for at least thousands of years at some point between ∼3.5-3.9 Ga. In turn, the implied lack of a strong field during demagnetization implies the Moon's dynamo may have been merely episodically strong, or had permanently weakened at the time of dome formation between 1.0-3.3 Ga.

3.1 Introduction & background

The Moon, at one point in its history, likely possessed a global magnetic field powered by a dynamo (Weiss and Tikoo, 2014). Understanding this global field would have implications for the timing of the Moon's heat loss (Evans et al., 2018; Evans and Tikoo, 2022), basic dynamo theory (Scheinberg et al., 2018), the presence of volatiles on the surface on the poles (Garrick-Bethell et al., 2019; Green et al., 2020; Tarduno et al., 2021), and possibly paleo-solar wind studies (Garrick-Bethell et al., 2019; Poppe et al.,

2021). In the wake of the global field's disappearance, numerous localized magnetic anomalies were left in the lithosphere (Arkani-Hamed and Boutin, 2014, 2017; Baek et al., 2017, 2019; Halekas et al., 2001; Hood, 2011; Hood et al., 2013, 2021a,b; Lee et al., 2019; Maxwell and Garrick-Bethell, 2020; Nayak et al., 2017; Oliveira et al., 2017; Oliveira and Wieczorek, 2017; Purucker and Nicholas, 2010). Constraining the geometry, depth, and formation time of the magnetic source bodies of these anomalies can constrain the timing and the strength of the Moon's past dynamo field (Garrick-Bethell and Kelley, 2019; Kelley and Garrick-Bethell, 2020; Wakita et al., 2021).

A useful tool to investigate the Moon's lithospheric magnetic anomalies is the sinuous pattern of albedo in the soil found at some anomalies, called lunar swirls (Blewett et al., 2011). The dominant formation hypothesis of these albedo patterns is that a "mini-magnetosphere" over the surface diverts solar wind ions, creating regions of the surface that do not darken over time (Hood and Schubert, 1980). Structures in the swirl pattern likely reflect the geometry of the magnetic field very near the surface (Deca et al., 2020; Hemingway and Garrick-Bethell, 2012; Poppe et al., 2016), perhaps at altitudes of $<$2 km (Garrick-Bethell and Kelley, 2019). This altitude is approximately ten times lower than available data from orbiting magnetometer measurements; hence the albedo pattern provides a higher resolution map of the magnetic field compared to such data. Thus, in some cases, lunar swirls can be used to more carefully investigate the geometry (Garrick-Bethell and Kelley, 2019), depth (Hemingway and Tikoo, 2018), and formation time (Kelley and Garrick-Bethell, 2020) of the source bodies. Alternative hypotheses for swirl formation include dust lofting (Garrick-Bethell et al., 2011) and anomalous

regolith properties (Hess et al., 2020). However, even if these hypotheses are correct in place of the mini-magnetosphere hypothesis, the field strength and geometry still likely controls the albedo of the surface.

In this work, we focus on a lunar swirl in the Marius Hills that appears to have been thermally demagnetized by nearby volcanoes. Thermal demagnetization of magnetic source bodies due to magmatic intrusions has been observed on Mars (Lillis et al., 2009, 2015) and on Earth is used in the baked contact test as a tool to determine if the magnetic remanence in an area was affected by volcanic intrusions (Buchan, 2007), but to our knowledge no such thermal demagnetization process has yet been reported on the Moon. If thermal demagnetization has occurred at the Marius Hills, the emplacement ages of the domes would constrain the epoch of low or zero ambient magnetic field. We can also constrain the volume of the source bodies to constrain their magnetization strength.

We develop a preliminary model for thermal demagnetization at one volcanic dome that shows the strongest evidence of demagnetization, Dome 3. First, we model the formation of Dome 3 as the intrusion of a laccolith to determine the likely depth and lateral extent of the laccolith material. We recognize that the actual geometry of the volcanic materials may be complex or even partially extrusive (see Section 3.7.4), but this model serves as a first-order test of the hypothesis that demagnetization has occurred. In this modeling step, we approximate the laccolith as having an elliptical footprint, which we subsequently refer to as the Elliptical Approximation. This approximation is in contrast to the Contour Approximation, which approximates Dome 3's footprint as the lowest

closed topography contour around the dome. Next, we model the flow of heat away from this laccolith to determine which regions around the laccolith reach temperatures high enough to demagnetize any magnetic source bodies. In this step, we approximate the footprint of the laccolith as a circle because of the 2D axisymmetric nature of our thermal modeling (subsequently referred to as the Circular Approximation).

Third, given the results of the heat flow model, we calculate what percentage of magnetization remains in the source bodies nearby the intrusion after being held at sub-Curie temperatures for thousands of years, considering several different possible magnetic minerals. Finally, we estimate the effect of demagnetization on the magnetic field and swirl pattern. To do this we create an arrangement of magnetic dipoles to represent the swirl source bodies before demagnetization by the laccolith. Then, we remove either 50% or 100% of the magnetic moments of the dipoles within the laccolith region to approximate the effects of partial or total demagnetization, respectively. Additionally, we infer the volume and geometry of the source bodies from these results to estimate the magnetization strength and age of the source bodies.

3.2 Data & georeferencing

In this work we use Lunar Reconnaissance Orbiter (LRO) Lunar Orbiter Laser Altimeter (LOLA) topography data at a resolution of 1024 pixels per degree, obtained from the Planetary Data System (PDS)(Smith et al., 2010)(Figures 3.1B, 3.1D, 3.1F, 3.2B, 3.3B, 3.3C, 3.4, 3.7, 3.9, 3.13, 3.15, and 3.16). Additionally, we use the β param-

eter, which is a combination of Clementine 750 nm and 950 nm reflectance maps that distinguishes swirl brightness patterns from the brightness changes associated with fresh crater ejecta (Hemingway et al., 2015). We use the β parameter at a resolution of 151 pixels per degree (Figures 3.1A, 3.1C, 3.1D, 3.1E, 3.1F, 3.2A, 3.2B, 3.3, 3.4, 3.15, 3.16, A.2D, and A.5). Lastly, we compare our modeled magnetic fields with the magnetic field observations from Tsunakawa et al. (2015) and Ravat et al. (2020) expanded out to degree 450 (Figures 3.13A, 3.13B).

Around Dome 3, the LOLA topography data and Clementine-derived β parameter data were aligned manually using small craters to the east of the swirl. The reflectance map was shifted 7 pixels ($\sim$1400 m) to the west and 2 pixels ($\sim$400 m) to the north relative to the topography map to correctly georeference the two datasets. We assume that we have shifted the maps to the best of our ability given their resolutions, which means that the maps can be assumed to be correctly aligned within one pixel. Thus, the estimated error between the two datasets is less than 200 m (the size of the β parameter map pixels).

3.3 Motivating observations from the Reiner Gamma swirl pattern

Reiner Gamma swirl is located in western Oceanus Procellarum (Figure 3.1A, 3.1B) and is often described as consisting of two segments. The first is the main body, which is a $\sim$30 km ellipse located at 301.0°E, 7.5°N. The second is the tail, a long and

sinuous pattern that extends ∼150 km northeast from the main body towards the Marius Hills, a large (∼35,000 km^2) volcanic complex (Head and Gifford, 1980; Whitford-Stark and Head, 1977) (Figure 3.1B). The volcanic domes and cones that make up the Marius Hills are typically 50-200 m in height (Head and Gifford, 1980) and are made up of blocky lava flows that represent a variety of eruption styles (Lawrence et al., 2013).

The ages of the domes within the Marius Hills are likely Eratosthenian or Imbrian, but are generally not well-constrained because the regions dated are not always well-defined (Heather and Dunkin, 2002; Heather et al., 2003; Hiesinger et al., 2003; Huang et al., 2011; Lawrence et al., 2013; McCauley, 1967; Whitford-Stark and Head, 1977; Wilhelms et al., 1987). The most careful study to date of Marius Hills dome ages was by Hiesinger et al. (2016), who dated 43 domes and 27 peripheral non-dome mare regions. For all 43 domes dated in Hiesinger et al. (2016), the age range was found to be 1.03-3.65 Ga, and for all 27 non-dome mare regions the age range was found to 1.20-3.69 Ga. The age ranges found in Hiesinger et al. (2016) are mostly consistent with previous work, with the exception of Huang et al. (2011). Hiesinger et al. (2016) found that in several locations, the domes are younger than their adjacent mare basalts. For our work in this area, we will focus on the ages of the domes rather than the ages of the basalts because it is the dome ages that determine when thermal demagnetization, and thus the low-field era of the dynamo, could have occurred. The seven dated domes closest to the Reiner Gamma tail have an age range of 1.3-3.3 Ga and hence in our work we assume that the oldest dome age relevant to thermal demagnetization of Reiner Gamma is ∼3.3 Ga.

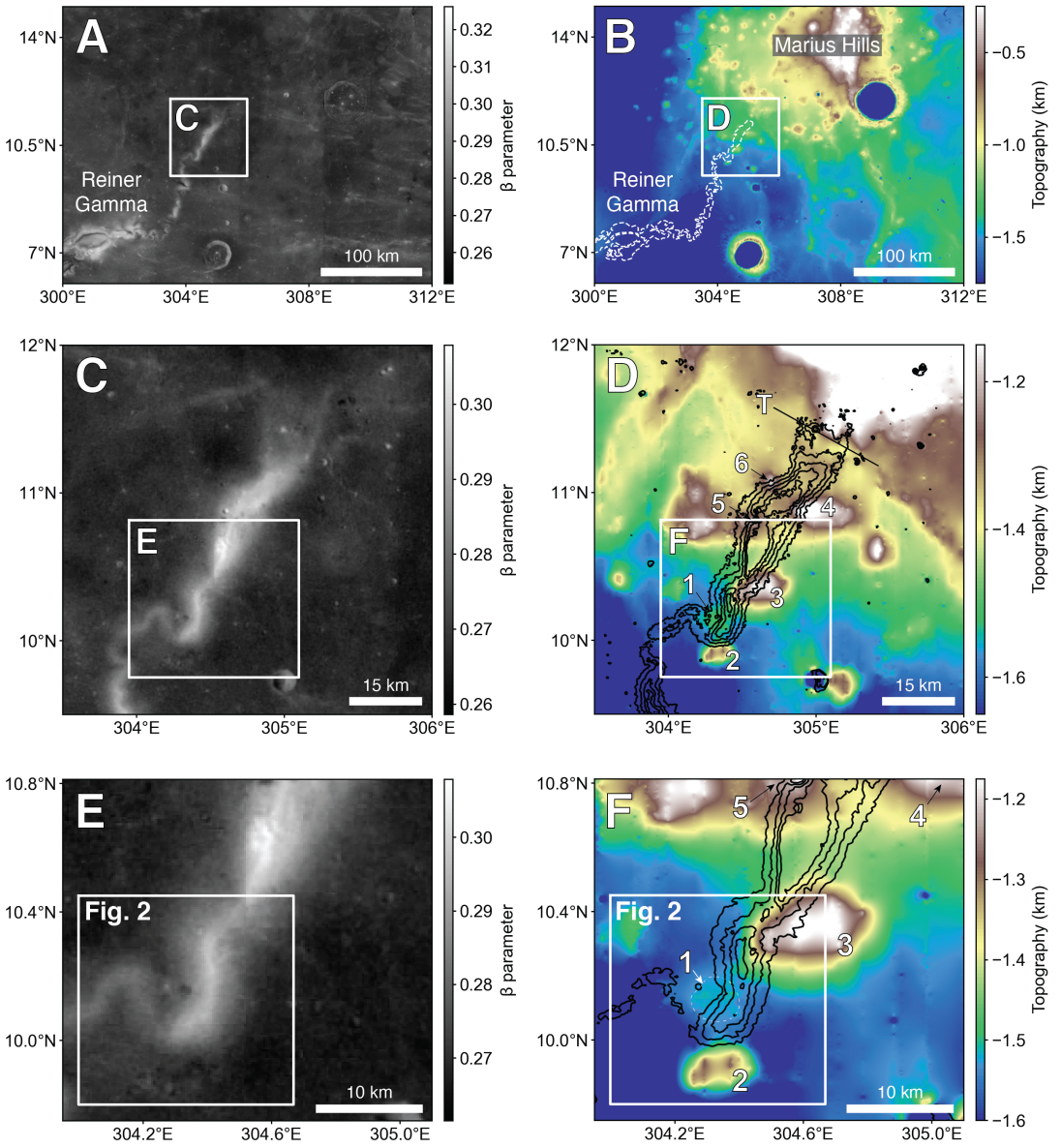

Figure 3.1: (A) β parameter map of the Reiner Gamma and Marius Hills region. The β parameter emphasizes lunar swirls (Hemingway et al., 2015). (B) Lunar Orbiter Laser Altimeter (LOLA) (Smith et al., 2010) topographic map of the same window as Panel A, with the Marius Hills volcanic complex indicated. (C) β parameter map of the box indicated in Panel A around the end of Reiner Gamma's tail. (D) Topographic map of the same window as Panel C. Contours of the β parameter map at levels 0.275, 0.28, 0.285, 0.29, and 0.295 (increasing towards the center of the swirl) are shown with solid black lines. Domes of interest are labeled with numbers 1 through 6, and the termination of the swirl at a topographic slope boundary is indicated with label T. (E) β parameter map of the box indicated in Panel C. This area is the focus of this work. The north-south artefact along the western edge of the swirl extending between ~10.4°N and ~10.7°N is addressed in Section 3.3 and Figures A.2 and A.3. (F) Topographic map of the same window as panel E. Contours of the β parameter map at levels 0.28, 0.285, 0.29, 0.295 (increasing towards the center of the swirl) are shown with solid black lines. Domes of interest are labeled with numbers 1 through 4, and Dome 1 is qualitatively circled with a dashed white line for clarity.

In this work we focus on the northern half of Reiner Gamma's tail (Figure 3.1B, 3.1D). In this area, the swirl generally does not cross over the peaks of the domes, but rather snakes around them (Figure 3.1D, 3.1F). We interpret this albedo-topography relationship as being caused by thermal demagnetization: the heat from dome formation erased or partially erased the pre-existing magnetization of the source bodies responsible for the creation of the swirl. Lunar swirls form over millions of years (Hemingway et al., 2015; McFadden et al., 2019), while volcanism in this area likely occurred more than one billion years ago (Heather and Dunkin, 2002; Heather et al., 2003; Hiesinger et al., 2003, 2016; Lawrence et al., 2013; McCauley, 1967; Whitford-Stark and Head, 1977; Wilhelms et al., 1987). Thus, any magnetic source bodies remaining after demagnetization have had sufficient time to control the surface albedo. Additionally, any downslope movement of soil on the flanks of a dome would only overturn, freshen, and brighten the regolith, not darken it as observed.

We can trace the swirl from the southwest to the northeast to illustrate how it passes near six different volcanic domes without passing over their peaks. First, the swirl almost surrounds Dome 1 without passing over its peak (Figure 3.1F, Figure 3.2B). Then, the southern edge of the swirl coincides with the north flank of Dome 2 (Figure 3.1F, Figure 3.2B, and Figure 3.3B, label X), but does not pass over the peak of Dome 2. Further to the northeast, the swirl wraps around the west and northwest flanks of Dome 3 (Figure 3.1F, Figure 3.2B, Figure 3.3B). In Figure 3.3, the outline of the swirl is defined by the contour line at $\beta = 0.28$. This is the lowest contour value that broadly encloses features of interest across the entire region.

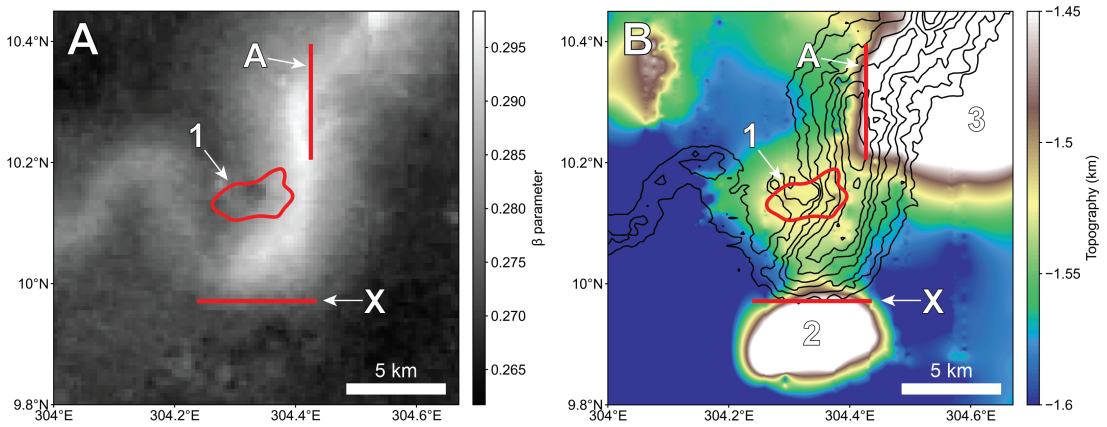

Figure 3.2: (A) β parameter map showing the swirl making a sharp turn around Dome 1, with Features A and X (straight red lines) indicated. The solid red contour line indicates the boundary of Dome 1, found by taking the lowest closed contour around its peak. (B) Topographic map of the same window as Panel A, with β parameter contours overlain in black. The β parameter contour lines are at 0.2778, 0.2807, 0.2836, 0.2864, 0.2893, 0.2921, and 0.2950, increasing towards the center of the swirl. The topography color scale has been saturated to more clearly show the swirl wrapping around Dome 1 (solid red contour line). Domes 2 and 3 are also indicated. Feature X (horizontal straight red line): the southernmost part of the swirl in this area has an east-west strike that parallels the north flank of Dome 2. Feature A (vertical straight red line): the strike of the swirl in this area parallels the western flank of Dome 3. This feature is also indicated in Figure 3.4.

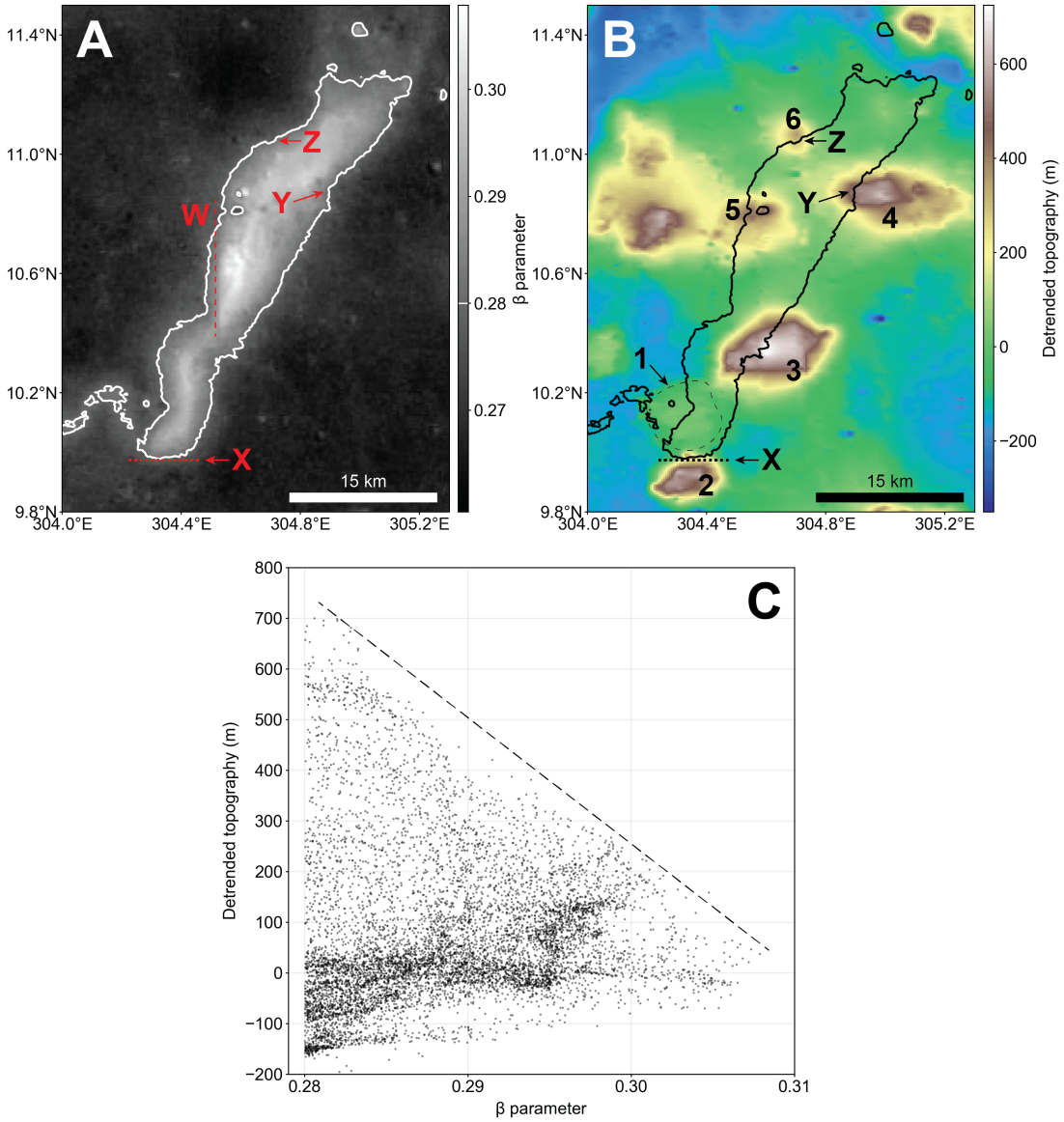

Figure 3.3: Comparison between β parameter and topography maps. (A) β parameter map of the northernmost part of the tail of Reiner Gamma. The white contour line indicates a β value of 0.28. Features W, X, Y, and Z are indicated in red. (B) Detrended LOLA topographic map of the northernmost part of the tail of Reiner Gamma. The black contour line is the same as the contour line in Panel A. Domes 1-6 and Features X, Y, and Z are indicated. (C) Scatter plot comparing all map points inside the white and black contour lines in Panels A and B, respectively. The dashed black line indicates a qualitative trend: in general, as β parameter increases, altitude decreases. This corresponds to the swirl not coinciding with the areas of highest topography (the domes).

Continuing to the northeast, there is a broad notch in the eastern edge of the swirl (Figure 3.3A and 3.3B, label Y) as it passes Dome 4 . To the west, the bright central region of the swirl avoids the peak of Dome 5 (Figure 3.1F, Figure 3.3B). Another smaller and more speculative notch is located in the edge of the swirl (Figure 3.3A and 3.3B, label Z) as it passes Dome 6. Finally, the swirl terminates, at a larger, more plateau-like region of the Marius Hills (Figure 3.1D, label T and black line).

To help quantify if the swirl's pattern is indeed anti-correlated with the locations of the domes, we plot swirl brightness as a function of topography (Figure 3.3C). Swirl brightness is represented by the swirl spectral parameter β (see Section 3.2, (Hemingway et al., 2015)). The topography map was detrended by finding a linear fit to local topography and subtracting this fit to remove the background upwards slope towards the Marius Hills. The higher-resolution topography map was downsampled to match the resolution of the β parameter map. In this correlation study, only pixels inside the swirl are included in Figure 3.3C, i.e., pixels inside the contour line of $\beta = 0.28$ in Figures 3.3A and 3.3B. A boundary can be seen in Figure 3.3C (black dashed line): brighter pixels (higher β parameter value) generally have lower topography, and vice versa. The upper right quadrant of Figure 3.3C, representing regions that would be both bright (high β parameter) and high topography, is devoid of points. This relationship implies that the swirl does not coincide with the areas of highest topography (the domes).

An apparent north-south linear feature in the swirl brightness E (Figure 3.3A, also visible in Figure 3.1C), hereafter referred to as Feature W, is likely an artifact from the mosaicking of imagery tiles. To show this, we compared the β parameter derived from

Clementine reflectance maps with β parameter derived from Kaguya Multiband Imager (MI) reflectance maps (Figures A.2 and A.3). Interestingly, a vertical band can also be seen in the Kaguya β parameter map (Figure A.2C, white arrows). The edge of this band appears to coincide with Feature W in the Clementine β parameter map (Figure A.2D, white arrows). Because Feature W's perfectly north-south strike in both Kaguya and Clementine β parameter maps is obviously an artefact due to tiling, we assume that it is a coincidence that both maps contain spurious Feature W. Most importantly, this region of the swirl is not critical for our analysis, and we use other well-defined reflectance boundaries to make our conclusions.

Having demonstrated that, in general, the brightest regions of the swirl are anti-correlated with the domes, the remainder of this work focuses on the swirl's correlation with Dome 3 (Figure 3.4). Consideration of the potential thermal demagnetization around other domes is left to future work. The solid yellow contour line in Figure 3.4 is the lowest closed topography contour around Dome 3 (-1420 meters), hereafter referred to as the Contour Approximation for the dome's extent. Along the western and northwestern flanks of Dome 3, which are collocated with the edges of the swirl, we define three albedo features that we propose are due to thermal demagnetization from Dome 3. First, the strike of the swirl is parallel to the strike of the western flank of Dome 3 (Figure 3.4, line A). Second, a local minimum in swirl brightness along its path is collocated with the northwestern edge of Dome 3 (Figure 3.4, box B). This brightness minimum is not as dark as the background values, i.e., the swirl is not completely severed at this point. Third, the strike of a bright region of the swirl is parallel to the

northwestern flank of Dome 3 (Figure 3.4, line C). These features will be referred to as Feature A, Feature B, and Feature C in subsequent sections, respectively.

3.4 Conceptual framework for the timing of dome and swirl formation

Modeling the thermal demagnetization of Dome 3 requires accounting for its formation mechanism. We focus on modeling Dome 3 as an intrusive magma body rather than extrusive volcanism (Figure 3.5D). This is justified by three points: 1) The heat from the flood basalts covering all of Reiner Gamma swirl was insufficient to thermally demagnetize all of the magnetic source bodies (i.e., we can still see the swirl today), likely due to the eruption volumes and timescales being too small. It is also unclear if extrusive volcanism from a shield volcano would be able to provide the requisite volumes and timescales. In contrast, intrusive volcanism can provide a potentially larger and longer-lived heat source. 2) If the source bodies are buried within the local 3-4 km-thick mare basalts (Garrick-Bethell and Kelley (2019); Kelley and Garrick-Bethell (2020); and this work), their thermal demagnetization by a volcano would require the special coincidence of erupting the volcanic lava right at the time when the yet-to-be-buried magnetic source bodies were on the surface and susceptible to being heated by this lava. In other words, the magnetic source bodies would have to be coeval with all six of the volcanic domes at Reiner Gamma tail. In contrast, magma intruding into the subsurface at any time after source body emplacement and burial might preferentially flow along the

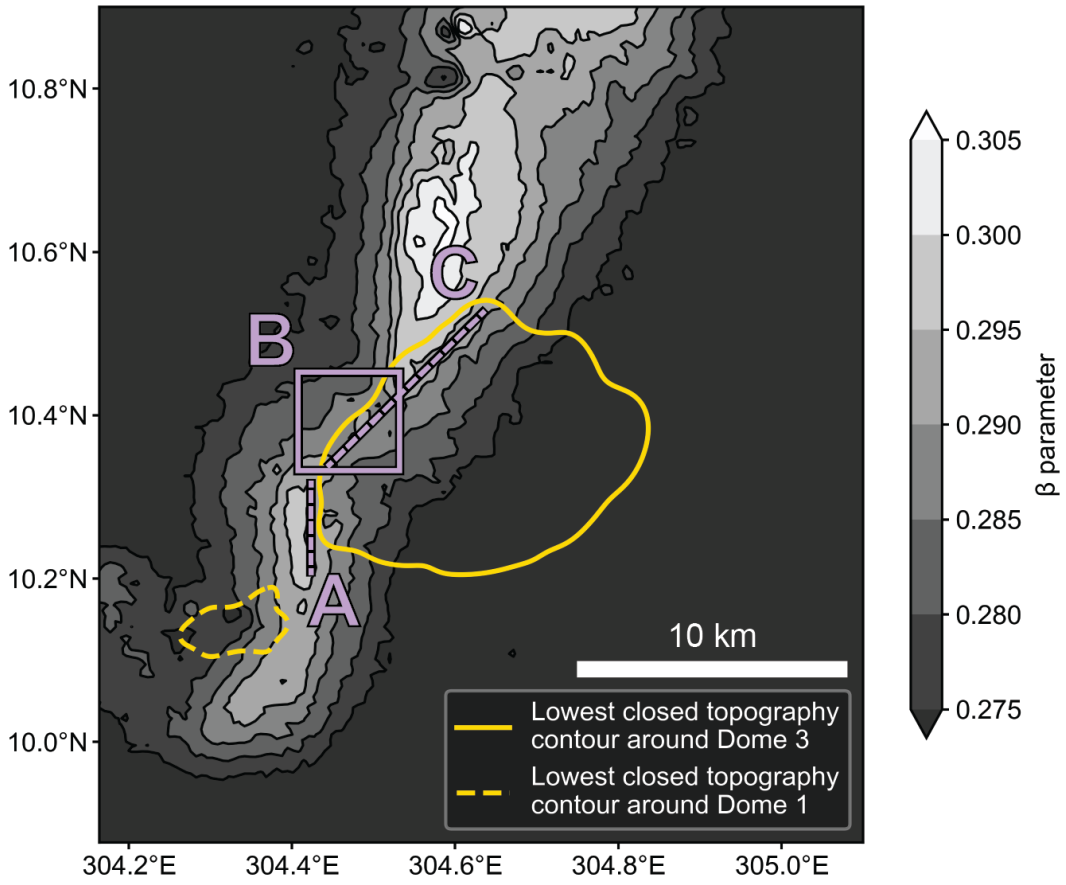

Figure 3.4: Map showing a closer view of the relationship between the boundary of Dome 1, Dome 3, and the swirl. The grayscale background map is the β parameter, the solid yellow contour line indicates the Contour Approximation boundary of Dome 3 (the lowest closed topographic contour around the dome at -1420 meters), and the dashed yellow contour line indicates the lowest closed topographic contour around Dome 1 (-1524 meters). The vertical purple dashed line labeled A indicates Feature A: a parallel strike between the western edge of Dome 3 and a bright region of the swirl. The purple box labeled B indicates Feature B: a local minimum in swirl brightness at the edge of Dome 3, and the slanted purple dashed line labeled C indicates Feature C: a parallel strike between the northern edge of Dome 3 and a bright region of the swirl.

paleo-surface where the bodies were emplaced, since it will act as a décollement layer. Hence, an intrusive magma source helps remove the coeval requirement (Figure 3.5). 3) Finally, we will show later that the topography profile of the dome resembles the profile of an ideal laccolith, particularly in the north-south direction.

A sample timeline (Figure 3.5) shows three potential dome formation scenarios that allow for either intrusive or extrusive volcanism. At Time 1 (Figure 3.5A), we assume that the swirl magnetic source bodies begin on or near the surface of the basalts and are located on a paleosol that accumulates as the surface is exposed to space. Our modeling results (see Section 3.6.1) suggest that the source bodies can be located anywhere within the top ∼2 km of basalt. After some time, the whole area can either be buried in more flood basalt (Figure 3.5B) or an extrusive event creates a dome that covers the magnetic source bodies (Figure 3.5C). At Time 3, after the burial by basalts at Time 2, a laccolith (Pollard and Johnson, 1973) spreads laterally using the paleosol layer collocated with the magnetic source bodies as a décollement surface, potentially pushing some source bodies upwards and others downwards (Figure 3.5D, dark purple ellipses). Alternatively at Time 3, the laccolith could spread laterally on a layer that is not collocated with the depth of the magnetic source bodies (Figure 3.5D, faded purple ellipses), resulting in the magnetic source bodies being located somewhat away from the laccolith. In both cases, the magnetic source bodies are near enough to the laccolith to experience some degree of thermal demagnetization.

Weitz and Head (1999) found that the Marius Hills domes have a large extrusive component. However, mixed intrusive/extrusive volcanism has been observed in other

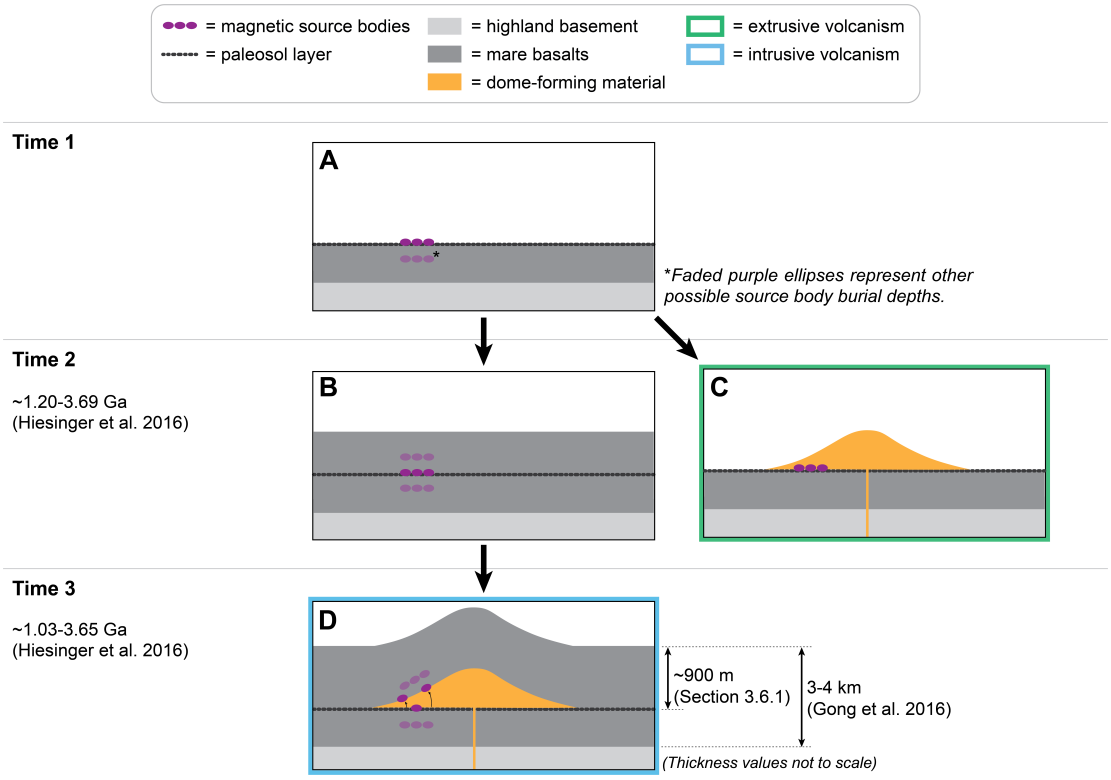

Figure 3.5: Diagram depicting potential formation scenarios for a dome located near magnetic source bodies. (A) In our favored model, at Time 1 the magnetic source bodies are located on the ancient surface. A paleosol layer will have formed on this surface that can serve as a décollement layer for the intruding magma after flood basalts bury the source bodies (black dashed line). In our proposed model, the magnetic source bodies can be anywhere within the top ∼1.5 km of the mare basalts (see Section 3.6.1). (B) At Time 2, the entire area has been buried by flood basalt. (C) As an alternate scenario at Time 2, an extrusive dome has formed and covered the magnetic source bodies, although this scenario is less favored since it suggests coeval emplacement of the magnetic source bodies and all six volcanic domes. (D) At Time 3, after the burial of the source bodies by basalts in (B), a laccolith forms, spreading laterally along a décollement surface associated with the paleosol layer that is collocated with the magnetic source bodies (dark purple ellipses). Alternatively, the laccolith could also propagate laterally on layers above or below the magnetic source bodies (faded purple ellipses). In (D) the degree of thermal demagnetization is a function of the proximity of the source bodies to the magma.

locations on the lunar nearside, including the Aristarchus Plateau and the Rümker Hills (Huang et al., 2014), and lunar laccoliths have been observed to occur in regions of otherwise extrusive volcanism (Wöhler and Lena, 2009). Most of the conclusions that we reach from modeling Dome 3 as intrusive can be applied to the case that Dome 3 is extrusive, albeit the extrusive scenario requires a more unique set of circumstances (see above and Section 3.7.4). For now, until further work can be completed, the intrusive magma body can serve as a starting point for understanding thermal demagnetization of Reiner Gamma.

Our model does not specify exactly how the magnetic source bodies were emplaced, but we favor the hypothesis that they are meteoritic material. This is consistent with the proposal of Garrick-Bethell and Kelley (2019) for Reiner Gamma and with other strong magnetic anomalies (Wakita et al., 2021; Wieczorek et al., 2012). These hypotheses are consistent with the very low magnetic susceptibility (approximately 1.58×10^{-3} (SI units)) of endogenous lunar materials (Wieczorek et al., 2012), which implies they could not likely produce the magnetic fields observed from orbit unless they were magnetized in unrealistic strength dynamo fields.

3.5 Methods

3.5.1 Elastic flexure modeling of Dome 3 formation

The putative laccolith at Dome 3 possesses an approximately elliptical footprint which can be modeled by an elastic plate whose vertical deformation w is (Pollard and

Johnson, 1973):

$$w(x,y) = \frac{p_d}{8D} \frac{\left(1 - \frac{x^2}{a^2} - \frac{y^2}{c^2}\right)^2}{\frac{3}{a^4} + \frac{3}{c^4} + \frac{2}{a^2 c^2}} \tag{3.1}$$

where p_d is magma driving pressure, D is the flexural rigidity ($D = Eh^3/12(1-\nu^2)$, E is Young's modulus, h is the thickness of the overburden layer, and $\nu = 0.25$ is Poisson's ratio), and a and c are the semi-minor and semi-major axes of the laccolith's elliptical footprint (Figure 3.6).

Approximating Dome 3's footprint as an ellipse will be referred to as the Elliptical Approximation of the dome boundary. The semi-major axis c and semi-minor axis a of the Elliptical Approximation were set equal to the distance between breaks in slope between the dome's flank and the background plains, along the dome's short and long axes (Figure 3.6; $c = 8$ km, and $a = 7$ km). For p_d, we assume a range of values: 3-15 MPa. The low end p_d was chosen based on the 3-8 MPa magma pressure estimate given by Wöhler and Lena (2009), a study of potentially intrusive lunar domes. The high end of p_d was chosen to be a bit higher than the 9 MPa magma driving pressure inferred by Wichman and Schultz (1996), a study of an intrusive body within the lunar crater Taruntius. The range of elastic moduli for in-situ rock that we consider is 5-30 GPa, which was chosen to include all likely values based on Dinçer et al. (2004) and Rubin and Pollard (1987), which consider laboratory results on terrestrial basalts (Dinçer et al., 2004) and theory based on dikes located near Kilauea, Hawai'i and Krafla Volcano, Iceland (Rubin and Pollard, 1987). For each combination of p_d and E in the ranges given above, we calculated the resulting overburden thickness h using Equation

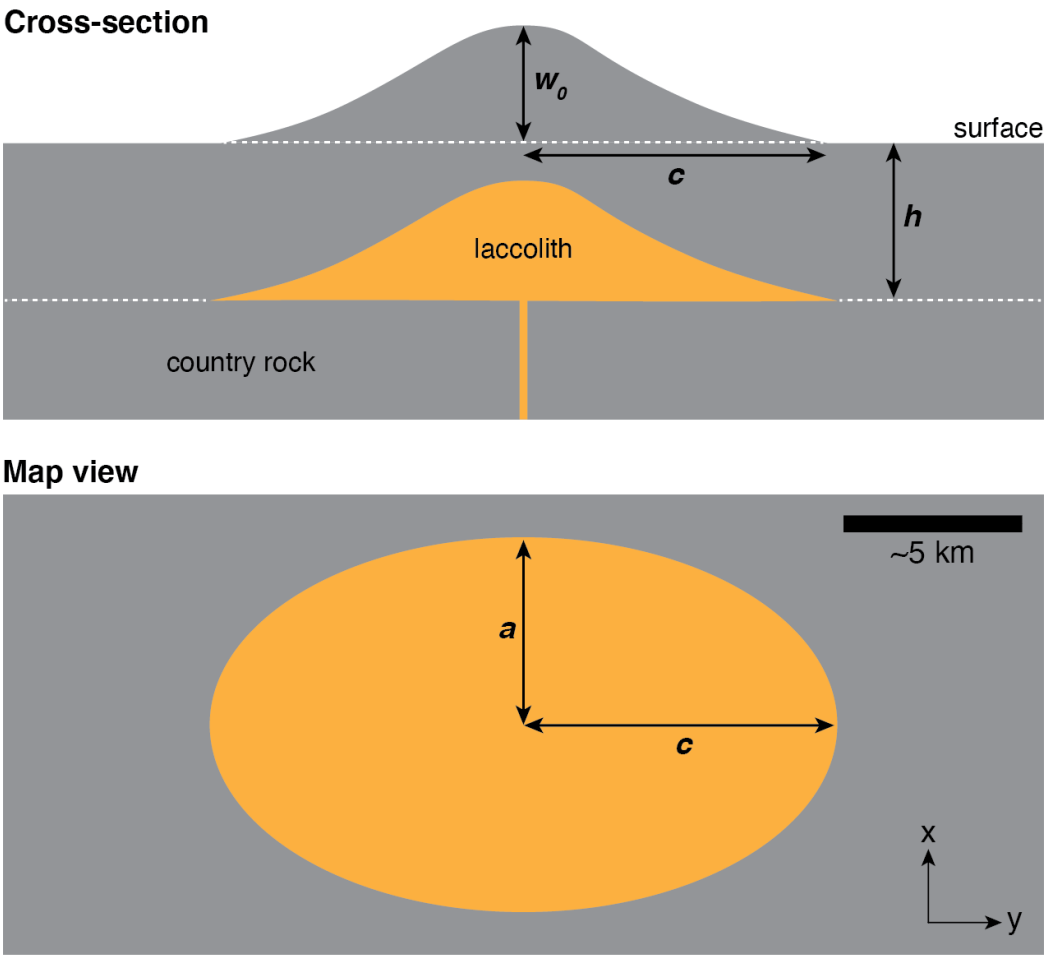

Figure 3.6: Cartoon depicting the parameters used in modeling the buried laccolith. H is the thickness of the overburden burying the laccolith, $w(0,0) = w_0$ is the maximum vertical displacement of the surface due to the intrusion, and a and c are the semi-minor and semi-major axes of the laccolith's elliptical footprint, respectively.

3.1 (Figure 3.8).

For our nominal model, we use $p_d = 7$ MPa, which represents the approximate middle of the total magma driving pressure range between Wöhler and Lena (2009) and Wichman and Schultz (1996). And we use $E = 16$ GPa, which represents the average elastic modulus of the basalt samples analyzed in Dinçer et al. (2004). These values are chosen to represent a middle value in each of the parameter ranges. These particular p_d and E values are indicated with dashed white lines and a gray point in Figure 3.8.

To assess if the Elliptical Approximation adequately captures the dome's shape, we compare it with the locations of breaks in slope around the dome and the more detailed Contour Approximation. Slope break choices from two sample topography profiles can be seen in Figures 3.9B and 3.9C; these boundaries represent the greatest topographic extent of Dome 3. The Elliptical Approximation and slope boundaries are in approximate agreement along the northwest flank of the dome (the area of focus in this paper, as the swirl passes this location, Figure 3.9A). In contrast, the Contour Approximation is about 20% smaller in radial extent along the northwest flank. Hence, our Contour Approximation is slightly conservatively small relative to the maximum extent of the magma bodies that formed the dome as inferred from the slope breaks.

3.5.2 Heat flow modeling around Dome 3

The purpose of our thermal model of the laccolith is to determine which areas around the intrusion reach temperatures high enough (and for a long enough duration) to achieve any degree of demagnetization. To model the flow of heat away from the

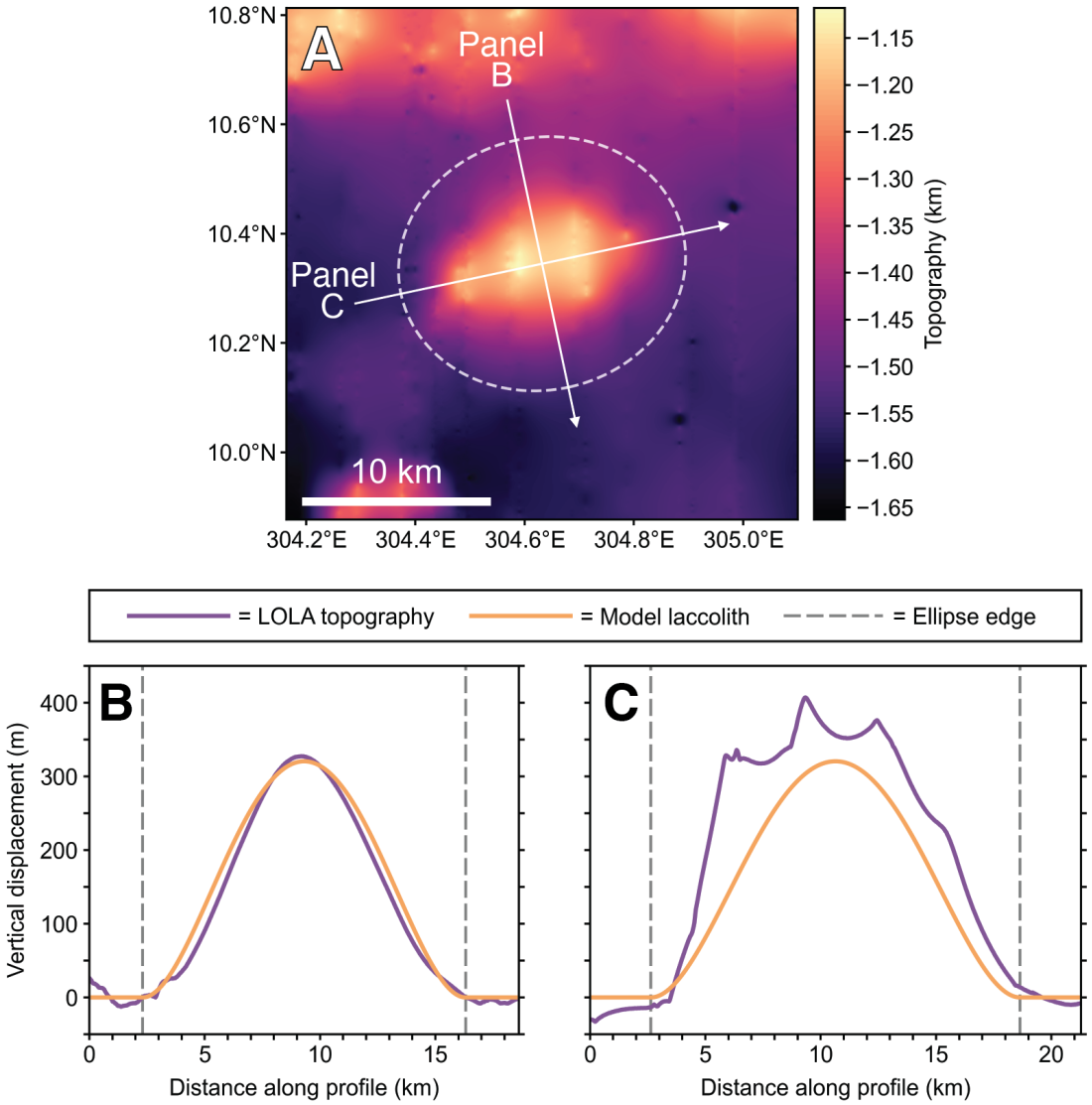

Figure 3.7: (A) The Elliptical Approximation of the Dome 3 footprint (white dashed line) compared with topography. Transects B and C in Panel A correspond to topographic profiles in purple in Panels B and C. (B&C) Model of topographic deformation (Equation 3.1, orange lines) compared with observed topography transects B and C (purple lines). The vertical gray dashed lines represent the edges of the Elliptical Approximation.

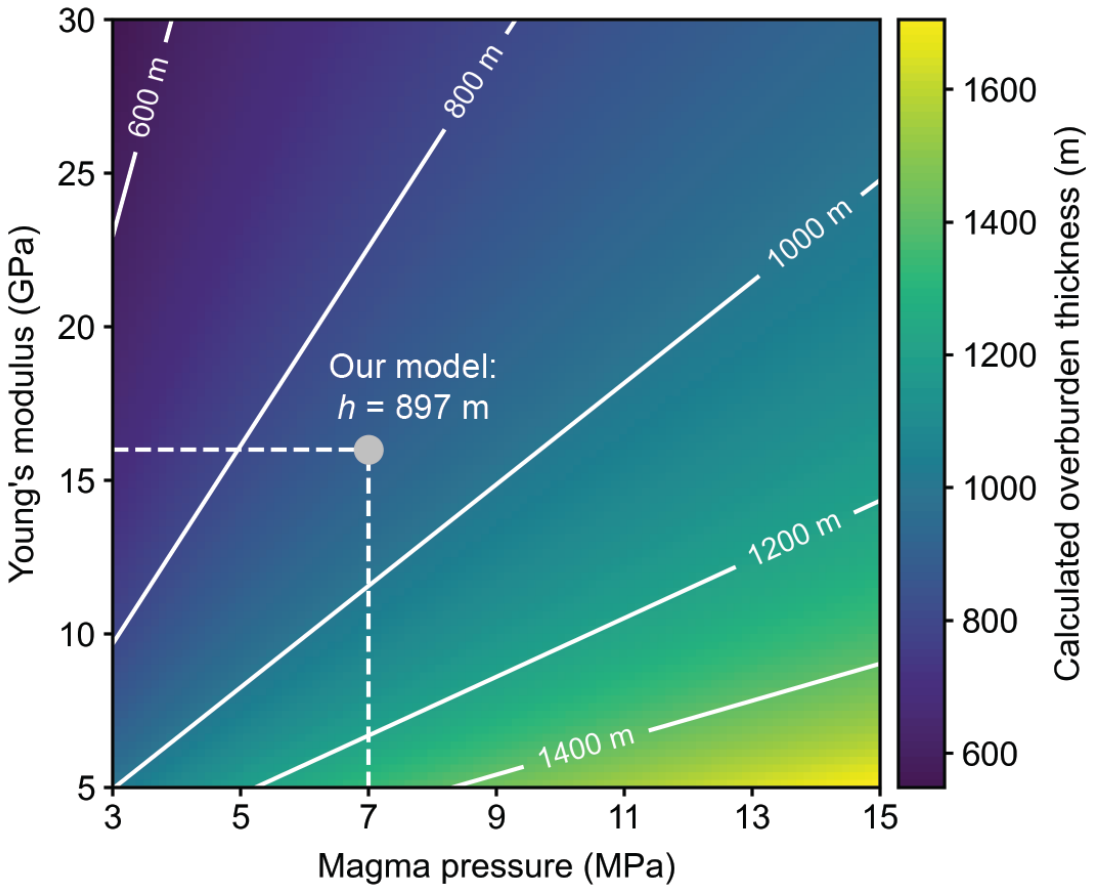

Figure 3.8: Plot showing the overburden thickness h at Dome 3 for plausible combinations of Young's modulus E and magma driving pressure p_d that produce the observed topographic deformation (325 m), via Equation 3.1. The minimum and maximum h values are 549 and 1705 m, respectively. For our nominal model with $E = 16$ GPa and $p_d = 7$ MPa, $h = 897$ m (gray point).

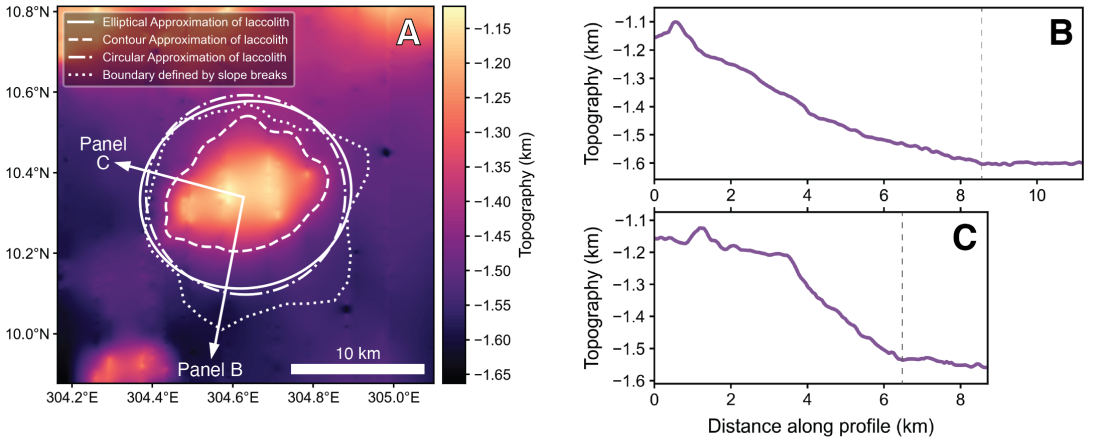

Figure 3.9: A comparison of different Dome 3 boundaries. The Contour Approximation represents most of Dome 3's volume and its shape; the Elliptical Approximation and the slope break boundary represent its outermost extent. (A) Map showing the Elliptical Approximation (solid line), the -1420 m LOLA topography contour (dashed line; Contour Approximation), the Circular Approximation (see Section 3.5.2, dot-dash line), and the boundary as defined by slope breaks (dotted line). The slope break boundary (dotted line) is the circumferential three-point running average of 36 measured slope breaks. (B) Example topography transect along profile B. The black dashed line indicates our choice of slope break. On the smoother slopes to the south of the dome, choosing the location of the slope break is relatively ambiguous. (C) Example topography transect along profile C. The black dashed line indicates our choice of slope break. On the steeper northwestern side of the dome, choosing the slope break is clearer than with other sections of the dome.

laccolith, we created a two-dimensional axisymmetric model where the axis of rotation runs vertically through the center of the model laccolith, the radial coordinate r runs perpendicularly outwards from this axis, and the vertical coordinate z runs parallel to this axis. The space is divided up into cells with radial resolution Δr, vertical resolution Δz, and temperature T. Heat flows through these cells according to the finite-difference version of the diffusion equation:

$$T_{i,j}^{m+1} = T_{i,j}^{m} + \kappa \Delta t \left[\frac{1}{r} \frac{T_{i+1,j}^{m} - T_{i-1,j}^{m}}{2\Delta r} + \frac{T_{i-1,j}^{m} - 2T_{i,j}^{m} + T_{i+1,j}^{m}}{(\Delta r)^2} + \frac{T_{i,j-1}^{m} - 2T_{i,j}^{m} + T_{i,j+1}^{m}}{(\Delta z)^2} \right] \tag{3.2}$$

where T is the temperature of the cell; m, i and j are the time, r direction, and z direction indices, respectively; κ is the thermal diffusivity; Δt is the time step; r is the radial distance; and Δr and Δz are the spatial resolutions in r and z, respectively. The derivation of Equation 3.2 can be found in Appendix A.1. The radial derivative of the temperatures of cells along the axis (the left-hand edge of Figure 3.10) is zero (a Neumann boundary condition), and cells along the remaining three sides of our model space are held constant (a Dirichlet boundary condition).

Due to this model's rotational symmetry, the laccolith in this model necessarily cannot have an elliptical footprint as in the Elliptical Approximation. Rather, in this model space the laccolith must have a circular footprint, hereafter referred to as the Circular Approximation (Figure 3.9A). We chose its radius to be $b = 7.5$ km, which is the average of the semi-major and semi-minor axes. Additionally, we set the central thickness of the laccolith to 332 m (the actual height of the dome as measured

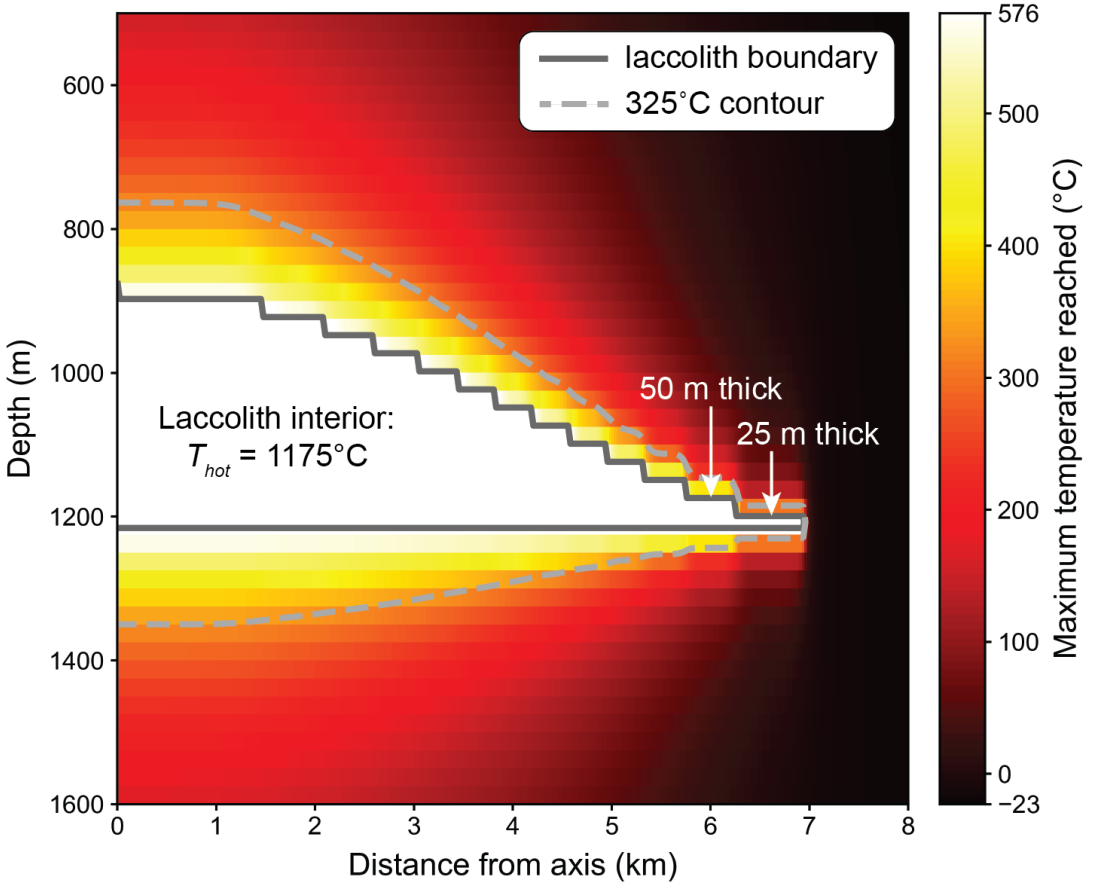

Figure 3.10: Maximum temperatures reached by the 2D-axisymmetric model laccolith of Dome 3 after maximum temperatures have been reached. The vertical and horizontal scales are not the same. The "zigzag" edge of the laccolith is due to the resolution of the thermal model (25 meters/pixel) being exaggerated by the vertical scaling. The left-hand vertical axis represents the axis of rotational symmetry. The white arrows indicate where the laccolith is 50 m and 25 m thick at its edge (2 thermal model cells and 1 thermal model cell, respectively). The dark gray line indicates the boundary of the laccolith, and the dashed light gray line indicates the 325°C contour line.

from topography), and the central burial depth of the laccolith to 897 m (the estimated overburden thickness, see Sections 3.5.1 and 3.6.1). The variation of thickness of the laccolith with radius in this thermal model is determined by the circular-footprint version of Equation 3.1:

$$w(r) = \frac{p_d}{64D}(b^4 - 2b^2r^2 + r^4) \tag{3.3}$$

where r is the radial coordinate, b is the circular laccolith radius, and h is the thickness of the overburden layer (the values of E and p_d are as specified in the previous section). For simplicity in the thermal model's boundaries we assume that the surface is undeformed by this laccolith (i.e., it is flat).

We define T_{hot} as the initial temperature of the intrusion in our model, and set it to be 1175°C. Additionally, we define T_{cool} to be the temperature of the surrounding country rock before the heat from the intrusion begins to propagate, and set it to be -23°C. T_{hot} was chosen to be just below the liquidus of basalt, and T_{cool} was chosen to be the lunar mean near-surface temperature. We take the liquidus and solidus of basalt to be 1200°C and 1000°C, respectively (McBirney, 1993). The thermal conductivity, density, and specific heat capacity of basalt were set as $k = 1.5$ W/(m·K), $\rho = 3000$ kg/m^3, and $c = 10^3$ J/(kg·K), respectively (Garrick-Bethell and Weiss, 2010). These values produce a thermal diffusivity of $\kappa = 5 \times 10^{-7}$ m^2/s ($\kappa = k/(\rho \cdot c)$). The latent heat of basalt is 10^5 J/kg (Barboza and Bergantz, 1996), which we convert to a total change in temperature due to the release of latent heat via the relationship $\Delta T = Q/(m \cdot c)$, where ΔT is the change in temperature, Q is energy due to heat, m is mass, and c is specific heat capacity. For a specific heat capacity of 10^3 J/(kg·K), ΔT is 100°C. This

change in temperature was spread linearly between the liquidus (1200°C) and solidus (1000°C) of basalt, i.e., for every degree of temperature decrease (in °C) between the liquidus to the solidus, 0.5°C was added to the temperature of the cell to represent the release of latent heat. For our model that cooled from $T_{\text{hot}} = 1175$°C to temperatures below the solidus, a total of (1175°C – 1000°C)(0.5°C/°C) = 87.5°C was added to each cell as the release of latent heat.

The ancient background thermal gradient can be approximated using $dT/dz = q/k$, where dT/dz is the thermal gradient, q is the heat flux, and k is thermal conductivity. Laneuville et al. (2013) find a range of paleo lunar heat fluxes of 20-55 mW/m^2 at 3.75 Ga, while Garrick-Bethell and Weiss (2010) find a paleo lunar heat flux of ∼30 mW/m^2 at ∼4.4 Ga. If we use the highest value, 55 mW/m^2, and the thermal conductivity listed above, 1.5 W/(m·K), we obtain a thermal gradient of ∼37 K/km. At the maximum depth of our thermal modeling space (2 km), the thermal gradient would increase the temperature by 73 K. Because 73 K is a fairly modest change overall, we do not include it in our model. More importantly, the reduction of magnetization with depth, which takes place uniformly over both the magnetized and demagnetized regions, is not as important in our analysis as the effect magnetization differences across the laccolith and surrounding terrain. In other words, the lateral changes in magnetization are the ones that manifest as changes in the swirl pattern.

The time step was set to be the maximum stable time step as determined by the

spatial resolution of the model:

$$\Delta t = \frac{1}{2\kappa} \frac{(\Delta r \Delta z)^2}{(\Delta r)^2 + (\Delta z)^2} \tag{3.4}$$

where κ is the thermal diffusivity (5×10^{-7} m^2/s) and Δr and Δz are the resolutions in the radial and vertical directions, respectively (25 m). For the values given above, the resulting maximum stable time step is 9.9 years, and the model was run to a time sufficient to reach the state where the laccolith has solidified and all cells in the domain reached their maximum temperatures (total run time was 50,000 years).

3.5.3 Thermal demagnetization

Areas around the laccolith that do not reach the Curie temperature may experience partial demagnetization due to the rock surrounding the laccolith spending up to ∼10 kyr at elevated, but sub-Curie, temperatures. For example, the top-most faded purple magnetic source bodies in Figure 3.5D are not in direct contact with the laccolith, but are near enough to it to be heated during its emplacement.

To model the partial demagnetization process, we divided the cells around the laccolith into four envelopes that correspond to four different maximum temperature ranges (Figure 3.11, colored regions). These envelopes contain cells that experienced maximum temperatures within ranges of 200°C through 500°C, in increments of 100°C, and 500°C to 576°C (the model reached temperatures higher than 500°C, but no cells outside the magma body exceeded 576°C for any amount of time). Additionally, we divided the laccolith into three radially-spaced regions, each with a width equal to

one-third of the laccolith's radius yielding a total of twenty-four regions in which we calculate partial thermal demagnetization (Figure 3.11, black stars/circles centered in each region).

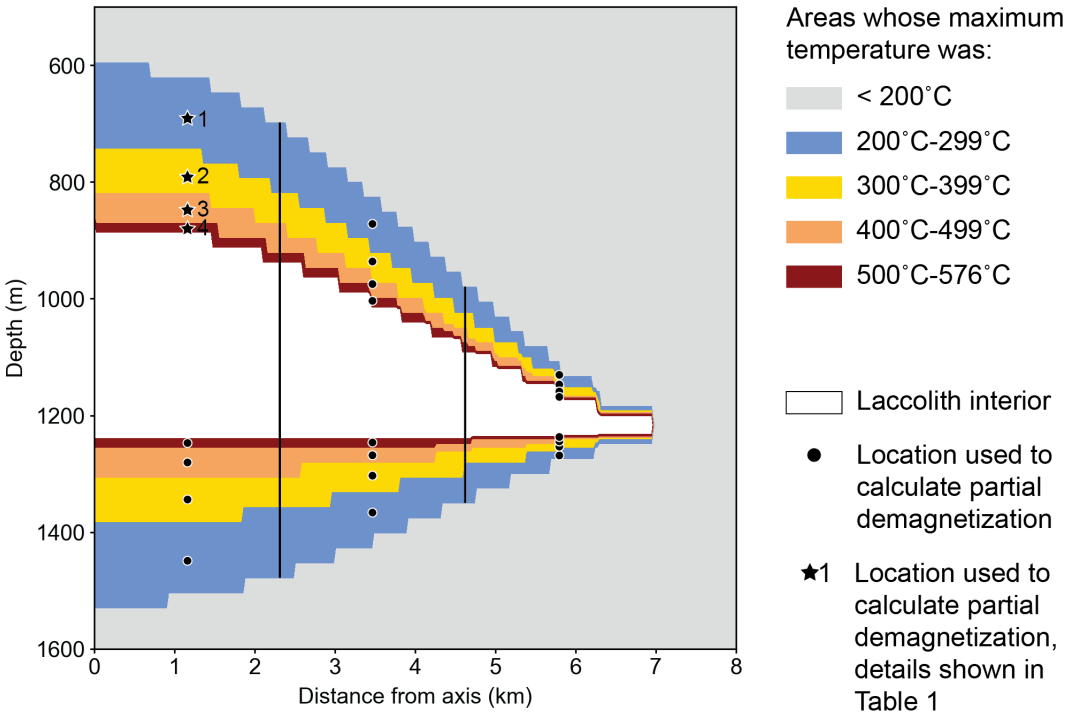

Figure 3.11: Cross-sectional map showing four bins of maximum temperatures reached by the 2D-axisymmetric model laccolith of Dome 3. The vertical black lines indicate the division of the laccolith's radius into thirds, and the black markers indicate locations whose temperature and time history were used with a Pullaiah diagram (Figure A.4) and a TRM curve (Figure 3.12) to determine amount of magnetization lost. The stars indicate locations whose time/temperature values are shown in Table 3.1.

Next, to calculate the fraction of remanence remaining at each of the twenty-four points in Figure 3.11, we used a Pullaiah diagram (Pullaiah et al., 1975) (Figure A.4). A Pullaiah diagram illustrates the relationship between heating a magnetic rock for

short times at high temperatures (i.e., in a laboratory) vs. long times at intermediate temperatures (i.e., in a planet's subsurface). More specifically, it relates the relaxation time and blocking temperature for families of similar magnetic grains. In our case, we know the long-time-scale heating history of the rock, and we use the Pullaiah diagram to derive the equivalent short-time-scale heating at high temperature. We compare that short-time-scale heating to actual laboratory-measured thermal demagnetization curves (thermoremanent magnetization (TRM) curves), Figure 3.12, to determine how much magnetization remains upon heating to that time-temperature history on the Moon. This remaining magnetization is then assumed to represent the remaining magnetization at Dome 3. In our analysis, we assume the laboratory heating timescale is 1000 seconds, which is has the standard laboratory heating timescale., Because the time axis in a Pullaiah diagram (Figure A.4) has a logarithmic scale, small variations in the actual laboratory heating timescales do not affect the temperature ranges that we take from the Pullaiah diagram.

As an example, if a cell in our thermal model that contains the carrier kamacite spent 1000 years at 500°C, we can find the laboratory equivalent to be ∼620°C of heating (at 1000 seconds) via the Pullaiah diagram for kamacite (Garrick-Bethell and Weiss, 2010) (see Figure A.4C). Then, referring to a laboratory TRM curve for kamacite, using, for example, Suavet et al. (2014) (Figure 3.12, orange circles), we see that at ∼620°C, the magnetic anomaly has lost ∼15% of its magnetization. If we use the alternative TRM curve for kamacite from Weiss et al. (2017) (Figure 3.12, orange triangles), we predict the magnetic anomaly will lose ∼35% of its magnetization. We carried out this

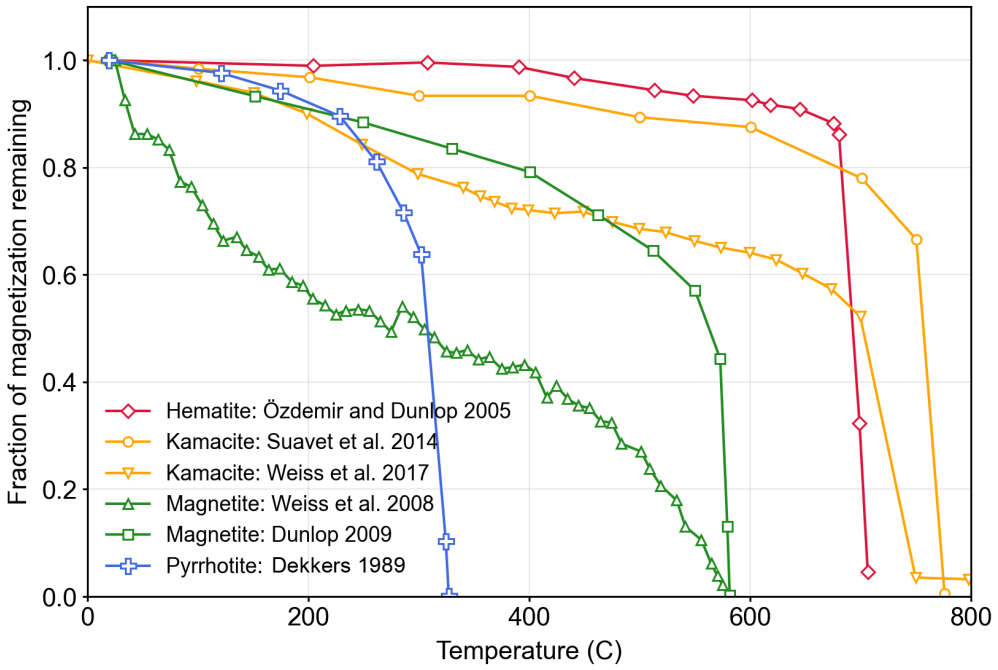

Figure 3.12: Thermal demagnetization curves from laboratory experiments for four magnetic remanence carriers. We use TRM curves from six different papers for four potential magnetic carriers: hematite (Özdemir and Dunlop, 2005), pyrrhotite (Dekkers, 1989), kamacite (Suavet et al., 2014; Weiss et al., 2017), and magnetite (Dunlop, 2009; Weiss et al., 2008). The carriers hematite, kamacite, magnetite, and pyrrhotite correspond to the red, orange, green, and blue curves, respectively. Both kamacite (orange) and magnetite (green) have two TRM curves each. Each of these six curves corresponds to a panel in Figure 3.14.

process for each location marked with a black circle or star in Figure 3.11.

We took the temperature associated with each of the twenty-four points in Figure 3.11 to be the lower bound of the temperature envelope that it is in, i.e., either 200°C, 300°C, 400°C, or 500°C. Choosing the lower bound here yields a lower bound on the fraction of magnetization lost. We took the time associated with each point to be the total amount of time spent above the associated temperature value. Table 3.1 shows these total times for the four points marked with a black star in Figure 3.11. A table showing the time values for all twenty-four points in Figure 3.11 is included in Appendix A.2.

Star label in Figure 3.11	Temperature (°C)	Time spent at temp. or above (kyr)
1	200	8.0
2	300	3.5
3	400	2.6
4	500	1.4

Table 3.1: The temperatures and time spent above these temperatures for each of the points labeled with a black star in Figure 3.11.

To do this partial demagnetization analysis, we must know the magnetic mineralogy of the source bodies, and we must also assume the remanence is carried by single domain grains. Unfortunately, none of these properties of the source bodies are known. Proposals for their origin include highly magnetic volcanic materials (Hemingway and Tikoo, 2018; Purucker et al., 2012) and impact ejecta (Hood et al., 2001; Wakita et al., 2021; Wieczorek et al., 2012). The compositions of these materials are not known.

Given the uncertainty in origin, we consider four different potential magnetic carriers: kamacite, hematite, magnetite, and pyrrhotite. Kamacite is a likely magnetic carrier for endogenous lunar materials (Suavet et al., 2014), but is also found in meteorites (Zhang et al., 1994); it has a Curie temperature of 780°C. Hematite, pyrrhotite, and magnetite are magnetic carriers observed in meteorites (Carporzen et al., 2011; Cournede et al., 2015; Fu et al., 2014; Weiss et al., 2008) and may be present on the Moon from exogenous sources; they have Curie temperatures of 690°C, 325°C, and 580°C, respectively. Given these uncertainties, we estimate that this type of analysis should be able to approximate the remaining magnetization within an order of magnitude, i.e., able to differentiate between 5% remanence remaining vs. 50% remanence remaining.

3.5.4 Modeling the magnetic field from model dipole distributions

In our results section, we show that our thermal demagnetization model predicts demagnetization of a substantial region around the magma intrusion, particularly if the magnetic carriers are magnetite and pyrrhotite. Hence, our next goal is to investigate how the surface marking pattern of swirl soil might change after some of its source bodies have been demagnetized.

Because swirl surface patterns are almost certainly related to the morphology of the near-surface magnetic field, we can model different arrangements of magnetic source bodies before and after thermal demagnetization and compare the resulting near-surface magnetic fields with the swirl pattern. The magnetic field modeling is carried out in three steps: (1) we created an arrangement of magnetic dipoles representing

the source bodies prior to demagnetization, (2) we reduced the demagnetization in a two-dimension region of these dipoles to approximate the effects of demagnetization in that area; the reduction was either 100% (complete demagnetization—an end member scenario) or 50% (partial demagnetization), (3) we calculated the magnetic field from the remaining source body dipoles, and (4) we compared this calculated magnetic field with the markings observed on the surface in this area. In our analysis, we use the horizontal component of the magnetic field because based on previous research (Hemingway and Garrick-Bethell, 2012), this component likely determines which regions of the swirl appear brightest on the surface; horizontal field lines more effectively block the solar wind ions that are responsible for typical surface darkening.

First, we created a 2D (zero vertical thickness) planar grid of dipoles that represents the area of the swirl magnetic source bodies prior to any thermal demagnetization. To construct an *a priori* model of the original, un-demagnetized swirl source bodies, we assumed a straight 2D strip of dipoles (Figure A.5). The process of using the swirl pattern to calculate the latitude and longitude of each dipole in this strip can be found in Appendix A.3.

Next, we estimated the magnetic moment density for the grid of dipoles based on spacecraft observations of the field amplitude in this region. Using two different spherical harmonic models of global magnetic field observations (Ravat et al., 2020; Tsunakawa et al., 2015), we created maps of the horizontal component of the magnetic field out to degree 450 at an altitude of 20 km (20 km is the approximate data collection altitude in this region, Figures 3.13A, 3.13B). For any magnetic moment density among the

strip of dipoles, the morphology of the resulting magnetic field did not closely match the observations from Tsunakawa et al. (2015) or Ravat et al. (2020). In particular, the field pattern is not strip-like or sinuous, like the swirl, implying that our assumed strip-like distribution is too weakly magnetized to dominate the field pattern at 20 km altitude.

To address this issue, we created a two-part dipole model: the first part is the strip described before, and the second part is a point source (single dipole) whose location matches the peak in magnetic field magnitude seen in the Tsunakawa et al. (2015) and Ravat et al. (2020) observations at approximately 304.7°E, 10.85°N. We set the magnetic moment of each dipole such that the combination of the strip dipoles and the point source dipole produced a magnetic field whose magnitude and morphology was similar to the magnetic field observations from Tsunakawa et al. (2015) and Ravat et al. (2020). In particular, the influence of the strip just barely begins to appear in the magnetic field map. In this case, the strip has a magnetic moment of 1.14×10^{12} A·m^2 evenly spread over ∼19,000 dipoles, and the point source is a single dipole with a magnetic moment of 8.57×10^{11} A·m^2 (i.e., ∼75% the moment of the strip, concentrated into a single dipole). Importantly, the strong, single dipole that makes up the point source was only used to help constrain the appropriate magnetic moment for the dipoles contained in the strip; it was not included in our forward modeling in subsequent sections because the focus of this modeling is to investigate the change in the near-surface field as the source bodies near Dome 3 demagnetize, not to recreate every feature in the observed magnetic field. Finally, we note that we cannot be certain that this model is an accurate

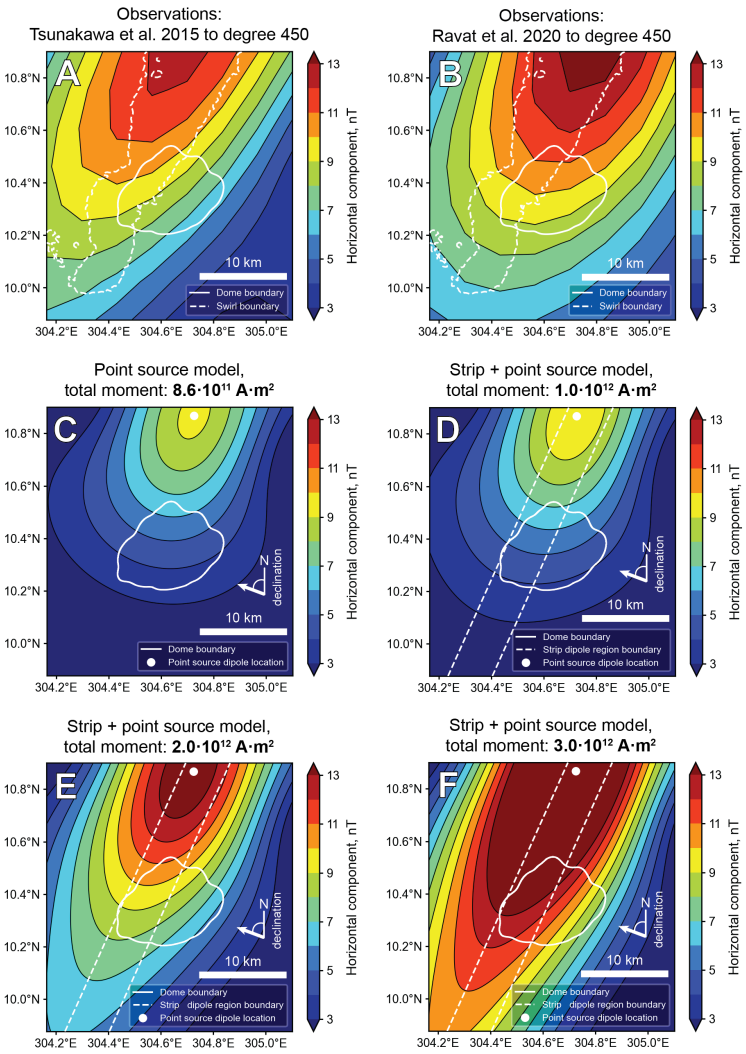

Figure 3.13: A comparison between magnetic field observations from orbit and this work's modeled magnetic fields. The solid white contour line in each panel indicates the Contour Approximation of Dome 3. The location of our model's point source is indicated in C-F with a white dot. (A) The horizontal component of the magnetic field observations from Tsunakawa et al. (2015), out to degree 450. (B) The horizontal component of the magnetic field observations from Ravat et al. (2020), out to degree 450. (C) The horizontal component of the magnetic field produced by a point source dipole whose parameters are described in Section 3.5.4. (D, E, F) The horizontal component of the magnetic field produced by the dipole arrangement described in Section 3.5.4 with three different total magnetic moments: 1×10^{12} A·m^2, 2×10^{12} A·m^2, and 3×10^{12} A·m^2, respectively. The dashed white lines indicate the boundaries of the dipole region prior to demagnetization. (D) shows a scenario where the 2D strip's magnetic moment is too small, (E) shows a scenario where the strip's magnetic moment produces a field that is consistent with observations and used in our modeling work, and (F) shows a scenario where the strip's magnetic moment is too large.

representation of the true magnetization, but certainly there must be some sinuous, strip-like distribution of magnetization to produce the swirl morphology.

The final 2D strip of dipoles consists of 14 parallel, equally-spaced lines of dipoles. Each of the 14 lines has a linear dipole density of 450 dipoles per map degree and strikes at an azimuth of 24° clockwise from north. The width of this grouping of 14 lines of dipoles is 0.19 map degrees (∼5.8 km), and the length is 3.05 map degrees (∼92.4 km). Each of the 14 lines was extended along the strike direction by 1 map degree beyond the edge of the field-modeling window (i.e., off the page) to minimize edge effects in the area of interest. The dipole burial depth was set to 1 km because this value represents both the approximate depth of the model laccolith discussed in Sections 3.5.1 and 3.6.1, as well as likely swirl source body depths (Hemingway and Tikoo, 2018; Kelley and Garrick-Bethell, 2020). The inclination of the dipoles was set to 0°, and the declination of the dipoles was set to -70° (Kurata et al., 2005; Takahashi et al., 2014). This declination value represents the magnetization direction of the tail of Reiner Gamma; the main body has a distinct declination of approximately -11° (Takahashi et al., 2014). We evaluated the field at 2 km altitude, the approximate altitude at which the charged particle/field interaction occurs that determines the swirl morphology (Bamford et al., 2012; Garrick-Bethell and Kelley, 2019). We note that small height differences in the modeling altitude or source-body burial depth are not likely to affect our conclusions.

After creating the initial 2D strip of dipoles, we reduced by 50% and 100% the moments of dipoles within the Contour Approximation that defines the observed limit of the laccolith. The actual spatial extent of demagnetization will be complex and

depend on the magnetic carrier, and may be the subject of future work. Hence our approximations of 100% and 50% demagnetization serve as a first order test on whether the geometry of the field can be grossly reproduced by removing magnetization in the general shape as the magma body.

3.6 Results

3.6.1 Results of elastic flexure modeling of Dome 3 formation

The topography profile of the dome closely resembles an ideal laccolith in the north-south direction (Figure 3.7B). However, in the east-west direction the profile is not as ideal, particularly near the summit, and suggests there is a depression there (Figure 3.7C).

We measured the maximum height of the dome, $w(0,0) = w_0$, to be 325 m above the background topography level (defined to be the topography level beyond the slope breaks just described). These values for c, a, and w_0, along with our choices for individual values of p_d and E described in Section 3.5.1, were all inserted into Equation 3.1 and the overburden thickness h was solved for, yielding 897 m. Because the individual p_d and E values that were used to calculate this h value were chosen to be near the middles of their respective ranges, this particular h value can be seen as a likely middle value of the potential range of overburden thicknesses, rather than a preferred overburden thickness.

In addition to the single values chosen for p_d and E, we calculated the resulting

overburden thickness for each combination of values in the ranges of p_d and E discussed in Section 3.5.1 (Figure 3.8). The highest and lowest values calculated for h are 549 m and 1705 m, respectively. This range of values is compatible with the 500-2500 m estimate for swirl source body burial depths given in Hemingway and Tikoo (2018).

3.6.2 Results of heat flow modeling around Dome 3

We compare the modeled temperatures produced by the laccolith magma body with the TRM curves and Curie temperatures of the four ferromagnetic materials discussed in Section 3.5.3. Figure 3.10 shows the maximum temperature reached by each cell over the run of the thermal model. The solid gray line indicates the boundary of the laccolith; cells within this boundary by definition reached $T_{\text{hot}} = 1175°\text{C}$. Cells immediately outside this boundary only reached 576°C, which implies that areas just tens of meters away from the intruded laccolith would not reach the Curie temperatures of kamacite ($T_{\text{Curie}} = 780°\text{C}$), hematite ($T_{\text{Curie}} = 690°\text{C}$), or magnetite ($T_{\text{Curie}} = 580°\text{C}$). This result agrees with a simple theoretical prediction that at the boundary of a region undergoing thermal diffusion, the maximum temperature reached is halfway between the temperatures of the hot and cool regions (Turcotte and Schubert, 2014). In this case, halfway between T_{hot} and T_{cool} is at 576°C.

The failure of the Curie temperature front around the laccolith to travel any great distance is slightly changed if we consider exogenous magnetic carriers with lower Curie temperatures. The dashed gray contour line in Figure 3.10 encloses cells that reached 325°C (the Curie temperature of pyrrhotite). This boundary is no more than ∼100 m

away from the boundary between the laccolith and the country rock. It should also be noted that the Curie temperature front travels farther away from the laccolith in the vertical direction (∼100 m) than in the horizontal direction (<25 m, the spatial resolution of the model). This is because the laccolith becomes very thin at its edges; it cannot carry a large amount of heat in such a small amount of material.

3.6.3 Results of thermal demagnetization analysis

Figure 3.14 shows the results of our partial thermal demagnetization analysis (Section 3.5.3). The remaining magnetization fractions for each of the twenty-four points in Figure 3.11, as well as the associated laboratory unblocking temperatures we obtained from the Pullaiah diagrams (Figure A.4), can be found in Appendix A.2.

The spatial extent of the demagnetization is not the same in all directions. Above and below the center of the laccolith, cells up to ∼300 m away from the laccolith experience some degree of demagnetization. But in the lateral direction, only cells closer than ∼25 meters (just one pixel in our model's resolution) experience any demagnetization. It should also be noted that the demagnetization envelope does not include the region within the laccolith itself, because in the simplest approximation, the laccolith's emplacement pushes surrounding material out of the way. And additionally, it should be noted that some adjacent envelope regions have demagnetization values very close to one another, making the separate regions unresolvable in Figures 3.14A, 3.14B, 3.14C, and 3.14E.

For the magnetic carrier hematite (Figure 3.14A), material ∼50 meters above and

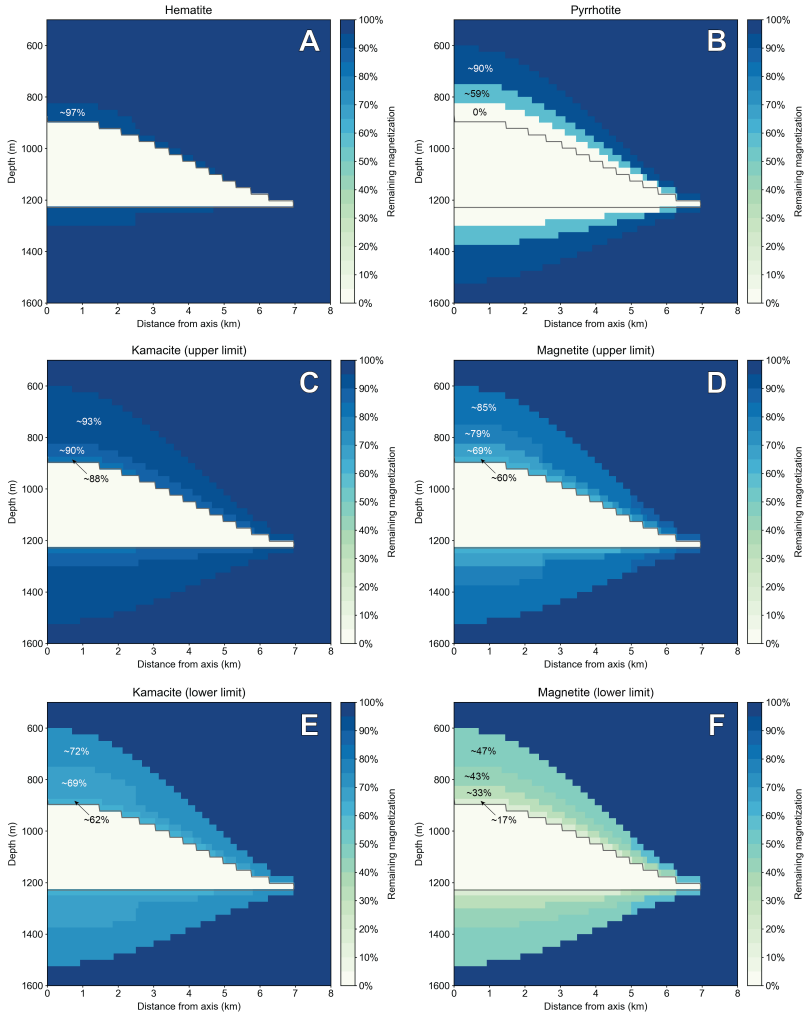

Figure 3.14: Cross-sectional maps showing the amount of magnetization remaining around the intrusion for different magnetic carriers and different TRM curves. Lower and higher limits for kamacite and magnetite are derived from two different laboratory curves for the same mineral. The regions where the magnetization was calculated are shown in Figure 3.11, comprising 24 subdivisions. The single gray contour line (seen most readily in Panel B) indicates the edge of the laccolith. The vertical and horizontal scales are not the same. The "zigzag" edge of the laccolith is due to the resolution of the thermal model (25 meters/pixel) being exaggerated by the vertical scaling. (A) The remaining magnetization around the intrusion using the hematite TRM curve. (B) The remaining magnetization around the intrusion using the pyrrhotite TRM curve. (C) The remaining magnetization around the intrusion using the upper limit kamacite TRM curve. (D) The remaining magnetization around the intrusion using the upper limit magnetite TRM curve. (E) The remaining magnetization around the intrusion using the lower limit kamacite TRM. (F) The remaining magnetization around the intrusion using the lower limit magnetite TRM curve.

below the laccolith has ∼97% magnetization remaining, and then all remaining cells outside the laccolith have 100% of their magnetization remaining. Contrast this behavior with the magnetic carrier pyrrhotite: due to pyrrhotite's Curie temperature (∼325°C) being lower than the $T_{\text{hot}}/T_{\text{cool}}$ midway temperature of 576°C, total demagnetization occurs outside of the boundary of the laccolith.

The remaining four panels in Figure 3.14 show two different results for kamacite and magnetite. For each of these carriers, an upper and lower limit TRM curve (taken from two different laboratory studies) was used to find two different cases of thermal demagnetization. We use "upper limit" to mean a greater amount of remaining magnetization and "lower limit" to mean a lesser amount of remaining magnetization, depending on which study is used for the laboratory TRM curve. For the upper limit TRM curve results, >88% (for kamacite, Figure 3.14C) or >60% (for magnetite, Figure 3.14D) of the magnetization remains around the laccolith. For the lower limit TRM curve results, >62% (for kamacite, Figure 3.14E) or >17% (for magnetite, Figure 3.14F) of the magnetization remains around the laccolith. For the lower limit magnetite case in particular, out to ∼250-300 m above and below the laccolith, only about half of the original magnetization remains in those regions.

A combination of magnetic carriers may be responsible for the magnetization. For example, the magnetization of the meteorite Allende is carried by both pyrrhotite and magnetite (Carporzen et al., 2011; Fu et al., 2014), and exogenous sources such as meteorites may be the source of the magnetic bodies in this region of the Moon (Wakita et al., 2021; Wieczorek et al., 2012). The results shown in Figure 3.14 can be used

to approximate this multicarrier situation via averaging: for a given cell, the amount of magnetization remaining in a multicarrier magnetic source body can be found by calculating a weighted average of the percent magnetization remaining in that cell for each of the different carriers present.

3.6.4 Results of modeling the magnetic field from model dipole distributions

In Figure 3.15 we show the magnetic field that results from the demagnetization (removal of dipoles) of portions of a model source distribution. In Figures 3.15A, 3.15B, and 3.15C, the area between the dashed white lines (the dipole 2D strip) is filled with dipoles prior to demagnetization. In those same panels, the area of demagnetization is located within the solid white contour lines (the Contour Approximation). Figure A.6 shows the resulting magnetic field from the non-demagnetized condition where no dipoles have been removed from the dipole 2D strip. We check to see if our basic model can recreate Features A, B, and C observed in the swirl (Figure 3.4, Figure 3.15D, Section 3.3) in our magnetic field models.

In Figure 3.15A, the dipole 2D strip is narrowed by the thermal demagnetization within the footprint of the Contour Approximation, but not completely severed (white arrow in Figure 3.15A). To better match Feature B, which is the observed local minimum in swirl brightness (which, by proxy, is likely a local minimum in near-surface magnetic field magnitude), we found that the dipole 2D strip needed to be nearly severed. We achieved this severing with two different methods: i) by expanding the dome boundary,

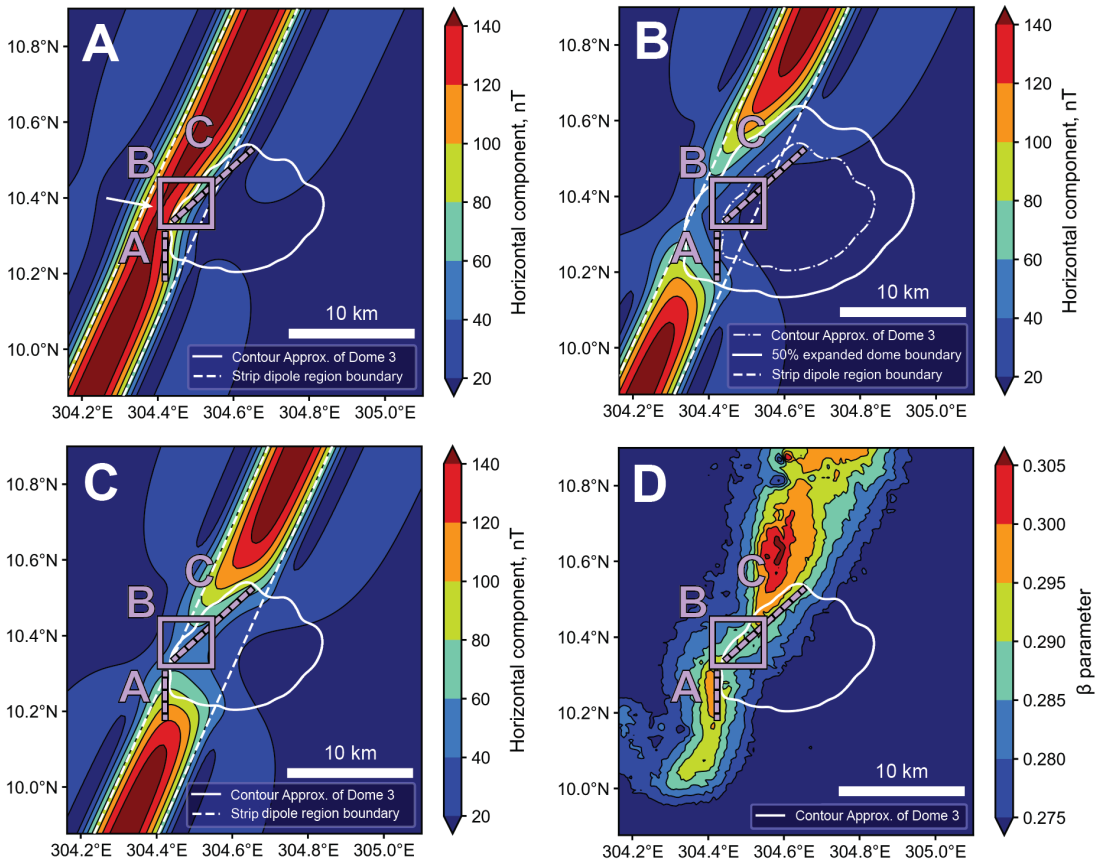

Figure 3.15: The horizontal component of the magnetic fields produced by various arrangements of dipoles as compared to the observed swirl morphology. A strip of dipoles is located between the two dashed white lines (see Figure A.6), and the dipole moments are set to zero when they are inside the region bounded by the solid white line. For each modeling scenario, the horizontal component of the resulting magnetic field is shown with colored contours whose levels are shared between Panels A, B, and C. In Panels A through C, the field is viewed from an altitude of 2 km and only the horizontal component of magnetic fields is shown. We have plotted the swirl pattern with the same colormap and number of contour lines as the magnetic fields are so that the morphologies of the magnetic fields and the swirl can be more easily compared. The purple box and dashed lines indicate Features A, B, and C discussed in Section 3.3. The locations of Features A, B, and C are the same in each panel. (A) The magnetic field from the dipole 2D strip (Figure A.6) demagnetized by the Contour Approximation of the dome boundary (-1420 m topography contour). (B) The magnetic field from the dipole 2D strip (Figure A.6) demagnetized by the Contour Approximation of the dome boundary enlarged by 50%. The dot-dash contour indicates the size of the dome before expansion. (C) The magnetic field from the dipole 2D strip shifted east by 0.095° and demagnetized by the Contour Approximation of the dome boundary. (D) The swirl β parameter, with a solid white line indicating the Contour Approximation of the dome boundary.

and ii) by shifting the strip to the east until it is severed.

With regard to the first method, in Figure 3.15B, the Contour Approximation (dot-dash contour) was expanded by 50% (solid white contour) to sever the dipole 2D strip at the location indicated by the white arrow in Figure 3.15A. This expansion assumes our modeling of the laccolith's boundaries was in error, perhaps due to intruded bodies with a nearly unobservable topographic signature. The magnetic field from this dipole arrangement matches both Features A, B, and C to varying degrees (Figure 3.15D, purple annotations). The field minimum (Feature B) is seen in the model field's strength, and the northeast-southwest strike of the field pattern to the north of Dome 3 (Feature C) is also observed. However, to the southwest of Dome 3, the magnetic field morphology is not as sharp and vertical as in Feature A. Regardless of how closely the morphology of each of the produced magnetic field features match what is observed at the swirl, their locations do not match their respective actual georeferenced locations relative to the dome boundary (Figure 3.15D).

In our second method, we shifted the dipole 2D strip to the east until the original dome boundary severed the dipole 2D strip (total shift of 0.095°, Figure 3.15C). This shift assumes that our *a priori* dipole 2D strip geometry (Figure A.5) may have been in error, perhaps due to the westward displacement of the swirl's modern brightness centroid due to the thermal demagnetization itself. In this scenario, similar to the previous modeling scenario, Features B (Figure 3.15D, box B) and C (Figure 3.15D, line C) are reproduced more strongly than Feature A. However, now each of these features of interest are located much closer to their corresponding georeferenced locations on the

observed swirl (Figure 3.15D, lines/box A, B, and C), but the strike of Feature A is again ∼45° different than the Feature A annotated in Figure 3.15D.

Figure 3.16 shows the same modeling scenarios as Figure 3.15, but the magnetic moments of dipoles inside the solid white contour lines are set to 50% of their initial value, instead of 0% as in Figure 3.15. The case where the Contour Approximation has not been expanded and the dipole strip has not been shifted (Figure 3.16A) produces a similar result to the corresponding case with the dipoles' moments set to 0% of their initial value (Figure 3.15A): the area of high magnetic field has been narrowed but not severed as is required to recreate Feature B. In the case where the Contour Approximation has been expanded and the dipole strip has not been shifted (Figure 3.16B), the area of high magnetic field is again narrowed, but not severed as it was in the case where the dipole moments were set to 0%. However, the strike of the field lines on the southwest flank of the dome (Figure 3.16B, line A) much more closely match the north-south strike of Feature A. Finally, in the case where the Contour Approximation has not been expanded and the dipole strip has been shifted to the east (Figure 3.16C), the area of high field has not been reduced to the same amount that it was in the case where the dipole moments were set to 0%, but the strike of the field lines to the north of the dome approximately match the strike of Feature C.

In summary, both the partial (50%) and total (100%) reductions in dipole strength produced some degree of agreement between model and observations. For all modeling scenarios, the assumption that the initial magnetization distribution was a strip with constant width and strike is not the case in reality. The swirl's sinuosity and the fact that

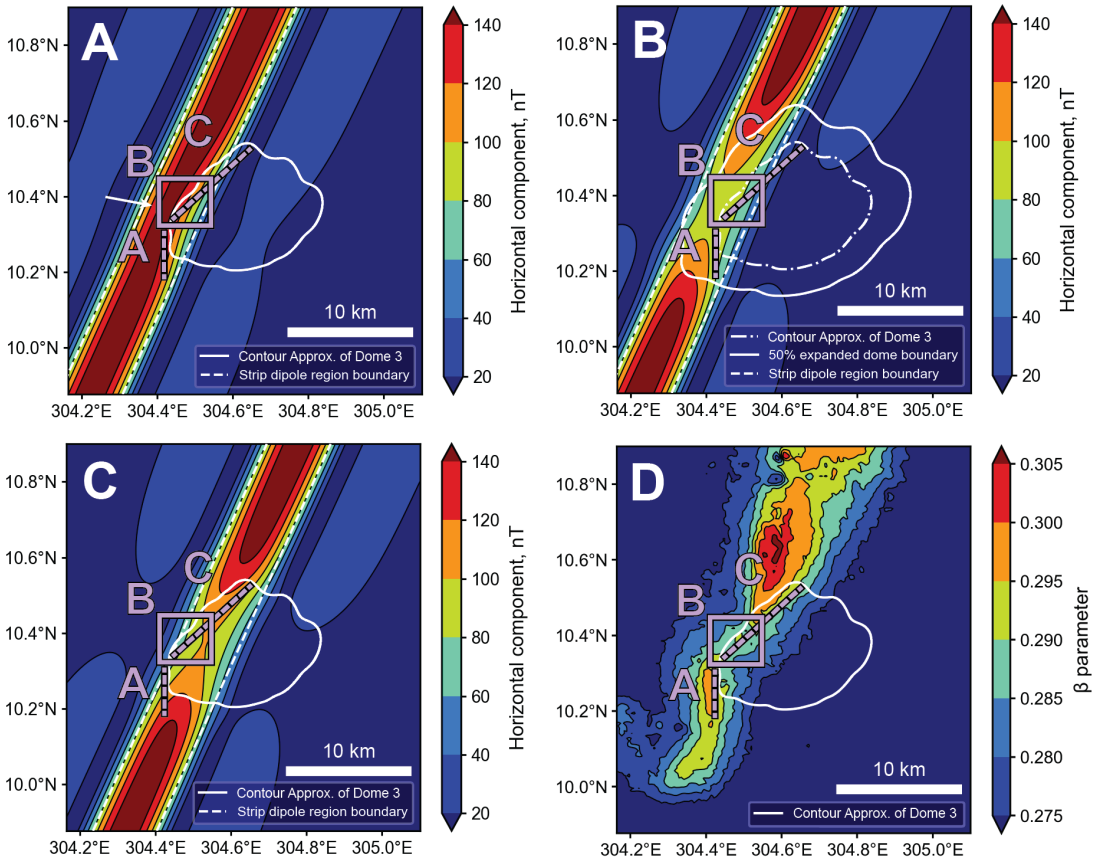

Figure 3.16: The same as Figure 3.15, but with the dipole moments set to 50% of their original value instead of zero, for dipoles within the region bounded by the solid white line. (A) The magnetic field from the dipole 2D strip (Figure A.6) demagnetized by the Contour Approximation of the dome boundary (-1420 m topography contour). (B) The magnetic field from the dipole 2D strip (Figure A.6) demagnetized by the Contour Approximation of the dome boundary enlarged by 50%. The dot-dash contour indicates the size of the dome before expansion. (C) The magnetic field from the dipole 2D strip (Figure A.6) shifted east by 0.095° and demagnetized by the Contour Approximation of the dome boundary. (D) The swirl β parameter, with a solid white line indicating the Contour Approximation of the dome boundary.

the swirl we observe today is in its (potentially) post-demagnetized form, implies that a straight strip based on the swirl's current form is not necessarily the best candidate to represent the initial arrangement of dipoles. Nonetheless, modeling the initial state of the source bodies as a straight strip is an effective way to get the first-order behavior of the magnetic field when some of the source bodies are demagnetized.

3.7 Discussion

Overall, two important modeling results imply that Reiner Gamma tail was indeed thermally demagnetized by Dome 3, and by inference at least Dome 1 (e.g., Figure 3.4) and the other domes in the region (Figure 3.3). Firstly, we find that a substantial fraction of magnetization can be removed by partial thermal demagnetization (Figure 3.14). This means that we do not need to overly tune our model to effect demagnetization—a variety of heat source geometries in the vicinity of the swirl would be sufficient to remove some of the magnetization. Indeed, similar processes have been inferred for volcanic regions on Mars (Lillis et al., 2015). Secondly, our magnetic field forward models are relatively successful in producing Features A, B and C that are observed in the swirl morphology. These findings are broadly consistent with the overall pattern of the swirl tail winding between the centers of six domes in the region (Section 3.3). In the remaining sections, we infer additional properties of the magnetic source bodies under the assumption that they have been thermally demagnetized.

3.7.1 Magnetic source body ages

We infer that the source bodies must be located within the local basalt layer, and hence Reiner Gamma must have been emplaced during the mare volcanism epoch. This argument is based on the observation that the full range of plausible burial depths from all magma driving pressures and Young's moduli is 550 m to 1700 m (Figure 3.8). Furthermore, the source bodies must be located within the envelope of demagnetization around the laccolith. Based on our thermal modeling, demagnetization may extend ∼300 m above and below the base of the laccolith. Thus, the total range of possible magnetic source body burial depths is ∼250 m to ∼2.3 km (∼550 m overburden layer thickness minus ∼300 m partial demagnetization envelope thickness for the minimum burial depth, and ∼1700 m overburden layer thickness plus ∼300 m thick laccolith plus ∼300 m partial demagnetization envelope for the maximum burial depth). This estimated range includes all depths that could experience any level of partial thermal demagnetization, i.e., it is not merely a depth-to-top of the source.

A burial depth range of ∼250 m to ∼2.3 km compares favorably to swirl source body depths as calculated in other works, most notably Hemingway and Tikoo (2018). They estimate that the depth to the top of the swirl source body does not exceed the light-to-dark transition length scale observed in the albedo pattern on the surface. For the region in this work, the light-to-dark transition length scale of the swirl along the northwest flank of the dome is ∼2 km, which is within our range of depths affected by a nonzero amount of partial thermal demagnetization.

We can compare our calculated burial depth to regional basalt thicknesses. Gong et al. (2016) finds total basalt thickness at the Marius Hills to be 3-4 km thick. Hence, we can conclude that the magnetic source bodies were emplaced and magnetized (and later demagnetized) during the period of mare basalt emplacement, which began at ∼3.9 Ga and continued in the region until ∼3.5 Ga (Hiesinger et al., 2003). This is also consistent with the findings of Kelley and Garrick-Bethell (2020), who found that the Reiner Gamma magnetic source bodies were emplaced within the mare basalts. Because the high field epoch of the lunar dynamo overlapped with the mare volcanism epoch (Weiss and Tikoo, 2014), this could explain the high magnetic fields found at Reiner Gamma.

3.7.2 Source body magnetizations

We estimate the magnetization of the magnetic source bodies by dividing the total magnetic moment of all the 2D strip dipoles in our model by the volume over which these dipoles are distributed: $M = m/(l \times w \times t)$, where m is the magnetic moment, and l, w, and t are the length, width, and thickness of the source body, respectively. The magnetic moment of the 2D dipole strip is 1.143×10^{12} A·m^2, and the width and length of the 2D dipole strip are 0.19 map degrees (∼5.8 km) and 3.05 map degrees (∼92.4 km), respectively.

The thickness t is chosen based on the height over which the demagnetization occurred, which depends on the degree of demagnetization around the laccolith. We can set the thickness t to be the total thickness of the envelope around the laccolith

that experiences any degree of demagnetization. This thickness is ∼600 m (Figure 3.14) for all the considered magnetic carriers with the exception of hematite. For $t = 600$ m, the corresponding magnetization value is 3.6 A/m. If we assume that only half of the magnetization has been removed, then the inferred magnetization is 7.2 A/m. These lower bounds on the magnetization can be compared to the 0.5 A/m lower bound presented in Hemingway and Tikoo (2018). We remark that there is some uncertainty in the actual magnetic field value at 20 km altitude that is due to the portion of the swirl near Dome 3 (Section 3.5.4) and hence similar uncertainty in the magnetization value. Future measurements of the field at lower altitudes could better constrain the magnetization of the swirl.

3.7.3 Era of a weak magnetic field

A natural implication of our results is that the dynamo field was weak or non-existent at the time of swirl source body demagnetization. The range of dome ages in our area of study is approximately 1.0-3.3 Ga (Hiesinger et al., 2016). If thermal demagnetization with no subsequent remagnetization occurred at any point in this time range, it implies that there was no global field (or a very weak global field) at the time of dome emplacement. This result is consistent with the high-field epoch of the lunar dynamo ending by approximately 3.56 Ga (Weiss and Tikoo, 2014). Other scenarios that may be consistent with a thermal demagnetization age of 1.0-3.3 Ga are a dynamo that was only episodically strong (Evans and Tikoo, 2022), or a dynamo that existed in a weakened state (Tikoo et al., 2014). It is also possible that the field was reversed

during the heating event, such that newly acquired TRM was reversely magnetized, and thereby nullified the total magnetization. However, we currently do not have sufficient information to determine the plausibility of these alternate scenarios.

3.7.4 Extrusive volcanism

If we assume that the particular dome studied in this work was formed by extrusive processes rather than intrusive processes (Lena et al., 2013; Weitz and Head, 1999), many of the same concepts related to heat transfer and demagnetization still apply. From the results of our thermal model, the lava emplaced on the surface still needs to surround the magnetic source bodies (Figure 3.5C), which in this case implies that the magnetic source bodies need to be located very near the surface when the eruption took place. While the Marius Hills domes may not be monogenetic (Lena et al., 2013), a single lava flow from the dome's center could thermally demagnetize nearby magnetic source bodies given if the flow is thick enough (at least the thickness of the source bodies) and emplaced quickly enough. Individual lava flows in this area are likely ∼20-220 m (Hiesinger et al., 2002), which may be thick enough to demagnetize a range of possible source body thicknesses.

3.8 Conclusion

We propose that the morphology of the tail of Reiner Gamma swirl is partially controlled by thermal demagnetization by at least one dome (Dome 3), but also likely five others (Figures 3.3, 3.4). This demagnetization explains why the swirl appears to

wrap around the flanks of Domes 1 and 3, and does not cross the other domes. We find three morphological features in the swirl brightness pattern at Dome 3 that suggest the magnetic source bodies were nearly severed by this thermal demagnetization. By modeling Dome 3 as a laccolithic intrusion, we estimate the regions that would have undergone thermal demagnetization. Using the results of our laccolith, thermal, and magnetic models, we place an upper bound on the burial depth of swirl source bodies in this region at $\sim$2 km. Given that mare basalts in the region are 3-4 km thick, this establishes the emplacement age of the source bodies during the age of mare volcanism, with an age range of 3.5-3.9 Ga. This age range coincides with the high field epoch, and is in agreement with the emplacement process and age estimate of Reiner Gamma in Kelley and Garrick-Bethell (2020) and Garrick-Bethell and Kelley (2019). These source bodies were then subsequently demagnetized after the time of mare volcanism during era with a weak dynamo field (Tikoo et al., 2014) or possibly an era without a dynamo field (Evans and Tikoo, 2022). We estimate the magnetizations of the magnetic source bodies in this region to be at least 3.6 A/m. Given their lower Curie temperatures, magnetite and pyrrhotite are the most promising candidates for the magnetic minerals, which would be consistent with exogenous source materials (Wakita et al., 2021; Wieczorek et al., 2012; Hood et al., 2001).

Chapter 4

Magnetic field morphology correlated with surface slopes at the Gerasimovich lunar magnetic anomaly

Abstract

The lunar magnetic anomalies in the region of the crater Gerasimovich are among the highest-magnitude anomalies on the Moon. Previous work (Hood and Artemieva, 2008; Lin et al., 1988; Wakita et al., 2021) has suggested that the source of this magnetic anomaly is magnetized ejecta from the impact that formed the Crisium basin, and we present results that support this antipodal ejecta hypothesis. We observe a correlation between areas of low slope and areas of high magnetic field, suggesting that after their deposition, the magnetic source bodies experienced downslope movement and preferentially collected in flat regions. We create a magnetic model based on this scenario, and

are able to reproduce several features that are in the observed magnetic field. Additionally, we also estimate the thickness of the magnetized layer using both older crater craters that may have been filled with magnetized ejecta and younger craters that destroyed portions of the magnetic layer. Using crater fill, we estimate the layer thickness to be ∼0.8-1.2 km, and using crater disruption of the magnetic layer, we estimate the layer thickness to be ∼2.4 km. From the former result, we then estimate the source body magnetization to be ∼3-5 A/m.

4.1 Introduction and background

The Moon sustained a global magnetic field at some point in its past, likely driven by a dynamo (Weiss and Tikoo, 2014). Although the global magnetic field no longer exists, multiple regions of magnetic anomalies were left behind in the Moon's crust (Hood et al., 2001; Tsunakawa et al., 2015). Understanding the magnetic source bodies of these anomalies would allow us to better understand when the Moon's dynamo field was active and its strength. However, the geologic context of these magnetic anomalies are poorly understood; few studies have been carried out that strongly constrained how these magnetic anomalies formed. Some previous work has investigated particular magnetic anomalies (Garrick-Bethell and Kelley, 2019; Kelley and Garrick-Bethell, 2020; Purucker et al., 2012; Wakita et al., 2021), but the geologic formation mechanisms of magnetic anomalies elsewhere in general remain elusive.

The group of Gerasimovich magnetic anomalies, located to the west of the Orien-

tale basin and near the Crisium basin antipode, exhibit some of the strongest magnetic fields observed from lunar orbit (Figure 4.1). Previous work has hypothesized that the high magnetic fields in the Gerasimovich region are due to highly magnetized ejecta from the impact that formed the Crisium basin (Lin et al., 1988; Mitchell et al., 2008; Wakita et al., 2021). If this hypothesis is true, we would expect a topographic signature of the magnetic source bodies: places where the ejecta fell and collected. This work will focus on testing the antipodal ejecta hypothesis via analyzing the relationship between topography, surface slope, and magnetic field in the region of the Gerasimovich magnetic anomalies. We find that areas of low surface slopes tend to be collocated with areas of high magnetic field, which suggests that the observed magnetic fields are due to magnetized ejecta collecting in low-slope areas.

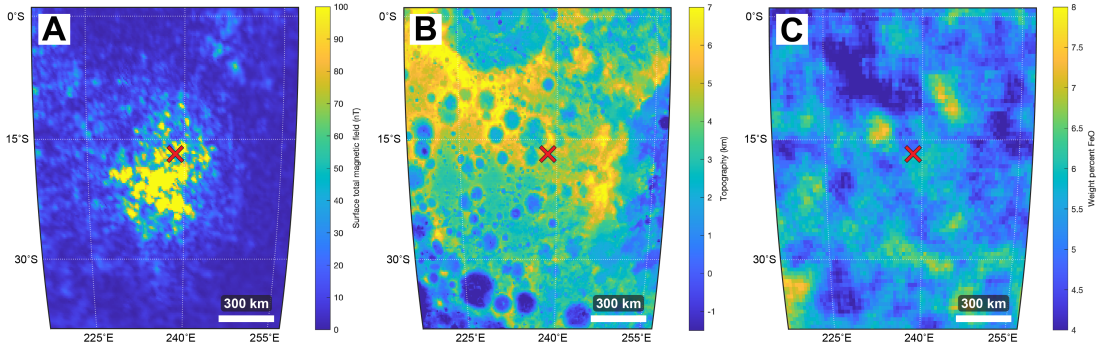

Figure 4.1: Context for the region of the Gerasimovich magnetic anomalies. The Crisium antipode is marked with a red "X". (A) Total magnetic field. Note that the peak magnetic field is 672 nT, but the colormap is saturated to 100 nT. (B) Lunar Orbiter Laser Altimeter (LOLA) topography. (C) Lunar Prospector iron content.

Our approach to testing the antipodal ejecta hypothesis is in three steps. After showing that the areas of low slope are collocated with areas of high magnetic field, we

then model the magnetic field with source bodies whose magnitude is set by areas of low surface slope, to see how well it reproduces the features in the observed magnetic data. Second, we compare the depths of craters in this area with other craters with approximately the same diameter. If the craters older than Crisium near Gerasimovich are shallower than expected, then they may be filled with ejecta, which supports the antipodal ejecta hypothesis. We also compare the craters older than Crisium with their theoretical depths as derived from crater scaling relationships. These analyses yield an estimate for the thickness of the magnetized layer, which in turn allows us to calculated a magnetization value for the source material. And third, we analyze craters in this area that are younger than Crisium to see if they have an effect on the morphology of the observed magnetic field. If they do, this suggests that the impacts that made these craters were able to destroy part of the magnetized layer. Thus, calculating the depths of these younger craters allows us to place a second constraint on the thickness of the magnetized layer.

4.2 Relationship between magnetic field and surface slope

For our magnetic field data, we use the Tsunakawa et al. (2015) SVM model at a resolution of 5ppd. For our topographic data, we use Lunar Orbiter Laser Altimeter (LOLA) maps at 32ppd (Smith et al., 2010). We created the surface slope map by calculating the arctangent of the magnitude of the gradient of the LOLA topography map; its units are degrees from the horizontal.

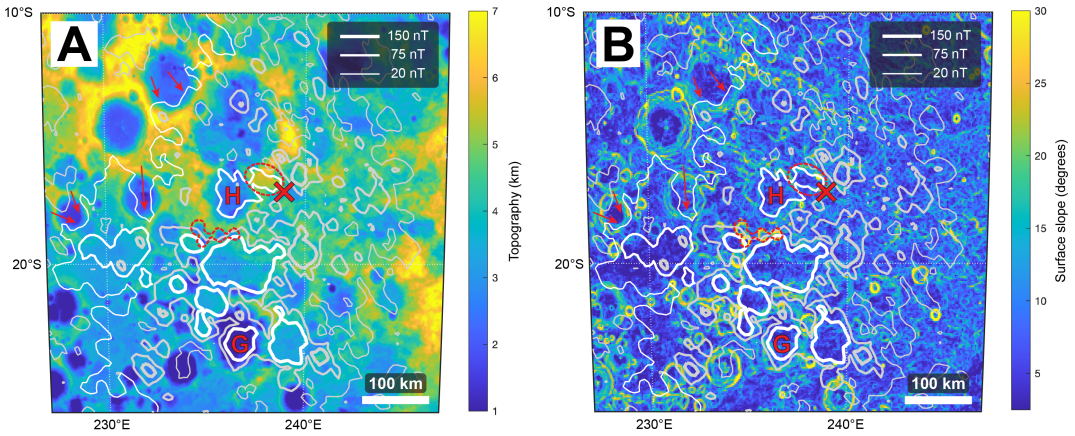

Figure 4.2: Magnetic field contour lines over topography (panel A) and surface slope (panel B) maps. The magnetic field contour lines are shown at 20 nT, 75 nT, and 150 nT (thick, medium, and thin contour lines, respectively). The Crisium antipode is marked with a red "X", and the floors of the craters Houzeau and Gerasimovich are marked with "H" and "G", respectively. Areas where the magnetic field contour lines appear to follow crater rims are indicated with red arrows, a high-field area with low surface slope and high topography is indicated with a dashed red oval, and four craters that appear on the northern edge of the broadest peak in magnetic field (see Section 4.5) are indicated with a dashed red outline at approximately 235°E, 18°S. The white contour lines indicate areas where the magnetic field appears most strongly correlated with areas of low slope, while all other contour lines are shown in gray.

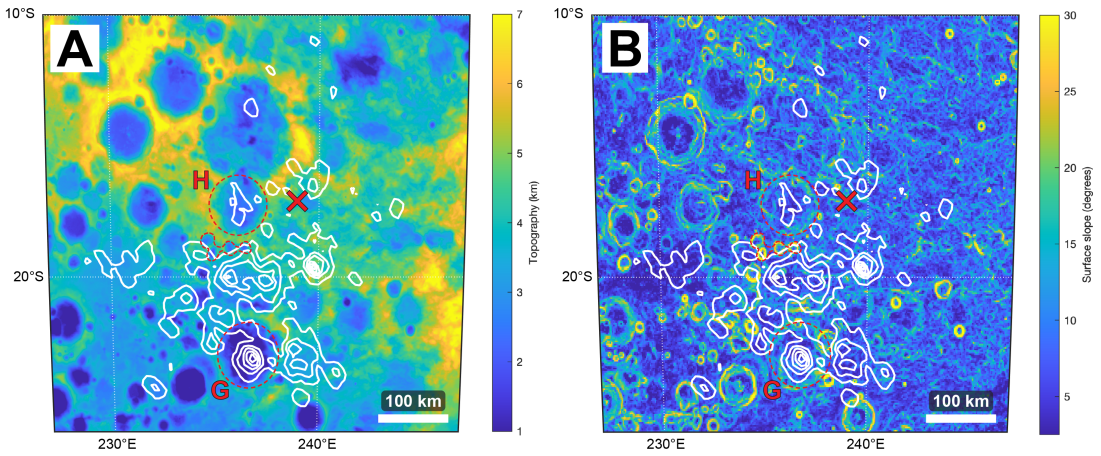

Figure 4.3: The same background maps as Figure 4.2, but with evenly spaced magnetic field contours shown on top. The contour lines are every 100 nT from 100 nT to 600 nT, and the peak magnetic field value in this window is 672 nT. The Crisium antipode is marked with a red "X", and the craters Houzeau and Gerasimovich are marked with dashed red circles and "H" and "G", respectively. Four craters that appear on the northern edge of the broadest peak in magnetic field (see Section 4.5) are indicated with a dashed red outline at approximately 235°E, 18°S.

We compare the magnetic field contours over the topography map (Figures 4.2A, 4.3A) and the same contours over the surface slope map (Figure 4.2B, 4.3B). We show both selected magnetic field contour lines (Figure 4.2) and evenly-spaced magnetic field contour lines (Figure 4.3). The selected contour lines in Figure 4.2 of 20 nT, 75nT, and 150 nT (all below the peak magnetic field value of 672 nT in this area) are meant to encircle the peaks of the magnetic field while still revealing the background map at the location of the peaks. The maps with the evenly spaced contour lines (Figure 4.3) demonstrate that including all contour lines up to the peak magnetic field value obscures the background maps at the locations of the magnetic field peaks, which are the regions of interest in this work.

We make two main observations about the contour lines of the magnetic field shown in Figure 4.2. First, in the topography background map (Figure 4.2A), a high in magnetic field is clearly correlated with the crater Gerasimovich in the south. The magnetic field contours are correlated, but less obviously so, with the crater Houzeau in the north. These correlations could lead one to believe that the magnetic field is highest within craters, but this leaves the relatively flat areas with high magnetic field between Gerasimovich and Houzeau unexplained. Additionally, the area of high magnetic field on the northeastern rim of Houzeau is not located within a crater (Figure 4.2A, dashed red ellipse). Second, in the slope background map (Figure 4.2B), each of the highest peaks in the magnetic field is more clearly correlated with areas of low surface slope. The floors of Gerasimovich and Houzeau are observed as in the topography background map, but now the low-slope region between the two is also correlated with the magnetic field peaks there. Additionally, the area of high magnetic field on the northeastern rim of Gerasimovich is collocated with an area of low surface slope (Figure 4.2B, dashed red ellipse). The magnetic field contour lines over surface slope, rather than topography, demonstrate that the areas of high magnetic field are correlated with areas of low surface slope, regardless of if these flat areas are at low elevation (i.e., the floor of the crater, as at Gerasimovich) or at high elevation (i.e., the plateau between Gerasimovich and Houzeau).

The areas of high magnetic field, and thus the areas with a high concentration of magnetic source bodies, are correlated with flat areas. This relationship is consistent with the antipodal ejecta hypothesis because the ejecta would experience downslope

movement over time and collect at areas of low surface slope (Ikeda et al., 2022; Kokelaar et al., 2017; Kreslavsky and Head, 2012; Senthil Kumar et al., 2016).

4.3 Magnetic field forward modeling

4.3.1 Methods

We determine that areas of low surface slope are better correlated with areas of high magnetic field than are areas of low topography. To show this point, we modeled the magnetic source bodies as a collection of dipoles whose locations and magnetic moments were set by the slope map (Figure 4.2B, background map). We began with a grid of uniformly spaced dipoles with the same resolution as the Tsunakawa et al. (2015) magnetic field map, 5 pixels per degree. The grid was a square with side length 40° centered the approximate center of the group of Gerasimovich magnetic anomalies (237°E, 20°S). This grid extends past the edges of the maps in Figures 4.2 and 4.3 so that any edge effects from the modeled field will not manifest in our window of interest 16° in latitude and 20° longitude. The total number of dipoles in this grid was 40,000. We set the moments of the dipoles in two different ways. First, we set the dipole moments to be inversely proportional to the topography values: the coordinate with the lowest topography value corresponded to the dipole with the highest moment and the coordinate with the highest topography corresponded to the dipole with a moment of zero. Second, we set the dipole moments to be inversely proportional to the surface slope values: the coordinate with a surface slope of zero corresponded to a dipole with

the highest moment and the coordinate with the maximum surface slope corresponded to a dipole with a moment of zero. Between the two extremes, the dipole moments varied linearly, and the peak moment was set to be 10^{11} A·m^2. This peak moment was chosen such that the peak magnitude of the resulting magnetic field approximately matched that of the peak observations in this area. These dipole moment values will be revisited in later sections when we calculate the approximate magnetization of the putative ejecta layer.

As a final step we linearly decreased the magnetic moment of the dipoles in our modeling space as a function of distance from the center of the grouping of anomalies at 237°E, 20°S, according to the following equation:

$$m = -\frac{1}{R}d + 1 \tag{4.1}$$

where m is the resulting moment, R is a constant that represents the distance over which the dipole moments fall to zero, and d is the distance of a given dipole from the center. We chose R to be $12^\circ \approx 300$ km, because this is the approximate observed radius of the observed magnetic anomalies. This decrease in dipole moments is done to more accurately represent the finite, grouped nature of the observed magnetic anomalies. The modeling case without the linear decrease in dipole moment is discussed in Appendix B (Figure B.1).

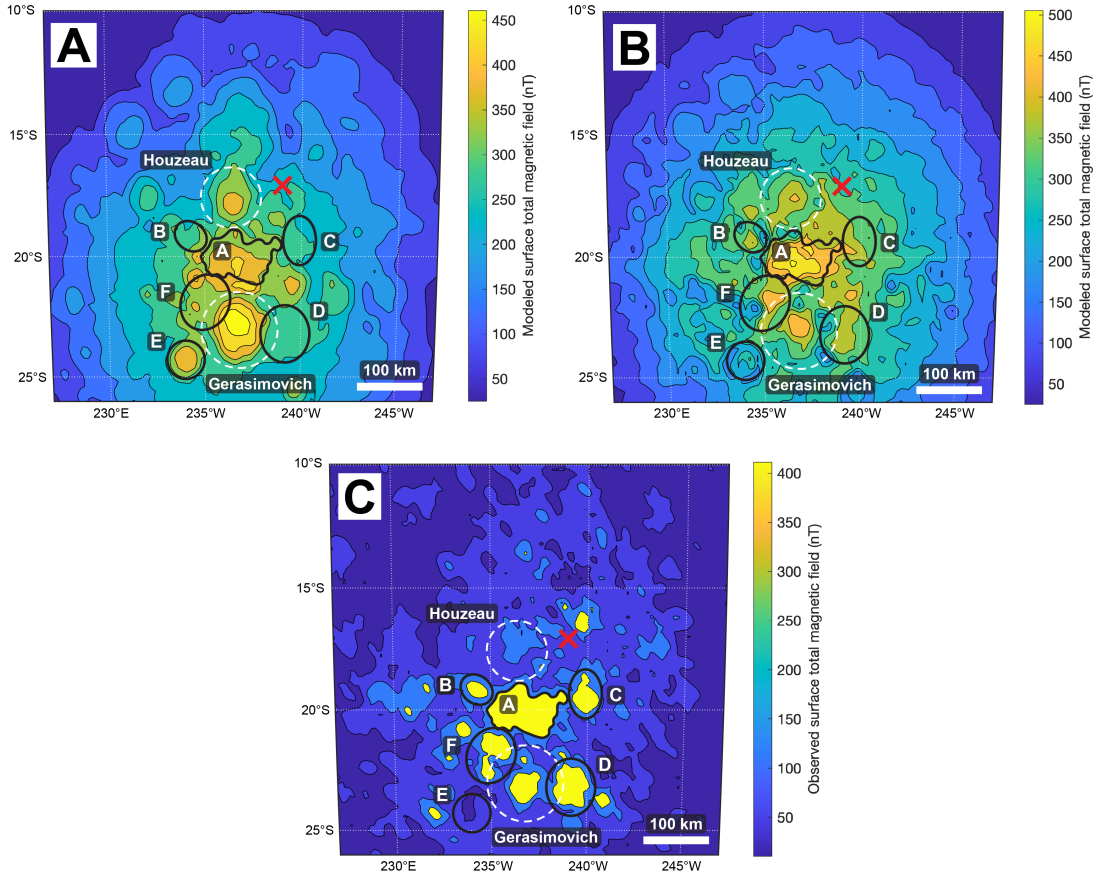

Figure 4.4: Modeled magnetic fields as compared to observed magnetic fields, with craters indicated with dashed white circles and features of interest indicated with heavy black lines. The Crisium antipode is indicated with a red "X". The annotations are in the same locations in each panel. (A) Modeled magnetic field with moments set by topography, with linear decrease in dipole moment over 12°. (B) Modeled magnetic field with moments set by surface slope, with linear decrease in dipole moment over 12°. (C) The observed magnetic field from Tsunakawa et al. (2015) with the same contour levels as Figure 4.2.

4.3.2 Results and interpretation

In the field from moments set by topography (Figure 4.4A), peaks are observed to coincide with the craters Gerasimovich and Houzeau (Figure 4.4, dashed white circles), which matches the observed magnetic field. Additional features to compare between the modeled and observed fields are indicated with heavy black lines, and will be referred to by their letter label. A broad peak is seen between the two crater-centered peaks, but it is located slightly too far south to be collocated with the peak between Gerasimovich and Houzeau that is present in the observed magnetic fields (Feature A). The modeled field does not have Features B, C, and D, which are peaks in the observed magnetic field. Additionally, the modeled field does produce an extra peak labeled Feature E, which is not present in the observed field. And finally, the modeled field produces only part of Feature F, which is a two-lobed peak seen in the observed field. Features D and F are locations are where the surface is at relatively high topography (along/outside the rim of the crater Gerasimovich), so the corresponding dipole moments are not high enough relative to the dipoles within Gerasimovich to produce an additional peak in magnetic field.

The field from moments set by surface slope (Figure 4.4B) overcomes most of the issues with the field from moments set by topography. As with the topography-set case, this modeled field produces peaks in the magnetic field over crater floors at Gerasimovich and Houzeau (Figure 4.4, dashed white circles). Additionally, the broad peak between the two craters is more closely aligned with Feature A's location in the

observed field. Features B and D, which are peaks in the observed field, are produced to a limited amount in the modeled field. Feature C, another peak in the observed field, is not produced by this modeled field. However, Feature F, the two-lobed peak on the northwest rim of Gerasimovich is produced by this modeled field much better than in the topography-set modeled field. And finally, the slope-set modeled field does not produce Feature E, which was the extra peak present in the topography-set modeled field but not in the observations. Overall, the slope-set modeled field better reproduces the observed magnetic field. Thus, areas of low surface slope are better correlated with areas of high magnetic field than are areas of low topography.

This correlation suggests the following mechanism for the formation of highly magnetized source bodies located at areas of low surface slope: first, the antipodal ejecta strikes the surface, and undergoes downslope movement induced by impact and surface shaking (Kreslavsky and Head, 2012; Senthil Kumar et al., 2016). Second, the hot ejecta cools, records the ambient magnetic field, and becomes magnetized (Wakita et al., 2021). Third, this material is covered by ejecta from the formation of the nearby Orientale basin, burying the magnetized ejecta and masking any mineralogical signatures from orbital observations (for example, iron, see Figure 4.1C). This mechanism contradicts the idea that the antipodal ejecta can become shock magnetized on impact because it undergoes so much movement after the first contact. Additionally, the peak shock pressures on landing from sub-orbital speeds are at most $\sim$12 GPa (Garrick-Bethell et al., 2020), which is too low for substantial shock magnetization (Tikoo et al., 2015a,b).

4.4 Older craters filled with antipodal ejecta

4.4.1 Methods

Another approach to testing the magnetized antipodal ejecta hypothesis is to determine if craters older than the Crisium basin-forming impact are anomalously shallow (i.e., filled) as compared to other craters their age. We accomplish this by comparing the measured crater depths to their theoretical depths from scaling relationships developed by Krüger et al. (2018). The relationships derived in that work do not separate out craters by age, only by size and mare/highland location, so we will also compare each of our four Gerasimovich-area craters to the depths of two other craters that are similar in diameter, one Copernican in age (1.1 Ga to present) and one Nectarian in age (3.92-3.85 Ga). The exception is Crater Y; there are no Copernican-aged craters at that size, so we compare its depth to two Nectarian-aged craters at that size. Explicitly separating out Copernican and Nectarian-aged craters serves to capture a variety of different degradation states in our comparisons, to be sure that degradation is not the cause of any of our four Gerasimovich-area craters being anomalously shallow.

First, we choose four craters in our region of study that are older than the impact that formed the Crisium basin, as determined by their classifications according to the Ji et al. (2022) geologic map (as well as by the classifications of the craters that overprint them in this geologic map). The four that we will focus on are Houzeau, Gerasimovich, and two unnamed craters that we will refer to as Crater X and Crater Y (Figure 4.6, black circles). The coordinates, diameters, depths, rim heights, and relative age of each

of these four craters, as well as the craters that we compare them to, are shown in Figure 4.5. A map showing context for these craters is shown in Figure B.2.

We found the diameter and the depth of each of these twelve craters with azimuthal averaging over angles where its rim is intact. Once the azimuthally averaged profile of each crater was calculated, we were able to obtain the diameter by doubling the distance from the center of the crater to the highest point on the time, and the depth of the crater by subtracting the lowest-elevation point from the highest-elevation point on the profile. We visualize azimuthally-averaged profiles of each of these four sets of craters in order to determine if any are anomalously shallow (Figure 4.7).

Additionally, we calculate the depth of each crater as predicted by the scaling relationships in Krüger et al. (2018):

$$d = 1.11 \cdot D^{0.290} \tag{4.2}$$

$$d = 1.12 \cdot D^{0.289} \tag{4.3}$$

where d is the depth of the crater and D is the measured diameter of the crater. Equation 4.2 is valid for highland craters in the transitional size range ($\sim$13-37 km diameter) and was used for the group of craters that included Crater X, and Equation 4.3 is valid for highland craters in the complex size range ($\sim$25-100 km diameter) and was used for the groups of craters that included Houzeau, Gerasimovich, and Crater Y. We calculate the ratio between the theoretical crater depth and the measured crater depth; a ratio value >1 indicates that the crater is shallower than its theoretical depth and a ratio value of <1 indicates that the crater is deeper than its theoretical depth. The results of these

Crater	Longitude (°E)	Latitude (°N)	Diameter (km)	Depth (m)	Rim height (m)	Period
Crater X	234.47	-19.81	24.8	2556	561	Ferroan anorthositic suite
Theaetetus	6.05	36.99	24.5	2579	621	Copernican
Feoktistov X	139.55	33.01	25.5	2684	168	Nectarian
Houzeau	236.19	-17.23	83.6	2839	814	Aitkenian
Jackson	196.67	22.02	72.7	4139	1237	Copernican
Einthoven	110.02	-5.19	78.2	4042	791	Nectarian
Gerasimovich	236.58	-22.95	90.9	3611	998	Nectarian, covered by Imbrian-age ejecta
Tycho	348.79	-43.36	86.4	4433	1285	Copernican
Bridgman	137.05	43.36	84.1	4061	1275	Nectarian
Crater Y	236.53	-14.46	152.7	3754	1581	Ferroan anorthositic suite, covered by Imbrian-age ejecta
Roche	136.57	-42.35	157.6	3236	1227	Nectarian
Sommerfeld	198.30	64.62	151.5	4330	1048	Nectarian

Figure 4.5: Table showing the coordinates, measured diameter, measured depth, measured rim height, and relative age of each crater in our area of study. Each set of three craters represents a group that contains one of our study craters in the Gerasimovich area (gray shading) and two similarly-sized craters that we compare it to. The age classifications were taken from Ji et al. (2022).

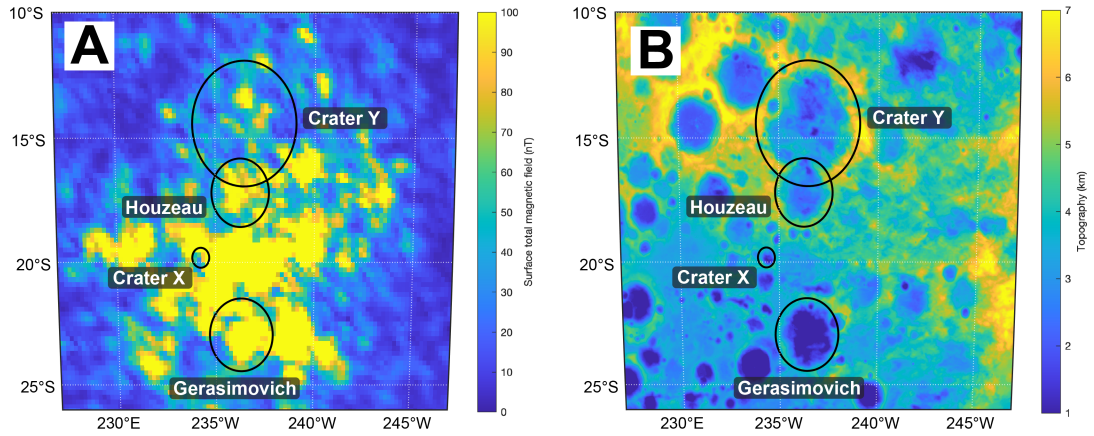

Figure 4.6: Context map for the Gerasimovich-areas craters in Figure 4.5 (rows with gray shading). (A) Magnetic field map of the area around Gerasimovich, with annotations showing the four craters of interest in the area. (B) Topographic map of the area around Gerasimovich, with annotations showing the four craters of interest in the area.

calculations can be found in Figure 4.8.

4.4.2 Results and interpretation

As seen in Figure 4.8, there are two cases where craters in the Gerasimovich area are shallower than expected as compared to their similarly-sized craters located elsewhere: Houzeau and Gerasimovich (rows 4-6 and rows 7-9, respectively). Houzeau is 42% shallower than expected, while its comparison craters, Jackson and Einthoven, are only 7% and 2% deeper than their theoretical depths, respectively. To a lesser extent, Gerasimovich follows this result: it is 14% shallower than expected, while its comparison craters, Tycho and Bridgman, are 8% and 1% deeper than their theoretical depths, respectively. These results can also be seen when comparing our azimuthally-averaged profiles of these two crater groups: the profiles for Houzeau and Gerasimovich

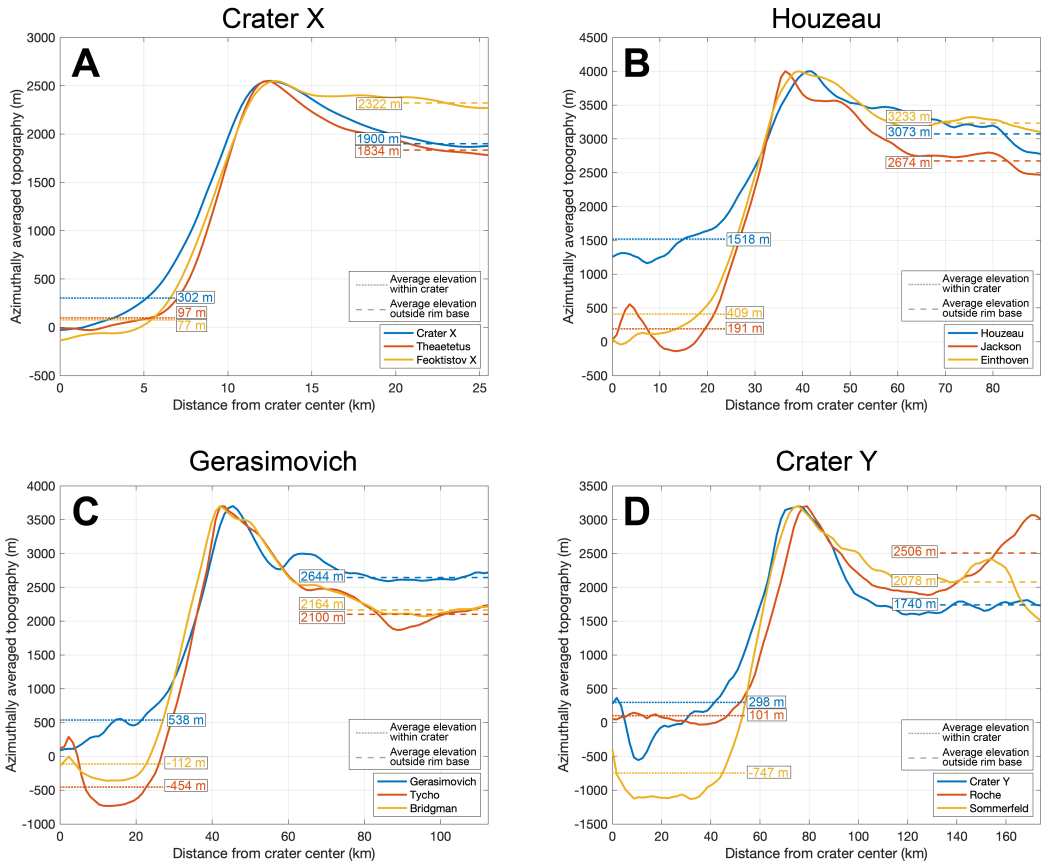

Figure 4.7: Azimuthally averaged topography of four craters that are within the Gerasimovich magnetic anomaly (crater name given at top of panel; gray shaded craters in Figure 4.5) and older than Crisium. Each of these four craters is compared with two other craters of similar size and different ages. The average floor elevations and average outside-rim elevations are indicated with dotted and dashed horizontal lines, respectively. (A) The azimuthally averaged profiles of Crater X, Theaetetus, and Feoktistov X. (B) The azimuthally averaged profiles of Houzeau, Jackson, and Einthoven. (C) The azimuthally averaged profiles of Gerasimovich, Tycho, and Bridgman. (D) The azimuthally averaged profiles of Crater Y, Roche, and Sommerfeld.

	Crater name	Measured depth (m)	Theoretical depth (m)	Depth ratio (theoretical/ measured)	Comparison to expectation
1	Crater X	2556	2817	1.10	shallower
2	Theaetetus	2579	2808	1.09	shallower
3	Feoktistov X	2684	2838	1.06	shallower
4	Houzeau	2839	4025	1.42	shallower
5	Jackson	4139	3866	0.93	deeper
6	Einthoven	4042	3947	0.98	deeper
7	Gerasimovich	3611	4123	1.14	shallower
8	Tycho	4433	4063	0.92	deeper
9	Bridgman	4061	4031	0.99	deeper
10	Crater Y	3754	4790	1.28	shallower
11	Roche	3236	4834	1.49	shallower
12	Sommerfeld	4330	4779	1.10	shallower

Figure 4.8: The measured depths, theoretical depths, and depth ratios of each of the twelve craters. They gray shaded craters are in the vicinity of the Gerasimovich magnetic anomaly. The final column indicates if the crater is deeper or shallower than its theoretical depth as calculated by Equation 4.2 (rows 1-3) or Equation 4.3 (rows 4-12).

(Figures 4.7B and 4.7C, solid blue lines) are shallower within the crater rims than their comparison craters (Figures 4.7B and 4.7C, solid yellow and orange lines).

The results for Crater X and Crater Y are less conclusive. While the theoretical depths of each of these craters are shallower than expected (Figure 4.8, rows 1 and 10), their comparison craters are also shallower than expected (Figure 4.8, rows 2-3 and 11-12). In the case of Crater X's group, all three craters are within 10% of their expected depth. In Crater Y's group, the spread is larger with Roche being almost 50% shallower than expected. If all three craters in each group are shallower than expected, this renders the comparison between Gerasimovich-area and non-Gerasimovich-area craters inconclusive. The inconclusive results for these two crater groups can also be seen in the comparison of the craters' azimuthally averaged profiles. The profiles for Crater X and Crater Y (Figures 4.7A and 4.7D, solid blue lines) are not that visually different than their comparison craters (Figure 4.7A and 4.7D, solid yellow and orange lines). However, these two crater groups giving inconclusive comparison results does not contradict the fact that Houzeau and Gerasimovich are shallower than expected. When the antipodal ejecta impacted the surface in this region, it likely did not do so in a perfectly uniform manner after its long travel time, affecting some preexisting craters more than others. And indeed, the grouped peaks in the observed magnetic field suggest groups of source bodies, rather than the more uniform ejecta blankets that are common closer to an impact site.

Under the assumption that the craters Houzeau and Gerasimovich are filled with magnetized antipodal ejecta, we now estimate the thicknesses of this fill and use it to

place a constraint on the magnetization of the source bodies. This process was carried out by Wakita et al. (2021) for Houzeau only; here we confirm their result that Houzeau is anomalously shallow and also carry out the process on the crater Gerasimovich. The difference in average floor elevation between Houzeau and Jackson is 1327 m, and the difference between Houzeau and Einthoven is 1109 m. The average of these two values is 1218 m, which we will approximate as Houzeau possessing a fill layer that is ∼1.2 km thick. The difference in average floor elevation between Gerasimovich and Tycho is 992 m, and the difference between Gerasimovich and Bridgman is 650 m. The average of these two values is 821 m, which we will approximate as Gerasimovich possessing a fill layer that is ∼0.8 km thick.

To convert these thickness values into source body magnetization, we use the equation $M = m/(A \times t)$, where M is magnetization in A/m, m is magnetic moment in Acotm^2, A is the area of the source body in m, and t is the thickness of the source body in m. We set t as the thickness values calculated above, and set A as the area of the floor of each of the craters as found with $A = \pi r^2$ and the following highland crater rim diameter/floor diameter relationship from Krüger et al. (2018) for radius r:

$$R_{\text{floor}} = \frac{1}{2}(0.249 \cdot D^{1.205}) \tag{4.4}$$

where R_{floor} is the radius of the crater floor and D is the measured diameter of the crater. The magnetic moment m was set by summing up the magnetic moments of each dipole within the area A, centered on either Houzeau or Gerasimovich, in our forward modeling scenario where the dipole moments were set by the surface slope (see Section

4.3.1). Figure 4.9 summarizes these values and the resulting magnetization values.

Crater name	R_{floor} from Eqn. 4	Area A (km^2)	Thickness t (km)	Magnetic moment m ($A \cdot m^2$)	Magnetization M (A/m)
Houzeau	25.8	2089.3	1.2	$7.97 \cdot 10^{12}$	3.2
Gerasimovich	28.5	2556.4	0.8	$9.37 \cdot 10^{12}$	4.6

Figure 4.9: Source body parameters and resulting minimum magnetization values for Houzeau and Gerasimovich, assuming their fill deposits are entirely Crisium ejecta.

The calculated source body magnetization values for the fill in the interiors of Houzeau and Gerasimovich are 3.2 A/m and 4.6 A/m, respectively. These values are lower bound magnetization values because they assume that the entire fill of the craters is from magnetized ejecta. In reality, some of the crater fill may be Orientale ejecta, due to this region's proximity to that basin. For comparison, Wakita et al. (2021) found a source body magnetization of 29 A/m from a representative source body thickness of 700 m. Additionally, Hemingway and Tikoo (2018) find a magnetization of ∼2 A/m for magnetic source bodies in regions with lunar swirls (some of which are observed around Gerasimovich), and Seritan and Garrick-Bethell (2022, under review) find a magnetization of ∼3.6 A/m for source bodies of the lunar swirl Reiner Gamma. As a lower bound, this work's magnetization estimates are in general agreement with previous studies.

The ejecta covering this region would be expected to fall outside the craters as well as inside them, so we also consider the difference in average elevations outside the rim base of Houzeau and Gerasimovich. In the case of Houzeau (Figure 4.7B), the

elevation outside the rim base is between that of Jackson and Einthoven, which suggests that there is no abnormally thick fill layer outside the rim of Houzeau. In the case of Gerasimovich (Figure 4.7C), the elevation outside the rim base is ∼500 m higher than that of Tycho and Bridgman, which suggests that there is a layer of extra material around Gerasimovich. This layer outside of Gerasimovich, ∼0.5 km thick, is less thick than the layer inside of Gerasimovich found in the previous paragraph, ∼0.8 km thick. However, the values are relatively comparable, and a thickness of ∼0.5 km rather than ∼0.8 km would decrease the estimated magnetization to ∼2.9 A/m, which still agrees well with other studies (Hemingway and Tikoo, 2018; Seritan and Garrick-Bethell, 2022, under review).

4.5 Younger craters damaging the magnetic layer

4.5.1 Methods

Our final approach to testing the magnetized antipodal ejecta hypothesis is to determine if craters younger than the Crisium basin-forming impact have disturbed the layer of magnetized material in a way that is observable in the present-day magnetic field. If we observe that a crater younger than Crisium (and thus, younger than the magnetic source bodies) destroys a portion of the magnetized layer, then we can use the depth of this crater to constrain the thickness of the magnetized layer.

First, we list which craters in our region of study are younger than the impact that formed the Crisium basin. We select four small (<∼22 km) craters south of Houzeau

crater that are likely Orientale secondaries, are listed as being in the ferroan anorthositic suite by Ji et al. (2022), and appear collocated with the edge of a broad peak in the observed magnetic field: Houzeau Q, Houzeau P, and two nearby unnamed craters that we will refer to as Crater A and Crater B (Figure 4.11, black circles). These craters are indicated in Figures 2 and 3 with a dashed red outline at approximately 235°E, 18°S. We compare these four craters to other craters in other areas that fall in four different age ranges (Figure B.3).

	Crater or group of craters	Diameter (km)	Depth (m)	Rim height (m)
1	Houzeau P	15.2	2461	199
2	Houzeau Q	21.6	2153	30
3	Crater A	18.4	2509	480
4	Crater B	16.0	2359	55
5	Nectarian craters (n=4)	15.3	1493	208
6	Imbrian craters (n=4)	15.6	1385	252
7	Eratosthenian craters (n=8)	19.0	3006	487
8	Copernican craters (n=8)	19.5	3191	618

Figure 4.10: Table showing the coordinates, measured diameter, measured depth, measured rim height of each crater in our area of study (rows 1-4) and the averages of these measurements for groups of craters (rows 5-8). See Figures B.1 and B.3 for detailed information about the constituent craters for each of the groups in rows 5-8.

As when considering craters older than Crisium in the previous section, we will calculate the theoretical depths of each of the craters, or groups of craters, in Figure 4.10. For each row in the table, we will calculate two different theoretical depths using scaling

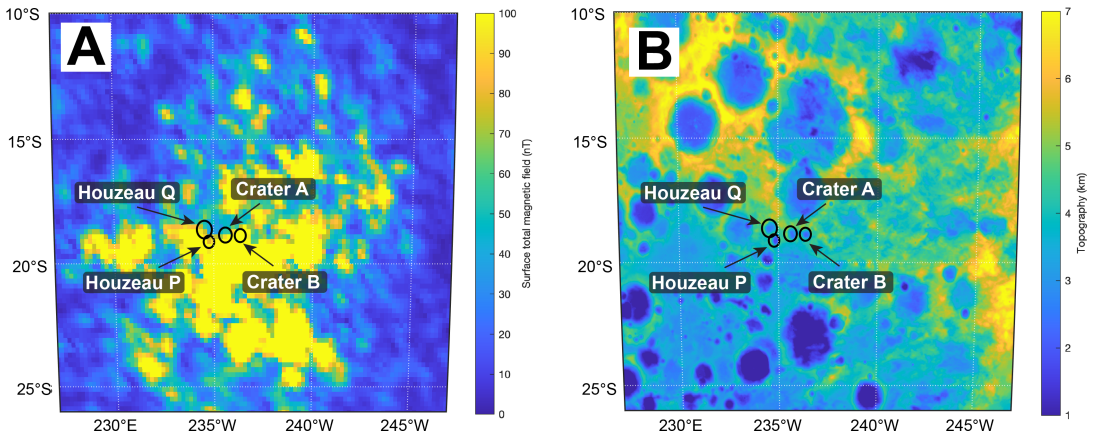

Figure 4.11: Context map for the Gerasimovich-areas craters in Figure 4.10 (rows 1-4). (A) Magnetic field map of the area around Gerasimovich, with annotations showing the four craters of interest in the area. (B) Topographic map of the area around Gerasimovich, with annotations showing the four craters of interest in the area. Note that these four craters appear on the northern edge of the broadest peak in magnetic field at approximately 235°E, 18°S.

relationships from Krüger et al. (2018): one derived for craters in the transitional (∼13-37 km) size range, and one derived for craters in the simple size range (∼3-17 km). We calculate both versions because our crater diameters lie approximately between the two size ranges (Krüger et al. (2018), their Figure 3). The depth as a function of diameter for transitional craters is the same as Equation 4.2, and the depth as a function of diameter for simple craters is as follows:

$$d = 0.1868 \cdot D^{1.0077} \tag{4.5}$$

where d is the depth of the crater and D is the measured diameter of the crater. As done in the previous section, we calculate the ratio between the theoretical crater depths and the measured crater depths; a ratio value >1 indicates that the crater is shallower than its theoretical depth and a ratio value of <1 indicates that the crater is deeper than its

theoretical depth. The results from the scaling relationship for transitional craters can be found in Figure 4.12, and the results from the scaling relationship for simple craters can be found in Figure 4.13.

	Crater or group of craters	Measured depth (m)	Transitional theoretical depth (m)	Depth ratio (theoretical/ measured)	Comparison to expectation
1	Houzeau P	2461	2444	0.99	deeper
2	Houzeau Q	2153	2706	1.26	shallower
3	Crater A	2509	2583	1.02	shallower
4	Crater B	2359	2480	1.05	shallower
5	Nectarian craters (n=4)	1493	2445	2.16	shallower
6	Imbrian craters (n=4)	1385	2459	2.06	shallower
7	Eratosthenian craters (n=8)	3006	2602	0.87	deeper
8	Copernican craters (n=8)	3191	2614	0.85	deeper

Figure 4.12: The measured depths, theoretical depths from the scaling relationship for transitional craters, and depth ratios of each of the craters or groups of craters. The final column indicates if the crater is deeper or shallower than expected.

4.5.2 Results and interpretation

When considering the four craters in the Gerasimovich area as transitional craters (Figure 4.12, rows 1-4), they are all within 5% of their expected value, with the exception of Houzeau Q, which is 26% shallower than expected. This can be contrasted with the craters groups at different ages: the Nectarian and Imbrian craters are much shallower than expected for their size, perhaps due to degradation over their lifetime. The Eratosthenian and Copernican craters are much deeper than expected for their size, perhaps because they are the younger of the age ranges. The theoretical/measured

	Crater or group of craters	Measured depth (m)	Simple theoretical depth (m)	Depth ratio (theoretical/ measured)	Comparison to expectation
1	Houzeau P	2461	2899	1.18	shallower
2	Houzeau Q	2153	4131	1.92	shallower
3	Crater A	2509	3515	1.40	shallower
4	Crater B	2359	3053	1.29	shallower
5	Nectarian craters (n=4)	1493	2919	2.58	shallower
6	Imbrian craters (n=4)	1385	2976	2.55	shallower
7	Eratosthenian craters (n=8)	3006	3631	1.22	shallower
8	Copernican craters (n=8)	3191	3737	1.19	shallower

Figure 4.13: The measured depths, theoretical depths from the scaling relationship for simple craters, and depth ratios of each of the craters or groups of craters. The final column indicates if the crater is deeper or shallower than expected.

ratio for the four craters in the Gerasimovich area fall between these two extremes. When considering the four craters in the Gerasimovich area as simple craters (Figure 4.13, rows 1-4), they range from 18% to 92% shallower than expected. In this case, the crater groups at different ages are all shallower than expected, with the Nectarian and Imbrian craters much more shallow than expected (over twice as shallow) while the Eratosthenian and Copernican craters are only ∼20% more shallow than expected. The theoretical crater depths derived for transitional-sized craters better replicates the measured depths of the Gerasimovich-area craters (Figure 4.12, rows 1-4) than the relation for simple craters. Additionally, it represents the relative degradation states of the non-Gerasimovich-area craters (Figure 4.12, rows 5-8) better than the relation for simple craters.

Because the four Gerasimovich-area craters are collocated with the edge of a peak

in the magnetic field and are younger than the impact that formed the Crisium basin, we can assume that they have disturbed the magnetized layer. Thus, the average depth of these four craters can give us a bound on the thickness of the magnetized layer. The average of their measured depths is 2371 m, and the average of their theoretical depths from Equation 4.2 is 2553 m. These putative ∼2.4-2.5 km layer thicknesses are approximately double the ∼0.8-1.2 km layer thicknesses obtained in Section 4.4.2. Heterogeneities in the magnetized layer, which would be expected for a collection of antipodal ejecta, may explain the difference between our two different magnetized layer thickness values, but further work is needed.

4.6 Conclusions

We observe that the areas of high magnetic field around the Gerasimovich magnetic anomalies are collocated with areas of low surface slope. We created a magnetic model, setting the dipole moments as inversely proportional to the surface slope, and found that the resulting field reproduces key features in the observed magnetic field. There are at least two craters in this region that are older than the impact that formed the Crisium basin, and that appear to be filled with magnetic antipodal ejecta from this impact. We estimate the thickness of this fill to be ∼0.8-1.2 km, and the magnetization of this ejecta to be ∼3-5 A/m. Craters younger than the Crisium impact appear to disturb the magnetic field, suggesting that they disrupted a layer of magnetized ejecta. Assuming that these younger craters penetrated the entirety of the magnetic layer, we

give an additional estimate of its thickness to be ∼2.4 km.

Appendix A

Chapter 3 Supplementary Information

A.1 Derivation of the finite difference approximation for 2D axisymmetric heat flow

The general form of the diffusion equation is:

$$\dot{T} = \kappa \nabla^2 T \tag{A.1}$$

where, in this case, $T = T(r, \theta, z, t)$ is temperature in three spatial (r, θ, z) coordinates and one time (t) coordinate, and κ is thermal diffusivity. The Laplace operator in cylindrical coordinates can be written as:

$$\nabla^2 T = \frac{1}{r}\frac{\partial}{\partial r}\Big(r\frac{\partial T}{\partial r}\Big) + \frac{1}{r^2}\frac{\partial^2 T}{\partial \theta^2} + \frac{\partial^2 T}{\partial z^2} \tag{A.2}$$

The second term on the right hand side of Equation A.2 is zero in the axisymmetric assumption because any derivatives with respect to the azimuthal coordinate are zero.

Setting this term equal to zero and using the chain rule on the first term yields:

$$\nabla^2 T = \frac{1}{r}\frac{\partial T}{\partial r} + \frac{\partial^2 T}{\partial r^2} + \frac{\partial^2 T}{\partial z^2} \tag{A.3}$$

Now the Laplace operator can be reinserted into the diffusion equation (Equation A.1):

$$\frac{\partial T}{\partial t} = \kappa\Big(\frac{1}{r}\frac{\partial T}{\partial r} + \frac{\partial^2 T}{\partial r^2} + \frac{\partial^2 T}{\partial z^2}\Big) \tag{A.4}$$

This is the analytic form of the axisymmetric form of the diffusion equation. The next step is to apply the finite difference approximation to discretize it. We will use forward difference in time and central difference in space. Each of the four derivative terms Equation S4 can be approximated as follows:

$$\frac{\partial T}{\partial t} \rightarrow \frac{T_{i,j}^{m+1} - T_{i,j}^{m}}{\Delta t} \tag{A.5}$$

$$\frac{\partial T}{\partial r} \rightarrow \frac{T_{i+1,j}^{m} - T_{i-1,j}^{m}}{2\Delta r} \tag{A.6}$$

$$\frac{\partial^2 T}{\partial r^2} \rightarrow \frac{T_{i-1,j}^{m} - 2T_{i,j}^{m} + T_{i+1,j}^{m}}{\Delta r^2} \tag{A.7}$$

$$\frac{\partial^2 T}{\partial z^2} \rightarrow \frac{T_{i,j-1}^{m} - 2T_{i,j}^{m} + T_{i,j+1}^{m}}{\Delta z^2} \tag{A.8}$$

where m is the index in time, i is the index in the r direction, and j is the index in the z direction. After inserting Equations A.5-A.8 into Equation A.4 and solving for $T_{i,j}^{m+1}$, you obtain:

$$T_{i,j}^{m+1} = T_{i,j}^{m} + \kappa\Delta t\left[\frac{1}{r}\frac{T_{i+1,j}^{m} - T_{i-1,j}^{m}}{2\Delta r} + \frac{T_{i-1,j}^{m} - 2T_{i,j}^{m} + T_{i+1,j}^{m}}{(\Delta r)^2} + \frac{T_{i,j-1}^{m} - 2T_{i,j}^{m} + T_{i,j+1}^{m}}{(\Delta z)^2}\right] \tag{A.9}$$

which is the next state of the array of temperature values (time index $m+1$) in terms of the current state of the array of temperature values (time index m).

A.2 Pullaiah diagram results from Section 3.5.3

In Figure A.1, letters A-X refer to the twenty four areas around the laccolith. Areas are labeled alternating above and below the laccolith, starting in the outermost envelope, moving outwards from the axis, then proceeding to the next outermost envelope. Pairs of locations that have the same adjacent row coloring (for example, rows A and B) are mirrored above and below the laccolith.

A.3 Construction of a 2D strip of dipoles to represent the swirl magnetic source bodies

The 2D strip's strike direction and width were determined from the β parameter map (Figure A.5). For the strip strike, we found the average *beta* value in the background area (dashed gray box). Setting this value as the base value, we then drew contour lines around the brightest 5% of points (Figure A.5, solid red contour lines). Of the two regions of the brightest 5% pixels, we calculated the location of the centroid (Figure A.5, small red points and large red circles). These two centroids were connected by a line whose slope defines the strike of the magnetized dipole-strip (Figure A.5, heavy dashed red line; the equation of this line is $y = 2.2253x$–667.1094).

For the strip width, we drew contour lines around the brightest 50% of points (Figure A.5, dashed white lines). We then drew lines outwards from the two centroid points to this 50% contour, perpendicular to the strike line (Figure A.5, solid white lines). The average value of the lengths of these two lines were averaged and taken to

Area name	Temp. (°C)	Time spent at or above temp. (kyr)	Laboratory unblocking temperature, kamacite (°C)	Percentage of magnetization left, Suavet et al. 2014 TRM curve	Percentage of magnetization left, Weiss et al. 2017 TRM curve	Laboratory unblocking temperature, magnetite (°C)	Percentage of magnetization left, Dunlop 2009 TRM curve	Percentage of magnetization left, Weiss et al. 2008 TRM curve	Laboratory unblocking temperature, hematite (°C)	Percentage of magnetization left, Özdemir & Dunlop 2005 TRM curve	Laboratory unblocking temperature, pyrrhotite (°C)	Percentage of magnetization left, Lillis et al. 2015 TRM curve
A	200	8	410	93	72	320	85	47	410	97	230	90
B	200	8.9	410	93	72	320	85	47	410	97	230	90
C	200	3.8	400	94	72	310	85	49	400	98	230	90
D	200	3.1	390	94	73	310	85	49	400	98	230	90
E	200	0.2	370	94	74	300	86	56	390	98	230	90
F	200	0.2	370	94	74	300	86	56	390	98	230	90
G	300	3.5	490	90	69	400	79	43	470	97	310	59
H	300	5.5	500	90	69	400	79	43	480	96	310	59
I	300	1.4	480	91	70	390	80	43	470	97	310	59
J	300	1.6	480	91	70	390	80	43	470	97	310	59
K	300	0.02	440	92	72	380	81	43	440	97	310	59
L	300	0.06	450	91	71	380	81	43	450	96	310	59
M	400	2.6	560	88	66	470	69	33	520	94	N/A	0
N	400	2.7	560	88	66	470	69	33	520	94	N/A	0
O	400	0.4	550	89	67	460	70	34	510	95	N/A	0
P	400	0.6	550	89	67	460	70	34	510	95	N/A	0
Q	400	0.06	530	89	67	450	72	35	500	96	N/A	0
R	400	0.06	530	89	67	450	72	35	500	96	N/A	0
S	500	1.4	630	85	62	530	60	17	570	93	N/A	0
T	500	1.5	630	85	62	530	60	17	570	93	N/A	0
U	500	0.3	620	86	63	520	61	19	560	94	N/A	0
V	500	0.4	620	86	63	520	61	19	560	94	N/A	0
W	500	0.03	600	87	64	520	61	19	560	95	N/A	0
X	500	0.03	600	87	64	520	61	19	560	95	N/A	0

Figure A.1: The coordinates, ages, measured diameters, measured depths, and measured rim heights for the aggregated craters in Section 4.5.

represent the width of the 2D dipole-strip. The center of the strip was also centered on the line connecting the two centroids. The final 2D dipole-strip boundary is shown in Figure A.5 with heavy red lines. In reality, we do not know the exact relationship between the width of the source body and the width of the swirl, but a source body width that includes the brightest 50% of the swirl is a reasonable choice that allows for the field from the source bodies to produce swirl patterns beyond their physical boundary. This would be consistent with the fact that solar wind plasma interacts with the field at a variety of altitudes and distances from the source bodies. Furthermore, we later adjust the east-west position of the strip more precisely, such that its exact width is not a critical parameter.

A.4 Supplementary Figures

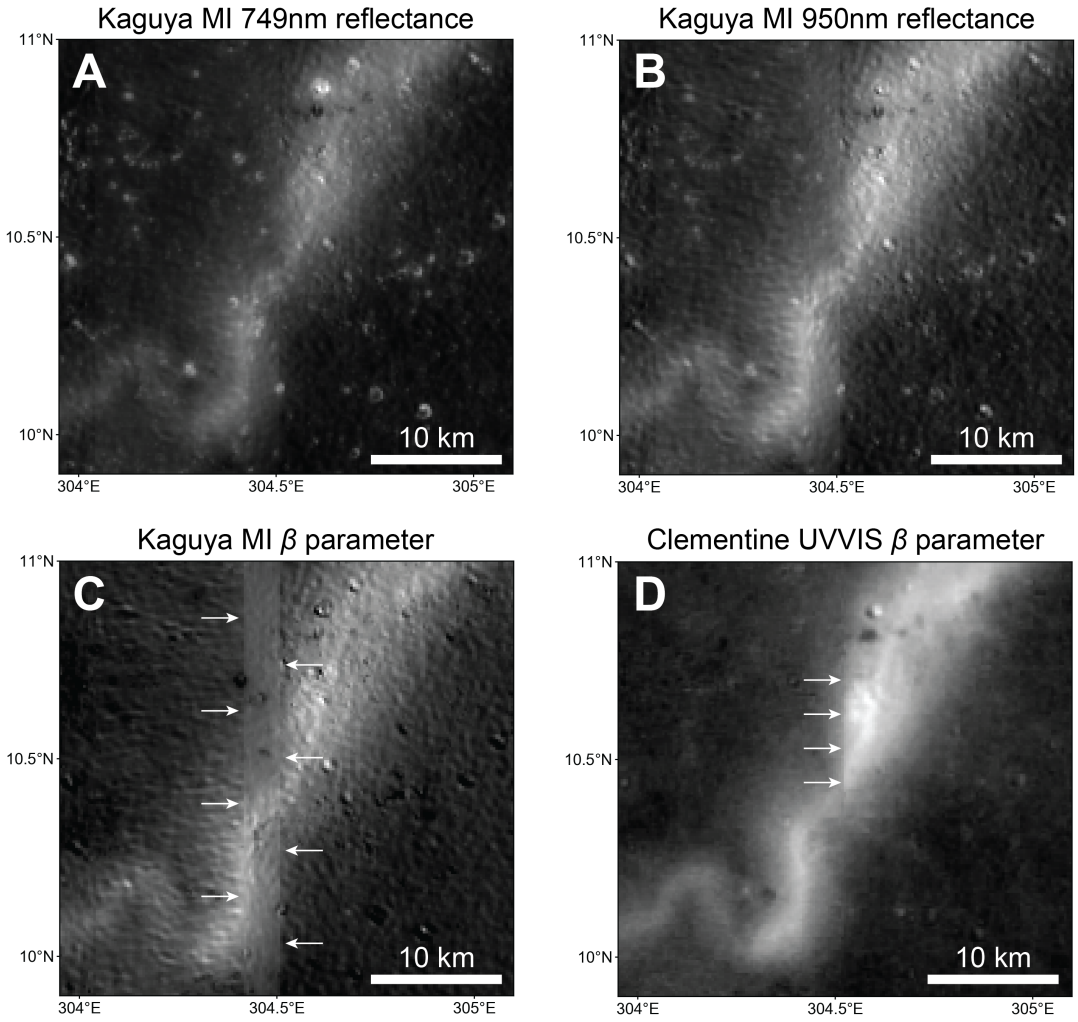

Figure A.2: A comparison between reflectance and β parameter in the area studied in this work. (A) 749 nm reflectance taken by the Multiband Imager (MI) instrument on Kaguya. (B) 950 nm reflectance taken by the Multiband Imager (MI) instrument on Kaguya. (C) Kaguya β parameter combining the information in (A) and (B) following the method in McFadden et al. (2019). White arrows indicate the north-south linear feature. (D) Clementine β parameter, as shown in earlier figures. White arrows indicate the location of a similar north-south feature as seen in (C).

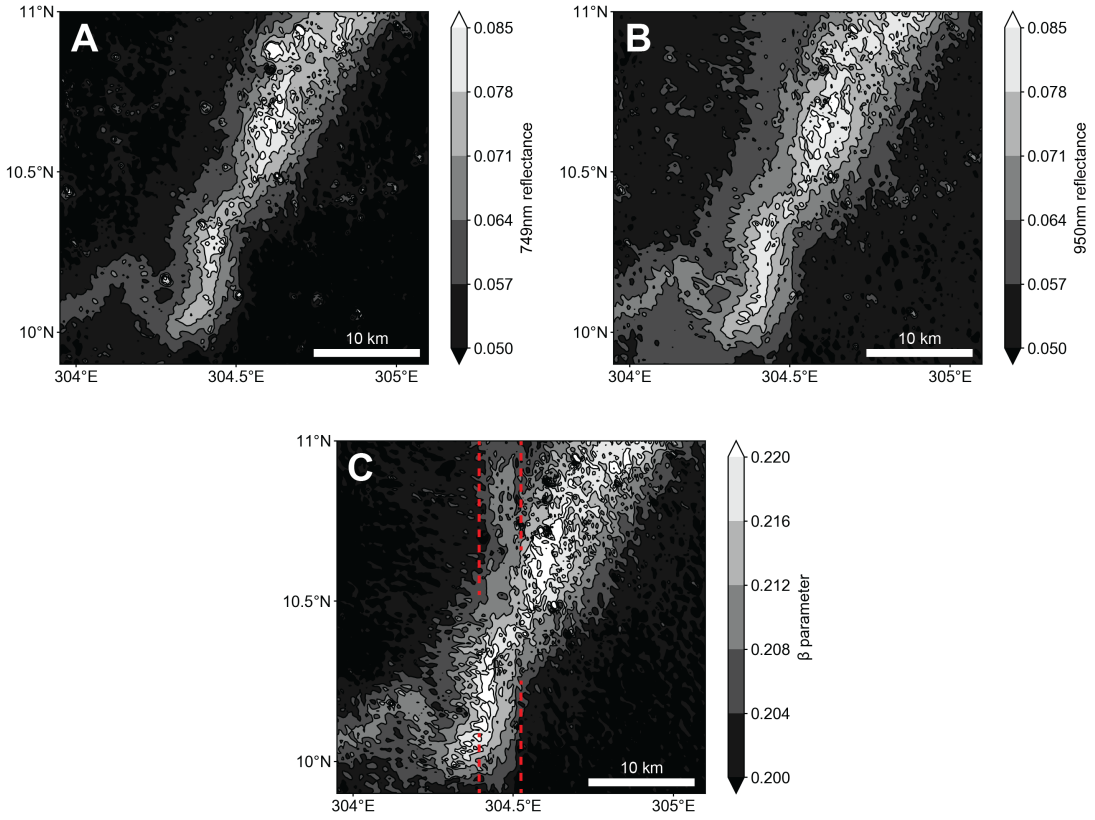

Figure A.3: Contour plot view of the reflectance and β parameter from the MI instrument on Kaguya. The panels in this figure contain the same data as in Figures A.2A, A.2B, and A.2C. (A) A contour plot of the 749 nm reflectance taken by the Multiband Imager (MI) instrument on Kaguya. (B) A contour plot of the 950 nm reflectance taken by the Multiband Imager (MI) instrument on Kaguya. (C) Kaguya β parameter combining the information in (A) and (B) following the method in McFadden et al. (2019). The dashed red lines indicate the extent of the north-south feature.

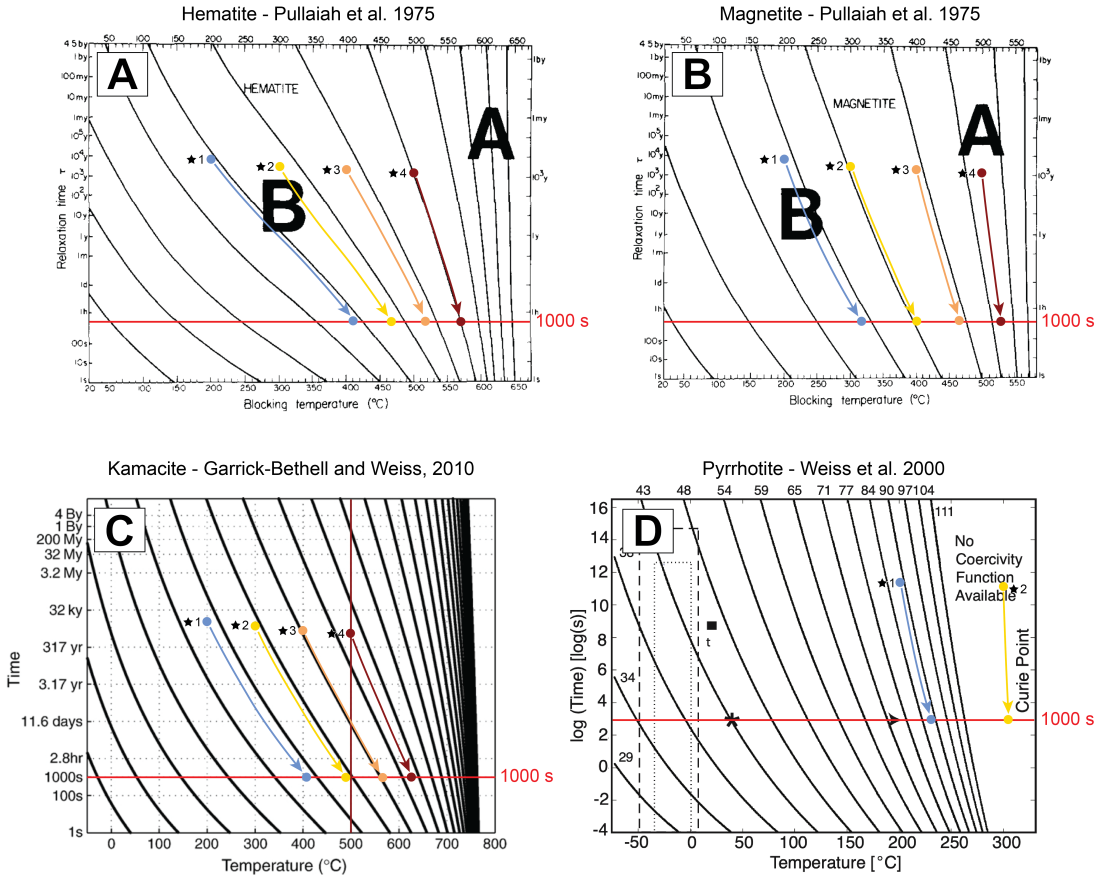

Figure A.4: Pullaiah diagrams for each of the four magnetic carriers that we consider. The laboratory timescale of 1000 seconds is indicated with a red line in each panel. The time/temperature conversions for each of the locations marked with a black star in Figure 3.11 are shown with traces in the color of their corresponding temperature value from Table 3.1. The other black points in Figure 3.11 are calculated in a similar way—the star points are simply used to illustrate the method. (A) The Pullaiah diagram for hematite (Pullaiah et al., 1975). (B) The Pullaiah diagram for magnetite (Pullaiah et al., 1975). (C) The Pullaiah diagram for kamacite (Garrick-Bethell and Weiss, 2010). (D) The Pullaiah diagram for pyrrhotite (Weiss et al., 2000). Note that only two traces are shown for pyrrhotite, because its Curie temperature, 325°C, is lower than the last two temperature values from Table 3.1.

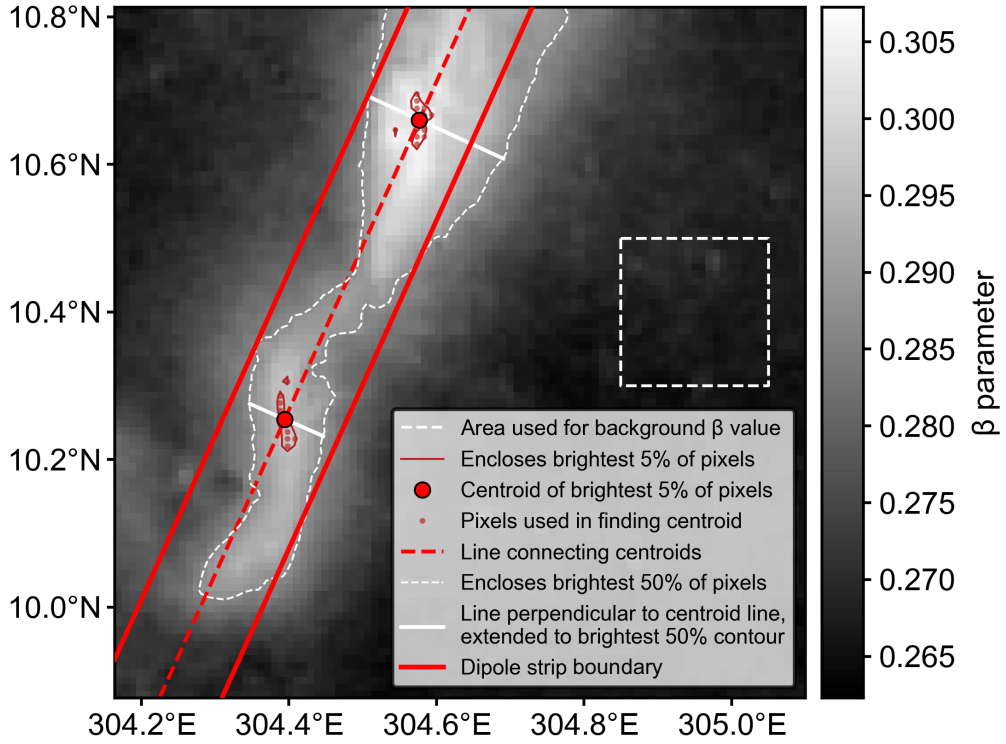

Figure A.5: The process used to find the strike and width of a strip of dipoles that represents the swirl magnetic source bodies prior to thermal demagnetization. The strike was found via the line connecting the centroids of the two areas containing the brightest 5% of pixels, and the width of the strip was taken to be the mean width at which the β parameter is halfway between its maximum and background values.

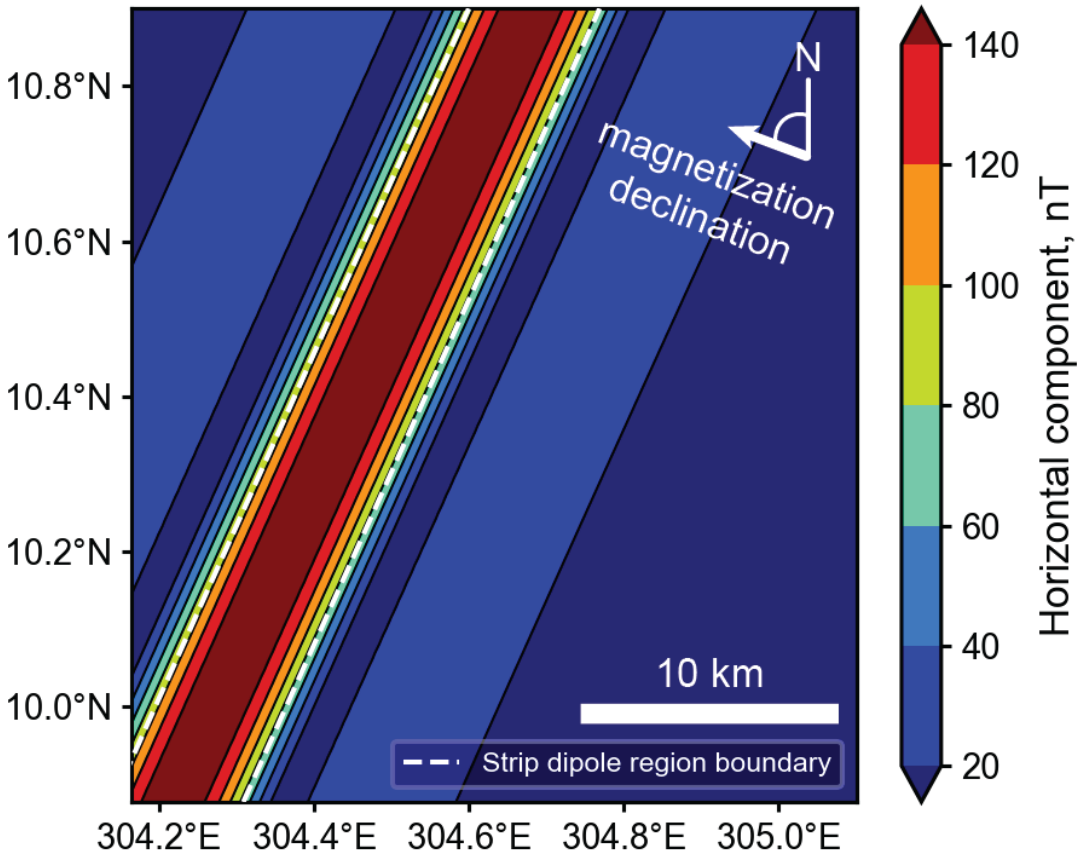

Figure A.6: The horizontal component of the magnetic field produced by the dipoles that compose the 2D strip prior to any dipole moment reductions.

Appendix B

Chapter 4 Supplementary Information

B.1 Magnetic field forward modeling without a linear decrease in dipole moments

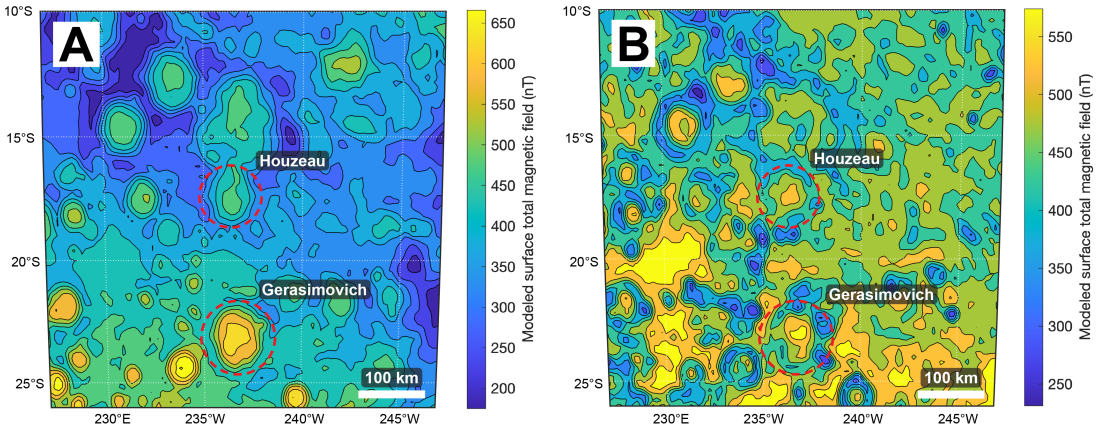

Figure B.1: The forward modeled magnetic field from dipoles with moments set inversely proportional to topography (panel A) and inversely proportional to surface slope (panel B). The peak dipole moment in each map is 10^{11} A·m^2, and the moments vary linearly between this peak and 0 A·m^2. Craters Gerasimovich and Houzeau are indicated with red dashed circles.

We compare the resulting magnetic field from dipoles with moments set by topography (Figure B.1A) and dipoles with moments set by surface slope (Figure B.1B). In the field set by topography (Figure B.1A), a peak is clearly visible at the crater Gerasimovich at approximately 237°E, 23°S, which coincides with the peak at Gerasimovich seen in the observations (Figures 4.2 and 4.3). To a lesser extent, there is a peak visible at Houzeau as well, which is also in the observations. In the field set by surface slope (Figure B.1B), the relationship between the modeled magnetic field and the observations is less clear. There is a small peak in magnetic field located in Gerasimovich (and an even smaller peak located in Houzeau), but it does not stand out from the background field as much as it does in the field set by topography (Figure B.1A). The highest peak in the field set by surface slope is located at approximately 230°E, 20°S, which is not collocated with the area of peak field in the observations.

B.2 Comparison craters for the four Gerasimovich-area craters that are older than Crisium

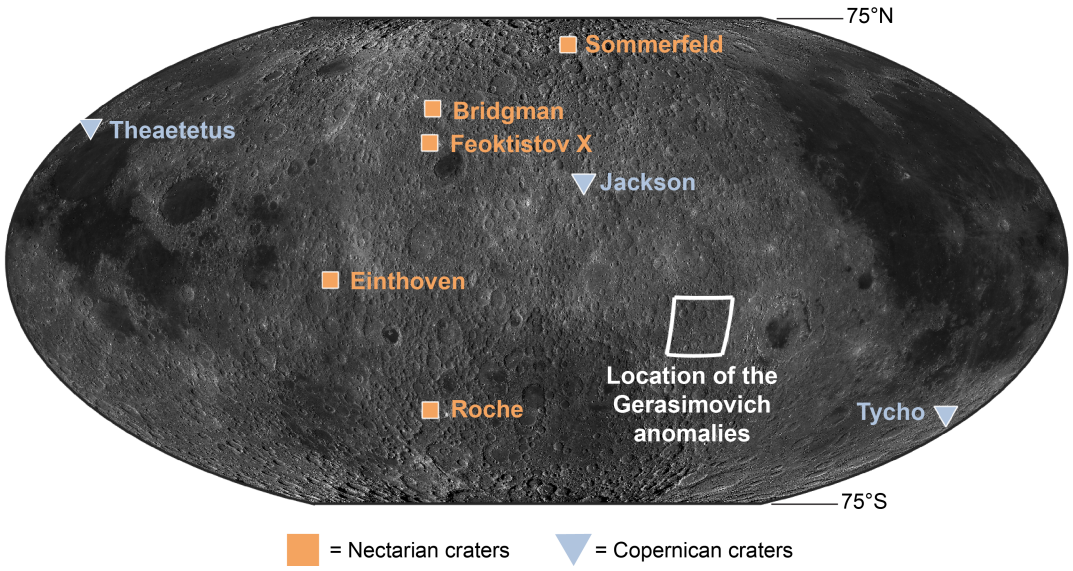

Figure B.2: Global map showing the locations of the eight craters compared to the Gerasimovich-area craters that are older than Crisium, color-coded by their age range. Each crater is listed in Figure 4.5, and the area shown in Figure 4.6 is marked with a white box.

B.3 Method to determine the average elevation of the profiles inside and outside the crater rim

To quantitatively compare each of the azimuthally averaged profiles, we developed a method to find the average elevation over the floor of each crater, and the average elevation of the area outside the rim of each crater. To find the average crater floor elevation, we first averaged the diameters of the three craters in a given comparison

group and divided it in half to obtain radius. Next, we converted this radius value into a floor radius value using a scaling relationship from Krüger et al. (2018), the parameters of which vary based on the size range of the crater being analyzed. Finally, we averaged the elevation of all points on the profile between the center of the crater and this floor radius, weighted by their distance from the center of the crater. To find the average elevation of the area outside the rim, we first recorded the average distance from the crater center to the outer base of the rim, chosen by eye, on the azimuthally averaged profile for each of the sets of craters. This averaged value was 1.73 crater radii for the groups of craters including Houzeau, Gerasimovich, and Crater Y, and 1.64 crater radii for the group of craters including Crater X. We then found the average elevation, again weighted by distance along the profile, of each point between the average base-of-rim distance for each group and 2.5 crater radii. In Figure 4.7, each of the averaged crater floor elevations and averaged outside-the-rim elevations are indicated with dotted and dashed lines, respectively.

B.4 Comparison craters for the four Gerasimovich-area craters that are younger than Crisium

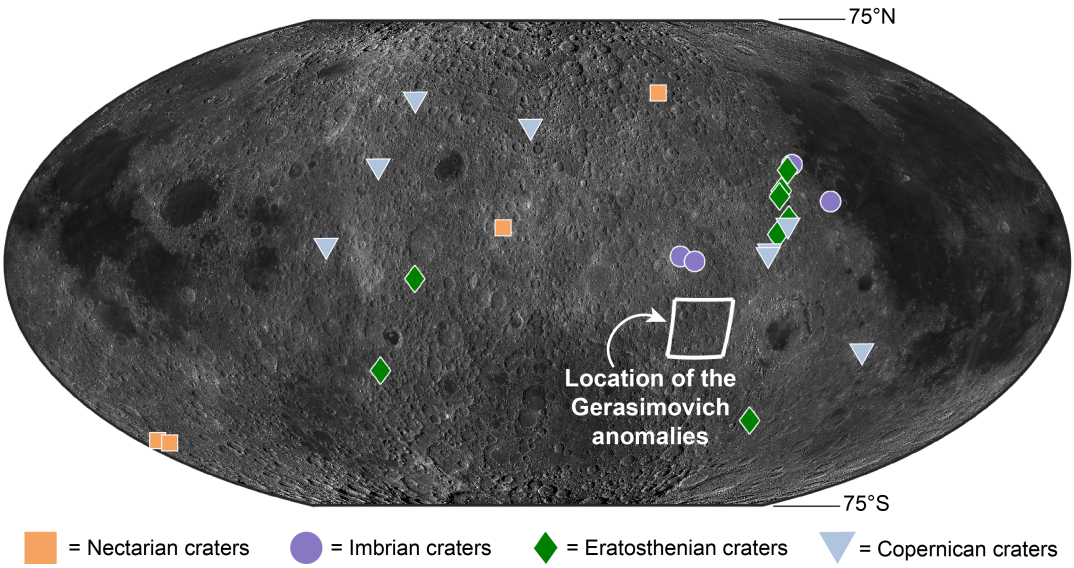

Figure B.3: Global map showing the locations of the four groups craters compared to the Gerasimovich-area craters that are younger than Crisium, color-coded by their age range. The area shown in Figure 4.11 is marked with a white box, and the details of each marked crater can be found in Figure B.4.

Crater	Longitude (°E)	Latitude (°N)	Period (Ji et al., 2022)	Diameter (km)	Depth (m)	Rim height (m)
Spencer Jones J	168.26531	9.63503	Ncf/Ncw; Nectarian	13.2	2621	342
Cuvier D	7.75306	-51.41231	Ncf/Ncw; Nectarian	16.8	1766	220
Cuvier F	11.20000	-52.32000	Ncf/Ncw; Nectarian	17.2	901	76
Kramers "X"	232.96829	48.94770	Ncf/Ncw; Nectarian	14.0	682	193
Nectarian crater averages				**15.3**	**1493**	**208**
Hertzsprung "Z"	228.56922	1.85157	I2c; Late Imbrian	14.4	2093	259
Hertzsprung "Y"	233.22903	0.45895	I1c; Early Imbrian	18.8	833	43
Voskresenskiy "X"	272.86116	27.34265	I2c; Late Imbrian	14.4	1637	273
Krafft H	282.09022	16.91006	I1c; Early Imbrian	14.8	976	432
Imbrian crater averages				**15.6**	**1385**	**252**
Bartels A	270.40962	25.68897	Ec; Eratosthenian	17.6	2701	585
Bell J	265.88956	19.88937	Ec; Eratosthenian	20.4	2944	382
Bell K	264.83193	18.33602	Ec; Eratosthenian	19.2	2885	649
Pannekoek T	138.45778	-4.28309	Ec; Eratosthenian	24.0	2993	206
Neujmin Q	121.8435	-30.03313	Ec; Eratosthenian	18.4	2689	113
Catalán U	269.32513	-45.05094	Ec; Eratosthenian	20.0	3548	662
Elvey G	261.97089	7.74465	Ec; Eratosthenian	14.0	2798	442
Sundman V	266.43806	11.96021	Ec; Eratosthenian	18.4	3486	854
Eratosthenian crater averages				**19.0**	**3006**	**487**
Lents C	258.24583	3.26931	Cc; Copernican	23.2	2869	849
Lents	257.70881	2.72898	Cc; Copernican	23.2	3024	459
Champollion "X"	177.05733	38.56138	Cc; Copernican	20.4	3752	613
Innes G	122.42648	26.85064	Cc; Copernican	21.2	2718	443
Segers	127.48106	46.96968	Cc; Copernican	16.0	2636	462
Al-Khwarizmi K	108.13133	4.50000	Cc; Copernican	23.2	3907	656
Byrgius A	296.19268	-24.57039	Cc; Copernican	18.8	4365	928
Sundman "X"	265.54127	10.37363	Cc; Copernican	10.4	2254	535
Copernican crater averages				**19.5**	**3191**	**618**

Figure B.4: The coordinates, ages, measured diameters, measured depths, and measured rim heights for the aggregated craters in Section 4.5.

Bibliography

J. Arkani-Hamed and D. Boutin. Analysis of isolated magnetic anomalies and magnetic signatures of impact craters: Evidence for a core dynamo in the early history of the Moon. *Icarus*, 237:262–277, 2014. doi: 10.1016/j.icarus.2014.04.046.

J. Arkani-Hamed and D. Boutin. South Pole Aitken Basin magnetic anomalies: Evidence for the true polar wander of Moon and a lunar dynamo reversal. *Journal of Geophysical Research: Planets*, 122(6):1195–1216, 2017. doi: 10.1002/2016JE005234.

S.-M. Baek, K.-H. Kim, I. Garrick-Bethell, H. Jin, H.-J. Lee, and J.-K. Lee. Detailed study of the Mare Crisium northern magnetic anomaly. *Journal of Geophysical Research: Planets*, 122(2):411–430, 2017. doi: 10.1002/2016JE005138. _eprint: https://agupubs.onlinelibrary.wiley.com/doi/pdf/10.1002/2016JE005138.

S.-M. Baek, K.-H. Kim, I. Garrick-Bethell, and H. Jin. Magnetic Anomalies Within the Crisium Basin: Magnetization Directions, Source Depths, and Ages. *Journal of Geophysical Research: Planets*, 124(2):223–242, 2019. doi: 10.1029/2018JE005678.

D. M. H. Baker, J. W. Head, C. I. Fassett, S. J. Kadish, D. E. Smith, M. T. Zuber, and G. A. Neumann. The transition from complex crater to peak-ring basin on the Moon: New observations from the Lunar Orbiter Laser Altimeter (LOLA) instrument. *Icarus*, 214(2):377–393, 2011. doi: 10.1016/j.icarus.2011.05.030.

R. A. Bamford, B. Kellett, W. J. Bradford, C. Norberg, A. Thornton, K. J. Gibson, I. A. Crawford, L. Silva, L. Gargaté, and R. Bingham. Minimagnetospheres above the Lunar Surface and the Formation of Lunar Swirls. *Phys. Rev. Lett.*, 109(8):081101, 2012. doi: 10.1103/PhysRevLett.109.081101.

S. A. Barboza and G. W. Bergantz. Dynamic model of dehydration melting motivated by a natural analogue: applications to the Ivrea-Verbano zone. *Ro. Sci. Edin.*, 87 (23), 1996.

J. Besserer, F. Nimmo, M. A. Wieczorek, R. C. Weber, W. S. Kiefer, P. J. McGovern, J. C. Andrews-Hanna, D. E. Smith, and M. T. Zuber. GRAIL gravity constraints on the vertical and lateral density structure of the lunar crust. *Geophysical Research Letters*, 41(16):5771–5777, 2014. doi: 10.1002/2014GL060240.

R. J. Blakely. *Potential Theory in Gravity and Magnetic Applications*. Cambridge University Press, 1996. ISBN 978-0-521-57547-8.

D. T. Blewett, E. I. Coman, B. R. Hawke, J. J. Gillis-Davis, M. E. Purucker, and C. G. Hughes. Lunar swirls: Examining crustal magnetic anomalies and space weathering trends. *Journal of Geophysical Research: Planets*, 116(E2), 2011. doi: 10.1029/2010JE003656.

K. L. Buchan. Baked Contact Test. In D. Gubbins and E. Herrero-Bervera, editors, *Encyclopedia of Geomagnetism and Paleomagnetism*, pages 35–39. Springer Netherlands, Dordrecht, 2007. ISBN 978-1-4020-4423-6. doi: 10.1007/978-1-4020-4423-6_12.

L. Carporzen, B. P. Weiss, L. T. Elkins-Tanton, D. L. Shuster, D. Ebel, and J. Gattacceca. Magnetic evidence for a partially differentiated carbonaceous chondrite parent body. *PNAS*, 108(16):6386–6389, 2011. doi: 10.1073/pnas.1017165108. Publisher: National Academy of Sciences Section: Physical Sciences.

C. Cournede, J. Gattacceca, M. Gounelle, P. Rochette, B. P. Weiss, and B. Zanda. An early solar system magnetic field recorded in CM chondrites. *Earth and Planetary Science Letters*, 410:62–74, 2015. doi: 10.1016/j.epsl.2014.11.019.

E. J. Dasch, C.-Y. Shih, B. M. Bansal, H. Wiesmann, and L. E. Nyquist. Isotopic analysis of basaltic fragments from lunar breccia 14321: Chronology and petrogenesis of pre-Imbrium mare volcanism. *Geochimica et Cosmochimica Acta*, 51(12):3241–3254, 1987. doi: 10.1016/0016-7037(87)90132-3.

J. Deca, A. Divin, C. Lue, T. Ahmadi, and M. Horányi. Reiner Gamma albedo features reproduced by modeling solar wind standoff. *Communications Physics*, 1(1):12, 2018. doi: 10.1038/s42005-018-0012-9.

J. Deca, D. J. Hemingway, A. Divin, C. Lue, A. R. Poppe, I. Garrick-Bethell, B. Lembège, and M. Horányi. Simulating the Reiner Gamma Swirl: The Long-Term Effect of Solar Wind Standoff. *Journal of Geophysical Research: Planets*, 125(5):e2019JE006219, 2020. doi: 10.1029/2019JE006219. _eprint: https://onlinelibrary.wiley.com/doi/pdf/10.1029/2019JE006219.

M. J. Dekkers. Magnetic properties of natural pyrrhotite. II. High- and low-temperature behaviour of Jrs and TRM as function of grain size. *Physics of the Earth and Planetary Interiors*, 57(3):266–283, 1989. doi: 10.1016/0031-9201(89)90116-7.

A. N. Deutsch, G. A. Neumann, J. W. Head, and L. Wilson. GRAIL-identified gravity anomalies in Oceanus Procellarum: Insight into subsurface impact and magmatic structures on the Moon. *Icarus*, 331:192–208, 2019. doi: 10.1016/j.icarus.2019.05.027.

I. Dinçer, A. Acar, I. Çobanoğlu, and Y. Uras. Correlation between Schmidt hardness, uniaxial compressive strength and Young's modulus for andesites, basalts and tuffs.

Bull Eng Geol Environ, 63(2):141–148, 2004. doi: 10.1007/s10064-004-0230-0.

D. J. Dunlop. Continuous and stepwise thermal demagnetization: are they equivalent? *Geophysical Journal International*, 177(3):949–957, 2009. doi: 10.1111/j.1365-246X.2009.04152.x.

C. A. Dwyer, D. J. Stevenson, and F. Nimmo. A long-lived lunar dynamo driven by continuous mechanical stirring. *Nature*, 479(7372):212–214, 2011. doi: 10.1038/nature10564.

P. Dyal, C. W. Parkin, and C. P. Sonett. Lunar-Surface Magnetometer Experiment. In *Apollo 15: Preliminary Science Report*, volume 1. Scientific and Technical Information Office, National Aeronautics and Space Administration, 1972. Google-Books-ID: SAQgAAAAIAAJ.

A. J. Evans and S. M. Tikoo. An episodic high-intensity lunar core dynamo. *Nat Astron*, pages 1–6, 2022. doi: 10.1038/s41550-021-01574-y.

A. J. Evans, J. M. Soderblom, J. C. Andrews-Hanna, S. C. Solomon, and M. T. Zuber. Identification of buried lunar impact craters from GRAIL data and implications for the nearside maria. *Geophysical Research Letters*, 43(6):2445–2455, 2016. doi: 10.1002/2015GL067394.

A. J. Evans, S. M. Tikoo, and J. C. Andrews-Hanna. The Case Against an Early Lunar Dynamo Powered by Core Convection. *Geophysical Research Letters*, 45(1):98–107, 2018. doi: 10.1002/2017GL075441. _eprint: https://agupubs.onlinelibrary.wiley.com/doi/pdf/10.1002/2017GL075441.

R. R. Fu, E. A. Lima, and B. P. Weiss. No nebular magnetization in the Allende CV carbonaceous chondrite. *Earth and Planetary Science Letters*, 404:54–66, 2014. doi: 10.1016/j.epsl.2014.07.014.

I. Garrick-Bethell and M. R. Kelley. Reiner Gamma: A Magnetized Elliptical Disk on the Moon. *Geophysical Research Letters*, 46(10):5065–5074, 2019. doi: 10.1029/2019GL082427.

I. Garrick-Bethell and B. P. Weiss. Kamacite blocking temperatures and applications to lunar magnetism. *Earth and Planetary Science Letters*, 294(1):1–7, 2010. doi: 10.1016/j.epsl.2010.02.013.

I. Garrick-Bethell, J. W. Head, and C. M. Pieters. Spectral properties, magnetic fields, and dust transport at lunar swirls. *Icarus*, 212(2):480–492, 2011. doi: 10.1016/j.icarus.2010.11.036.

I. Garrick-Bethell, A. R. Poppe, and S. Fatemi. The Lunar Paleo-Magnetosphere: Implications for the Accumulation of Polar Volatile Deposits. *Geophysical Research*

Letters, 46(11):5778–5787, 2019. doi: 10.1029/2019GL082548.

I. Garrick-Bethell, K. Miljković, H. Hiesinger, C. H. van der Bogert, M. Laneuville, D. L. Shuster, and D. G. Korycansky. Troctolite 76535: A sample of the Moon's South Pole-Aitken basin? *Icarus*, 338:113430, Mar. 2020. doi: 10.1016/j.icarus.2019.113430.

S. Gong, M. A. Wieczorek, F. Nimmo, W. S. Kiefer, J. W. Head, C. Huang, D. E. Smith, and M. T. Zuber. Thicknesses of mare basalts on the Moon from gravity and topography. *Journal of Geophysical Research: Planets*, 121(5):854–870, 2016. doi: 10.1002/2016JE005008.

J. Green, D. Draper, S. Boardsen, and C. Dong. When the Moon had a magnetosphere. *Science Advances*, 6(42):eabc0865, 2020. doi: 10.1126/sciadv.abc0865. Publisher: American Association for the Advancement of Science.

J. S. Halekas, D. L. Mitchell, R. P. Lin, S. Frey, L. L. Hood, M. H. Acuña, and A. B. Binder. Mapping of crustal magnetic anomalies on the lunar near side by the Lunar Prospector electron reflectometer. *Journal of Geophysical Research: Planets*, 106 (E11):27841–27852, 2001. doi: 10.1029/2000JE001380.

J. W. Head and A. Gifford. Lunar mare domes: Classification and modes of origin. *The Moon and the Planets*, 22(2):235–258, 1980. doi: 10.1007/BF00898434.

D. J. Heather and S. K. Dunkin. A stratigraphic study of southern Oceanus Procellarum using Clementine multispectral data. *Planetary and Space Science*, 50(14):1299–1309, 2002. doi: 10.1016/S0032-0633(02)00124-1.

D. J. Heather, S. K. Dunkin, and L. Wilson. Volcanism on the Marius Hills plateau: Observational analyses using Clementine multispectral data. *Journal of Geophysical Research: Planets*, 108(E3), 2003. doi: 10.1029/2002JE001938. _eprint: https://onlinelibrary.wiley.com/doi/pdf/10.1029/2002JE001938.

D. Hemingway and I. Garrick-Bethell. Magnetic field direction and lunar swirl morphology: Insights from Airy and Reiner Gamma. *Journal of Geophysical Research: Planets*, 117(E10), 2012. doi: 10.1029/2012JE004165.

D. J. Hemingway and S. M. Tikoo. Lunar Swirl Morphology Constrains the Geometry, Magnetization, and Origins of Lunar Magnetic Anomalies. *Journal of Geophysical Research: Planets*, 123(8):2223–2241, 2018. doi: 10.1029/2018JE005604.

D. J. Hemingway, I. Garrick-Bethell, and M. A. Kreslavsky. Latitudinal variation in spectral properties of the lunar maria and implications for space weathering. *Icarus*, 261:66–79, 2015. doi: 10.1016/j.icarus.2015.08.004.

M. Hess, C. Wöhler, M. Bhatt, A. A. Berezhnoy, A. Grumpe, K. Wohlfarth, A. Bhardwaj, and V. V. Shevchenko. Processes governing the VIS/NIR spectral reflectance

behavior of lunar swirls. *A&A*, 639:A12, 2020. doi: 10.1051/0004-6361/201937299. Publisher: EDP Sciences.

H. Hiesinger, J. W. Head, U. Wolf, R. Jaumann, and G. Neukum. Lunar mare basalt flow units: Thicknesses determined from crater size-frequency distributions. *Geophysical Research Letters*, 29(8):89–1–89–4, 2002. doi: 10.1029/2002GL014847. _eprint: https://agupubs.onlinelibrary.wiley.com/doi/pdf/10.1029/2002GL014847.

H. Hiesinger, J. W. Head, U. Wolf, R. Jaumann, and G. Neukum. Ages and stratigraphy of mare basalts in Oceanus Procellarum, Mare Nubium, Mare Cognitum, and Mare Insularum. *Journal of Geophysical Research: Planets*, 108(E7), 2003. doi: 10.1029/2002JE001985.

H. Hiesinger, J. W. Head, U. Wolf, R. Jaumann, and G. Neukum. Ages and stratigraphy of lunar mare basalts: A synthesis. In *Recent Advances and Current Research Issues in Lunar Stratigraphy*, pages 1–52. Geological Society of America, 2011.

H. Hiesinger, J. Gebhart, C. H. van der Bogert, J. H. Pasckert, J. Weinauer, S. J. Lawrence, J. D. Stopar, and M. S. Robinson. Stratigraphy of Low Shields and Mare Basalts of the Marius Hills Region, Moon. Abstract #1877, Lunar and Planetary Science Conference, The Woodlands, TX, 2016.

L. L. Hood. Central magnetic anomalies of Nectarian-aged lunar impact basins: Probable evidence for an early core dynamo. *Icarus*, 211(2):1109–1128, 2011. doi: 10.1016/j.icarus.2010.08.012.

L. L. Hood and N. A. Artemieva. Antipodal effects of lunar basin-forming impacts: Initial 3D simulations and comparisons with observations. *Icarus*, 193(2):485–502, 2008. doi: 10.1016/j.icarus.2007.08.023.

L. L. Hood and G. Schubert. Lunar Magnetic Anomalies and Surface Optical Properties. *Science*, 208(4439):49–51, 1980. doi: 10.1126/science.208.4439.49.

L. L. Hood, P. J. Coleman, C. T. Russell, and D. E. Wilhelms. Lunar magnetic anomalies detected by the Apollo substatellite magnetometers. *Physics of the Earth and Planetary Interiors*, 20(2):291–311, 1979. doi: 10.1016/0031-9201(79)90052-9.

L. L. Hood, A. Zakharian, J. Halekas, D. L. Mitchell, R. P. Lin, M. H. AcuÃ±a, and A. B. Binder. Initial mapping and interpretation of lunar crustal magnetic anomalies using Lunar Prospector magnetometer data. *Journal of Geophysical Research: Planets*, 106(E11):27825–27839, 2001. doi: 10.1029/2000JE001366.

L. L. Hood, N. C. Richmond, and P. D. Spudis. Origin of strong lunar magnetic anomalies: Further mapping and examinations of LROC imagery in regions antipodal to young large impact basins. *Journal of Geophysical Research: Planets*, 118(6):1265–1284, 2013. doi: 10.1002/jgre.20078.

L. L. Hood, J. S. Oliveira, J. Andrews-Hanna, M. A. Wieczorek, and S. T. Stewart. Magnetic Anomalies in Five Lunar Impact Basins: Implications for Impactor Trajectories and Inverse Modeling. *Journal of Geophysical Research: Planets*, 126(2):e2020JE006668, 2021a. doi: 10.1029/2020JE006668. _eprint: https://onlinelibrary.wiley.com/doi/pdf/10.1029/2020JE006668.

L. L. Hood, C. B. Torres, J. S. Oliveira, M. A. Wieczorek, and S. T. Stewart. A New Large-Scale Map of the Lunar Crustal Magnetic Field and Its Interpretation. *Journal of Geophysical Research: Planets*, 126(2):e2020JE006667, 2021b. doi: 10.1029/2020JE006667. _eprint: https://onlinelibrary.wiley.com/doi/pdf/10.1029/2020JE006667.

J. Huang, L. Xiao, X. He, L. Qiao, J. Zhao, and H. Li. Geological characteristics and model ages of Marius Hills on the Moon. *J. Earth Sci.*, 22(5):601, 2011. doi: 10.1007/s12583-011-0211-8.

Q. Huang, Z. Xiao, and L. Xiao. Subsurface structures of large volcanic complexes on the nearside of the Moon: A view from GRAIL gravity. *Icarus*, 243:48–57, 2014. doi: 10.1016/j.icarus.2014.09.009.

A. Ikeda, H. Kumagai, and T. Morota. Topographic Degradation Processes of Lunar Crater Walls Inferred From Boulder Falls. *Journal of Geophysical Research: Planets*, 127(10):e2021JE007176, 2022. doi: 10.1029/2021JE007176. _eprint: https://onlinelibrary.wiley.com/doi/pdf/10.1029/2021JE007176.

J. Ji, D. Guo, J. Liu, S. Chen, Z. Ling, X. Ding, K. Han, J. Chen, W. Cheng, K. Zhu, J. Liu, J. Wang, J. Chen, and Z. Ouyang. The 1:2,500,000-scale geologic map of the global moon. *Science Bulletin*, 2022. doi: 10.1016/j.scib.2022.05.021.

M. R. Kelley and I. Garrick-Bethell. Gravity constraints on the age and formation of the Moon's Reiner Gamma magnetic anomaly. *Icarus*, 338:113465, 2020. doi: 10.1016/j.icarus.2019.113465.

M. R. Kelley, I. Garrick-Bethell, and S. J. Goossens. Evidence for thermal demagnetization of the Moon's Reiner Gamma Magnetic Anomaly. Abstract #2415, Lunar and Planetary Science Conference, The Woodlands, TX, 2018. https://www.hou.usra.edu/meetings/lpsc2018/pdf/2415.pdf.

W. S. Kiefer. Gravity constraints on the subsurface structure of the Marius Hills: The magmatic plumbing of the largest lunar volcanic dome complex. *Journal of Geophysical Research: Planets*, 118(4):733–745, 2013. doi: 10.1029/2012JE004111.

B. P. Kokelaar, R. S. Bahia, K. H. Joy, S. Viroulet, and J. M. N. T. Gray. Granular avalanches on the Moon: Mass-wasting conditions, processes, and features. *Journal of Geophysical Research: Planets*, 122(9):1893–1925, 2017. doi: 10.1002/2017JE005320.

_eprint: https://onlinelibrary.wiley.com/doi/pdf/10.1002/2017JE005320.

M. A. Kreslavsky and J. W. Head. New observational evidence of global seismic effects of basin-forming impacts on the Moon from Lunar Reconnaissance Orbiter Lunar Orbiter Laser Altimeter data. *Journal of Geophysical Research: Planets*, 117(E12), 2012. doi: 10.1029/2011JE003975. _eprint: https://onlinelibrary.wiley.com/doi/pdf/10.1029/2011JE003975.

T. Krüger, S. Hergarten, and T. Kenkmann. Deriving Morphometric Parameters and the Simple-to-Complex Transition Diameter From a High-Resolution, Global Database of Fresh Lunar Impact Craters (D 3 km). *Journal of Geophysical Research: Planets*, 123(10):2667–2690, 2018. doi: 10.1029/2018JE005545. _eprint: https://onlinelibrary.wiley.com/doi/pdf/10.1029/2018JE005545.

M. Kurata, H. Tsunakawa, Y. Saito, H. Shibuya, M. Matsushima, and H. Shimizu. Mini-magnetosphere over the Reiner Gamma magnetic anomaly region on the Moon. *Geophysical Research Letters*, 32(24), 2005. doi: https://doi.org/10.1029/2005GL024097. _eprint: https://agupubs.onlinelibrary.wiley.com/doi/pdf/10.1029/2005GL024097.

M. Laneuville, M. A. Wieczorek, D. Breuer, and N. Tosi. Asymmetric thermal evolution of the Moon. *Journal of Geophysical Research: Planets*, 118(7):1435–1452, 2013. doi: 10.1002/jgre.20103. _eprint: https://onlinelibrary.wiley.com/doi/pdf/10.1002/jgre.20103.

S. J. Lawrence, J. D. Stopar, B. R. Hawke, B. T. Greenhagen, J. T. S. Cahill, J. L. Bandfield, B. L. Jolliff, B. W. Denevi, M. S. Robinson, T. D. Glotch, D. B. J. Bussey, P. D. Spudis, T. A. Giguere, and W. B. Garry. LRO observations of morphology and surface roughness of volcanic cones and lobate lava flows in the Marius Hills. *Journal of Geophysical Research: Planets*, 118(4):615–634, 2013. doi: 10.1002/jgre.20060. _eprint: https://onlinelibrary.wiley.com/doi/pdf/10.1002/jgre.20060.

J.-K. Lee, R. Maxwell, H. Jin, S.-M. Baek, O. Ghassemi, M. Kelley, H. Lee, K.-H. Kim, S. Lee, and I. Garrick-Bethell. A small lunar swirl and its implications for the formation of the Reiner Gamma magnetic anomaly. *Icarus*, 319:869–884, 2019. doi: 10.1016/j.icarus.2018.09.015.

R. Lena, C. Wöhler, J. Phillips, and M. T. Chiocchetta. *Lunar Domes: Properties and Formation Processes*. Springer Science & Business Media, 2013. ISBN 978-88-470-2637-7. Google-Books-ID: 6F5h39Azb1kC.

R. J. Lillis, J. Dufek, J. E. Bleacher, and M. Manga. Demagnetization of crust by magmatic intrusion near the Arsia Mons volcano: Magnetic and thermal implications for the development of the Tharsis province, Mars. *Journal of Volcanology and Geothermal Research*, 185(1):123–138, 2009. doi: 10.1016/j.jvolgeores.2008.12.007.

R. J. Lillis, J. Dufek, W. S. Kiefer, B. A. Black, M. Manga, J. A. Richardson, and J. E. Bleacher. The Syrtis Major volcano, Mars: A multidisciplinary approach to interpreting its magmatic evolution and structural development. *Journal of Geophysical Research: Planets*, 120(9):1476–1496, 2015. doi: 10.1002/2014JE004774.

R. P. Lin, K. A. Anderson, and L. L. Hood. Lunar surface magnetic field concentrations antipodal to young large impact basins. *Icarus*, 74(3):529–541, June 1988. doi: 10.1016/0019-1035(88)90119-4.

R. E. Maxwell and I. Garrick-Bethell. Evidence for an Ancient Near-Equatorial Lunar Dipole From Higher Precision Inversions of Crustal Magnetization. *Journal of Geophysical Research: Planets*, 125 (12):e2020JE006567, 2020. doi: 10.1029/2020JE006567. _eprint: https://agupubs.onlinelibrary.wiley.com/doi/pdf/10.1029/2020JE006567.

A. R. McBirney. *Igneous Petrology*. Jones & Bartlett Learning, 1993. ISBN 978-0-86720-175-8. Google-Books-ID: Nl73ymr7cgIC.

J. F. McCauley. Geologic map of the Hevelius region of the moon. *U.S. Geological Survey Report*, page 491, 1967. ADS Bibcode: 1967USGS...IM..491M.

J. McFadden, I. Garrick-Bethell, C. K. Sim, S. S. Kim, and D. Hemingway. Iron content determines how space weathering flux variations affect lunar soils. *Icarus*, 333:323–342, 2019. doi: 10.1016/j.icarus.2019.05.033.

H. J. Melosh. *Impact cratering: A geologic process*. New York: Oxford University Press, 1989.

H. J. Melosh. *Planetary Surface Processes*. Cambridge University Press, 2011. ISBN 978-1-139-49830-2. Google-Books-ID: 3bQD1DJgliIC.

D. L. Mitchell, J. S. Halekas, R. P. Lin, S. Frey, L. L. Hood, M. H. Acua, and A. Binder. Global mapping of lunar crustal magnetic fields by Lunar Prospector. *Icarus*, 194(2): 401–409, 2008. doi: 10.1016/j.icarus.2007.10.027.

M. Nayak, D. Hemingway, and I. Garrick-Bethell. Magnetization in the South Pole-Aitken basin: Implications for the lunar dynamo and true polar wander. *Icarus*, 286: 153–192, 2017. doi: 10.1016/j.icarus.2016.09.038.

J. S. Oliveira and M. A. Wieczorek. Testing the axial dipole hypothesis for the Moon by modeling the direction of crustal magnetization. *Journal of Geophysical Research: Planets*, 122(2):383–399, 2017. doi: 10.1002/2016JE005199. _eprint: https://agupubs.onlinelibrary.wiley.com/doi/pdf/10.1002/2016JE005199.

J. S. Oliveira, M. A. Wieczorek, and G. Kletetschka. Iron Abundances in Lunar Impact Basin Melt Sheets From Orbital Magnetic Field Data. *Journal of Geophysical*

Research: Planets, 122(12):2429–2444, 2017. doi: 10.1002/2017JE005397.

O. Özdemir and D. J. Dunlop. Thermoremanent magnetization of multidomain hematite. *Journal of Geophysical Research: Solid Earth*, 110(B9), 2005. doi: 10.1029/2005JB003820. _eprint: https://agupubs.onlinelibrary.wiley.com/doi/pdf/10.1029/2005JB003820.

R. J. Pike. Size-dependence in the shape of fresh impact craters on the moon. In *Impact and Explosion Cratering*, pages 489–509, 1977.

D. D. Pollard and A. M. Johnson. Mechanics of growth of some laccolithic intrusions in the Henry mountains, Utah, II: Bending and failure of overburden layers and sill formation. *Tectonophysics*, 18(3):311–354, 1973. doi: 10.1016/0040-1951(73)90051-6.

A. R. Poppe, S. Fatemi, I. Garrick-Bethell, D. Hemingway, and M. Holmström. Solar wind interaction with the Reiner Gamma crustal magnetic anomaly: Connecting source magnetization to surface weathering. *Icarus*, 266:261–266, 2016. doi: 10.1016/j.icarus.2015.11.005.

A. R. Poppe, I. Garrick-Bethell, and S. Fatemi. Fractionation of Solar Wind Minor Ion Precipitation by the Lunar Paleomagnetosphere. *The Planetary Science Journal*, 2: 60, 2021. doi: 10.3847/PSJ/abea7d.

V. Pratt. Direct Least-squares Fitting of Algebraic Surfaces. In *Proceedings of the 14th Annual Conference on Computer Graphics and Interactive Techniques*, SIGGRAPH '87, pages 145–152, New York, NY, USA, 1987. ACM. ISBN 978-0-89791-227-3. doi: 10.1145/37401.37420.

G. Pullaiah, E. Irving, K. L. Buchan, and D. J. Dunlop. Magnetization changes caused by burial and uplift. *Earth and Planetary Science Letters*, 28(2):133–143, 1975. doi: 10.1016/0012-821X(75)90221-6.

M. E. Purucker and J. B. Nicholas. Global spherical harmonic models of the internal magnetic field of the Moon based on sequential and coestimation approaches. *Journal of Geophysical Research: Planets*, 115(E12), 2010. doi: https://doi.org/10.1029/2010JE003650. _eprint: https://agupubs.onlinelibrary.wiley.com/doi/pdf/10.1029/2010JE003650.

M. E. Purucker, J. W. Head, and L. Wilson. Magnetic signature of the lunar South Pole-Aitken basin: Character, origin, and age. *Journal of Geophysical Research: Planets*, 117(E5), 2012. doi: 10.1029/2011JE003922.

D. Ravat, M. E. Purucker, and N. Olsen. Lunar Magnetic Field Models From Lunar Prospector and SELENE/Kaguya Along-Track Magnetic Field Gradients. *Journal of Geophysical Research: Planets*, 125(7): e2019JE006187, 2020. doi: https://doi.org/10.1029/2019JE006187. _eprint:

https://agupubs.onlinelibrary.wiley.com/doi/pdf/10.1029/2019JE006187.

M. S. Robinson, S. M. Brylow, M. Tschimmel, D. Humm, S. J. Lawrence, P. C. Thomas, B. W. Denevi, E. Bowman-Cisneros, J. Zerr, M. A. Ravine, M. A. Caplinger, F. T. Ghaemi, J. A. Schaffner, M. C. Malin, P. Mahanti, A. Bartels, J. Anderson, T. N. Tran, E. M. Eliason, A. S. McEwen, E. Turtle, B. L. Jolliff, and H. Hiesinger. Lunar Reconnaissance Orbiter Camera (LROC) Instrument Overview. *Space Sci Rev*, 150 (1):81–124, 2010. doi: 10.1007/s11214-010-9634-2.

A. M. Rubin and D. D. Pollard. Origins of blade-like dikes in volcanic rift zones. *U. S. Geological Survey Professional Paper*, 1350(2):1449–1470, 1987. Publisher: U.S. Geological Survey.

A. L. Scheinberg, K. M. Soderlund, and L. T. Elkins-Tanton. A basal magma ocean dynamo to explain the early lunar magnetic field. *Earth and Planetary Science Letters*, 492:144–151, 2018. doi: 10.1016/j.epsl.2018.04.015.

P. Senthil Kumar, U. Sruthi, N. Krishna, K. J. P. Lakshmi, R. Menon, Amitabh, B. Gopala Krishna, D. A. Kring, J. W. Head, J. N. Goswami, and A. S. Kiran Kumar. Recent shallow moonquake and impact-triggered boulder falls on the Moon: New insights from the Schrödinger basin. *Journal of Geophysical Research: Planets*, 121(2):147–179, 2016. doi: 10.1002/2015JE004850. _eprint: https://onlinelibrary.wiley.com/doi/pdf/10.1002/2015JE004850.

M. R. K. Seritan and I. Garrick-Bethell. Volcanic thermal demagnetization of the Reiner Gamma magnetic anomaly. *Icarus*, 2022, under review.

E. K. Shea, B. P. Weiss, W. S. Cassata, D. L. Shuster, S. M. Tikoo, J. Gattacceca, T. L. Grove, and M. D. Fuller. A Long-Lived Lunar Core Dynamo. *Science*, 335(6067): 453–456, 2012. doi: 10.1126/science.1215359.

D. E. Smith, M. T. Zuber, G. A. Neumann, F. G. Lemoine, E. Mazarico, M. H. Torrence, J. F. McGarry, D. D. Rowlands, J. W. Head, T. H. Duxbury, O. Aharonson, P. G. Lucey, M. S. Robinson, O. S. Barnouin, J. F. Cavanaugh, X. Sun, P. Liiva, D.-d. Mao, J. C. Smith, and A. E. Bartels. Initial observations from the Lunar Orbiter Laser Altimeter (LOLA). *Geophysical Research Letters*, 37(18), 2010. doi: 10.1029/2010GL043751.

D. Stöffler, G. Ryder, B. A. Ivanov, N. A. Artemieva, M. J. Cintala, and R. A. F. Grieve. Cratering History and Lunar Chronology. *Reviews in Mineralogy and Geochemistry*, 60(1):519–596, 2006. doi: 10.2138/rmg.2006.60.05.

C. Suavet, B. P. Weiss, W. S. Cassata, D. L. Shuster, J. Gattacceca, L. Chan, I. Garrick-Bethell, J. W. Head, T. L. Grove, and M. D. Fuller. Persistence and origin of the lunar core dynamo. *PNAS*, 110(21):8453–8458, 2013. doi: 10.1073/pnas.1300341110.

C. Suavet, B. P. Weiss, and T. L. Grove. Controlled-atmosphere thermal demagnetization and paleointensity analyses of extraterrestrial rocks. *Geochemistry, Geophysics, Geosystems*, 15(7):2733–2743, 2014. doi: 10.1002/2013GC005215.

F. Takahashi, H. Tsunakawa, H. Shimizu, H. Shibuya, and M. Matsushima. Reorientation of the early lunar pole. *Nature Geoscience*, 7(6):409–412, 2014. doi: 10.1038/ngeo2150. Number: 6 Publisher: Nature Publishing Group.

J. A. Tarduno, R. D. Cottrell, K. Lawrence, R. K. Bono, W. Huang, C. L. Johnson, E. G. Blackman, A. V. Smirnov, M. Nakajima, C. R. Neal, T. Zhou, M. Ibanez-Mejia, H. Oda, and B. Crummins. Absence of a long-lived lunar paleomagnetosphere. *Science Advances*, 7(32):eabi7647, 2021. doi: 10.1126/sciadv.abi7647. Publisher: American Association for the Advancement of Science Section: Research Article.

L. A. Taylor, J. W. Shervais, R. H. Hunter, C.-Y. Shih, B. M. Bansal, J. Wooden, L. E. Nyquist, and L. C. Laul. Pre-4.2 AE mare-basalt volcanism in the lunar highlands. *Earth and Planetary Science Letters*, 66:33–47, 1983. doi: 10.1016/0012-821X(83)90124-3.

K. Terada, M. Anand, A. K. Sokol, A. Bischoff, and Y. Sano. Cryptomare magmatism 4.35 Gyr ago recorded in lunar meteorite Kalahari 009. *Nature*, 450(7171):849–852, 2007. doi: 10.1038/nature06356.

S. M. Tikoo, B. P. Weiss, J. Buz, E. A. Lima, E. K. Shea, G. Melo, and T. L. Grove. Magnetic fidelity of lunar samples and implications for an ancient core dynamo. *Earth and Planetary Science Letters*, 337-338:93–103, 2012. doi: 10.1016/j.epsl.2012.05.024.

S. M. Tikoo, B. P. Weiss, W. S. Cassata, D. L. Shuster, J. Gattacceca, E. A. Lima, C. Suavet, F. Nimmo, and M. D. Fuller. Decline of the lunar core dynamo. *Earth and Planetary Science Letters*, 404:89–97, 2014. doi: 10.1016/j.epsl.2014.07.010.

S. M. Tikoo, J. Gattacceca, N. L. Swanson-Hysell, B. P. Weiss, C. Suavet, and C. Cournède. Preservation and detectability of shock-induced magnetization. *Journal of Geophysical Research: Planets*, 120(9):1461–1475, 2015a. doi: 10.1002/2015JE004840.

S. M. Tikoo, N. L. Swanson-Hysell, and N. S. Bezaeva. Rock magnetic effects induced in basalt and diabase by >20 GPa experimental shock waves. Abstract #5079, Annual Meeting of the Meteoritical Society, Berkeley, CA, 2015b. https://www.hou.usra.edu/meetings/metsoc2015/pdf/5079.pdf.

H. Tsunakawa, F. Takahashi, H. Shimizu, H. Shibuya, and M. Matsushima. Surface vector mapping of magnetic anomalies over the Moon using Kaguya and Lunar Prospector observations. *Journal of Geophysical Research: Planets*, 120(6):1160–1185, 2015. doi: 10.1002/2014JE004785.

D. Turcotte and G. Schubert. *Geodynamics*. Cambridge University Press, 2014. ISBN 978-1-107-00653-9. Google-Books-ID: qksHAwAAQBAJ.

S. Wakita, B. C. Johnson, I. Garrick-Bethell, M. R. Kelley, R. E. Maxwell, and T. M. Davison. Impactor material records the ancient lunar magnetic field in antipodal anomalies. *Nat Commun*, 12(1):6543, 2021. doi: 10.1038/s41467-021-26860-1. Number: 1 Publisher: Nature Publishing Group.

B. P. Weiss and S. M. Tikoo. The lunar dynamo. *Science*, 346(6214):1246753, 2014. doi: 10.1126/science.1246753.

B. P. Weiss, J. L. Kirschvink, F. J. Baudenbacher, H. Vali, N. T. Peters, F. A. Macdonald, and J. P. Wikswo. A Low Temperature Transfer of ALH84001 from Mars to Earth. *Science*, 290(5492):791–795, 2000. doi: 10.1126/science.290.5492.791. Publisher: American Association for the Advancement of Science Section: Report.

B. P. Weiss, J. S. Berdahl, L. Elkins-Tanton, S. Stanley, E. A. Lima, and L. Carporzen. Magnetism on the Angrite Parent Body and the Early Differentiation of Planetesimals. *Science*, 322(5902):713–716, 2008. doi: 10.1126/science.1162459. Publisher: American Association for the Advancement of Science Section: Report.

B. P. Weiss, H. Wang, T. G. Sharp, J. Gattacceca, D. L. Shuster, B. Downey, J. Hu, R. R. Fu, A. T. Kuan, C. Suavet, A. J. Irving, J. Wang, and J. Wang. A nonmagnetic differentiated early planetary body. *Earth and Planetary Science Letters*, 468:119–132, 2017. doi: 10.1016/j.epsl.2017.03.026.

C. M. Weitz and J. W. Head. Spectral properties of the Marius Hills volcanic complex and implications for the formation of lunar domes and cones. *Journal of Geophysical Research: Planets*, 104(E8):18933–18956, 1999. doi: 10.1029/1998JE000630.

J. L. Whitford-Stark and J. W. Head. The Procellarum volcanic complexes - Contrasting styles of volcanism. In *Lunar and Planetary Science Conference Proceedings*, volume 8, pages 2705–2724, 1977.

J. Whitten, J. W. Head, M. Staid, C. M. Pieters, J. Mustard, R. Clark, J. Nettles, R. L. Klima, and L. Taylor. Lunar mare deposits associated with the Orientale impact basin: New insights into mineralogy, history, mode of emplacement, and relation to Orientale Basin evolution from Moon Mineralogy Mapper (M3) data from Chandrayaan-1. *Journal of Geophysical Research: Planets*, 116(E6), 2011. doi: 10.1029/2010JE003736.

J. L. Whitten and J. W. Head. Lunar cryptomaria: Physical characteristics, distribution, and implications for ancient volcanism. *Icarus*, 247:150–171, 2015. doi: 10.1016/j.icarus.2014.09.031.

R. W. Wichman and P. H. Schultz. Crater-Centered Laccoliths on the Moon: Modeling

Intrusion Depth and Magmatic Pressure at the Crater Taruntius. *Icarus*, 122(1): 193–199, 1996. doi: 10.1006/icar.1996.0118.

M. A. Wieczorek, B. P. Weiss, and S. T. Stewart. An Impactor Origin for Lunar Magnetic Anomalies. *Science*, 335(6073):1212–1215, 2012. doi: 10.1126/science.1214773.

D. E. Wilhelms, J. F. with sections by McCauley, and N. J. Trask. The geologic history of the Moon. USGS Numbered Series 1348, U. S. Geological Survey, 1987.

C. Wöhler and R. Lena. Lunar intrusive domes: Morphometric analysis and laccolith modelling. *Icarus*, 204(2):381–398, 2009. doi: 10.1016/j.icarus.2009.07.031.

Y. Zhang, J. G. Stevens, Y. Li, and Z. Li. Mössbauer study of the Jilin and Xinyang meteorites. *Hyperfine Interact*, 91(1):547–550, 1994. doi: 10.1007/BF02064568.

M. T. Zuber, D. E. Smith, M. M. Watkins, S. W. Asmar, A. S. Konopliv, F. G. Lemoine, H. J. Melosh, G. A. Neumann, R. J. Phillips, S. C. Solomon, M. A. Wieczorek, J. G. Williams, S. J. Goossens, G. Kruizinga, E. Mazarico, R. S. Park, and D.-N. Yuan. Gravity Field of the Moon from the Gravity Recovery and Interior Laboratory (GRAIL) Mission. *Science*, 339(6120):668–671, 2013. doi: 10.1126/science.1231507.